

**Nanodiamonds for biological applications:
Synthesis by laser ablation and sensing of
local magnetic environment by optical
spectroscopy of NV centers**

Federico Gorrini

Committee members:

Dr. Claudia E. Avalos

École polytechnique fédérale de Lausanne (EPFL)

Prof. Paolo Ossi

Dipartimento di Energia - Politecnico di Milano, Italy

Prof. Giulio Monaco

Dipartimento di Fisica - Università di Trento, Italy

To my parents and my sister

*One does not discover new lands without
consenting to lose sight, for a very long time, of the
shore.*

- André Gide -

Curriculum Vitae

Name of author: Federico Gorrini

Date of birth: 12 September 1987

Place of birth: Rovereto, Italy

BPhys: University of Trento, Italy (2010)

MPhys: University of Trento, Italy (2013)

List of publications

- 1) Mazzi, A., F. Gorrini and A. Miotello (2015). "Liquid nanodroplet formation through phase explosion mechanism in laser-irradiated metal targets." Physical Review E **92**(3).
- 2) Mazzi, A., F. Gorrini and A. Miotello (2017). "Dynamics of liquid nanodroplet formation in nanosecond laser ablation of metals." Applied Surface Science **418**: 601-606.
- 3) Gorrini, F., M. Cazzanelli, N. Bazzanella, R. Edla, M. Gemmi, V. Cappello, J. David, C. Dorigoni, A. Bifone and A. Miotello (2016). "On the thermodynamic path enabling a room-temperature, laser-assisted graphite to nanodiamond transformation." Sci Rep **6**: 35244.
- 4) Basso, L., F. Gorrini, N. Bazzanella, M. Cazzanelli, C. Dorigoni, A. Bifone and A. Miotello (2017). "The modeling and synthesis of nanodiamonds by laser ablation of graphite and diamond-like carbon in liquid-confined ambient." Applied Physics A **124**(1).

Citations to Previously Published Works:

Large portions of Chapter 2 have appeared in the following papers:

- 1) Mazzi, A., F. Gorrini and A. Miotello (2015). "Liquid nanodroplet formation through phase explosion mechanism in laser-irradiated metal targets." Physical Review E **92**(3).
- 2) Mazzi, A., F. Gorrini and A. Miotello (2017). "Dynamics of liquid nanodroplet formation in nanosecond laser ablation of metals." Applied Surface Science **418**: 601-606.

Large portions of Chapter 4 have appeared in the following paper:

Gorrini, F., M. Cazzanelli, N. Bazzanella, R. Edla, M. Gemmi, V. Cappello, J. David, C. Dorigoni, A. Bifone and A. Miotello (2016). "On the thermodynamic path enabling a room-temperature, laser-assisted graphite to nanodiamond transformation." Sci Rep **6**: 35244.

Abstract

Nanodiamonds (NDs) are the subject of intense investigation for their unique physical and chemical properties. Due to high hardness, optical transparency and biocompatibility, NDs find applications in tribology, catalysis and drug delivery. When enriched with nitrogen-vacancy (NV) centers, NDs can be used in bioimaging and biosensing. While the field is progressing rapidly, a number of problems are still open. In this dissertation I have tackled two important aspects for the development of NDs as biosensors:

- 1) production of NDs with controlled size and properties;
- 2) characterization and optimization of commercial fluorescent NDs as probes of paramagnetic species.

In the first part of my thesis, I report a novel synthesis route for NDs by pulsed laser ablation (PLA) in water. PLA can directly produce diamonds on a nanoscopic scale, with potential advantages over alternative methods, like grinding of bulk crystals or detonation techniques. Specifically, I demonstrate synthesis of nanometric diamond crystals by PLA in aqueous environment, and investigate the thermodynamics of this process. Indeed, the synthesis of NDs by PLA is related to a drastic change in the thermodynamic state of the target upon laser irradiation. Fast laser-induced heating results in melting and superheating of the target, followed by a strong boiling, a process named "phase explosion", and then by a fast cooling of the molten material in water. I provide a theoretical description of both superheated and undercooled liquids and of the mechanism of phase explosion. The investigation of the link between the metastable liquids (superheated or undercooled) and the synthesis of nanoparticles is carried out by theoretical analyses, computer simulations and comparison of our experimental data with previous literature.

In the second part of the thesis I turn to commercial NDs enriched with (NV) centers. The purpose of the investigation is to explore the use of fluorescent NDs for sensing of paramagnetic species of biological interest. To this end, I explored

the effects of size and surface coating on the optical properties and sensing capabilities of fluorescent NDs.

Following a theoretical introduction to the basic properties of the NV centers and to the ground state spin dynamics of these color centers, I describe the set up used for the experimental characterization of the NDs. All NDs used in my experiments, characterized by different sizes and coatings, presented high fluorescence levels, the result of a relatively high concentration of NV center. In all NDs I observed a fast loss in coherence due to interactions between the NV centers and with the external environment. The most striking and unexpected result concerns the dynamics of the spin-lattice relaxation time T_1 . Differently from previous reports, spin dynamics after polarization of NV centers could not be described by a single exponential decay, but showed a sharp signal increase that I attribute to charge dynamics and charge conversion between the negative and neutral forms of the NV center. Unexpectedly, I found that coupled charge and spin dynamics are strongly affected by paramagnetic interactions, yielding unprecedented sensitivity to subnanomolar concentrations of gadolinium, a strong paramagnetic contrast agent. The connection between relaxation dynamics and concentration of paramagnetic species can open new perspectives in biosensing and in bioimaging. As a demonstration of a practical application, I tested the sensitivity of NDs in the detection of deoxyhemoglobin, an endogenous paramagnetic species in blood.

Keywords

Nanodiamonds, NV centers, pulsed laser ablation, metastability, paramagnetism

Acknowledgments

I have to thank many people for the closeness throughout my years in Trento. I am grateful to my supervisors, Professors Antonio Miotello of University of Trento and Angelo Bifone of Istituto Italiano di Tecnologia, for their incessant help and for believing in my abilities. I was lucky to express my creativity and improve my scientific experience with discussions and research. They contribute to both my scientific and personal growth.

I am very grateful to my current and former colleagues Massimo Cazzanelli, Nicola Bazzanella, Alberto Mazzi, Michele Orlandi, Raju Edla, Marco Bettonte, Zakaria El Koura, Loredana Schiavo and Enrico Binetti for their help and useful discussions. Thanks to Rakshyakar Giri, who patiently taught me the “tools of the trade” and expanded my fascination for the experimental world. Thanks to Carla Dorigoni, for stimulating debates and for everyday life. I am thankful to Stefano Tambalo for his support in the experimental section. I want to thank Luca Basso, for his vivacious approach to science and for working side by side. All of them gave me invaluable stimulating discussions and joyful moments spent together.

I want to thank Professor Zeno Gaburro, for his help in the very beginning of my career. A special thank to Rajeshkumar Mupparapu: I owe a lot to his experience and his friendship during the first year of my activity. I also owe some coffees and teas.

I express gratitude all the people whom I spent some time in the office with and who contributed to chill out and enjoy the days: Alberto, Adam, Denise, Nayome, Gergely, Ryszard, Valentina, Alessia, and Carola. I am also grateful to the staff of the administration offices of IIT and University of Trento for their help.

I am thankful to Dr. Claudia E. Avalos and Prof. Paolo Ossi for the revision of the thesis and productive suggestions.

Finally, I want to thank my friends, who balanced my research activity with cheerful moments, and my family, whose support throughout the years was essential for my success.

Table of contents

Abstract.....	VII
Acknowledgments	IX
Table of contents.....	XI
Chapter 1 - Introduction.....	1
1.1 Thesis outline	3
Chapter 2 - Superheated liquids: phase explosion and formation of nanoparticles....	9
2.1 Background: few notes about nucleation theory.....	10
2.2 Thermodynamics of superheated liquids and phase explosion.....	13
2.3 Modeling of phase explosion and nanoparticles synthesis	22
2.4 Results and discussion	24
Chapter 3 - Undercooled liquids: nucleation and growth of nanodiamonds.....	29
3.1 Stability of nanodiamonds and nanographites.....	30
3.2 Nucleation and growth of nanodiamonds in the metastable region.....	36
3.3 Results and discussion.....	40
Chapter 4 - Synthesis of nanodiamonds by pulsed laser ablation	43
4.1 Experimental set up	44
4.2 Results and discussion.....	47
4.3 Conclusions.....	60
Chapter 5 - Basic properties of nitrogen-vacancy centers in nanodiamonds.....	63
5.1 The basic physics of NV centers.....	64
5.2 The spin Hamiltonian	71
5.3 Experimental set up.....	76
5.4 Characterization of the NDs through optical analyses	79
5.5 Spin dynamics.....	85

5.6	Conclusions.....	94
Chapter 6 - Coupled charge and spin dynamics of T_1 relaxation in the presence of paramagnetic species.....		97
6.1	T_1 relaxometry with gadolinium.....	99
6.2	T_1 relaxometry with blood.....	110
Summary		113
Bibliography.....		115

Chapter 1

Introduction

Nanoparticles have attracted attention in the last decades for their interesting physical and chemical properties and for new potential technological applications. As an intermediate system between molecules on one side and bulk materials on the other side, nanoparticles' size-dependent properties are determined by their small volume in connection to a large surface area. Active areas of investigation include mechanical¹, optical², thermophysical³ and electronic⁴ properties of nanoparticles. Nanoparticles have been used in photocatalysis and water purification schemes⁵, in hydrogen production⁶ and storage⁷, with potential applications in the field of renewable energies. Moreover, nanoparticles may find important applications in medicine⁸ (especially drug delivery⁹) and biophysics¹⁰. Due to this growing interest, different physical and chemical techniques have been exploited for their synthesis, including sol-gel¹¹, hydrothermal methods¹², precipitation¹³ and laser-assisted techniques¹⁴. Moreover, substantial theoretical work has been performed in order to explain the formation of nanoparticles¹⁵⁻¹⁷.

Among nanoparticles, nanodiamonds (NDs) occupy a special position. NDs combine features of nanoparticles with some of the properties of bulk diamond: highest hardness and resistance to friction, high thermal conductivity, optical transparency, chemical stability and biocompatibility¹⁸.

This makes NDs a versatile tool in many fields¹⁹, including tribology, catalysis¹⁹, drug delivery, biomarkers and bioimaging^{20,21}.

Production of NDs by detonation²² dates back to the sixties. Nevertheless, NDs synthesis is still a challenge as it requires extreme pressure and temperature conditions. Several methods have been proposed, including detonation^{23,24}, high-pressure-high-temperature (HPHT) growth¹⁸, ultrasound cavitation²⁵, chemical vapor deposition²⁶, carbon dioxide reduction²⁷ and laser-assisted techniques²⁸⁻³⁰. Purification and production cost of NDs remain a problem for most of these approaches.

Importantly, NDs can be enriched with nitrogen to obtain nitrogen-vacancy centers (NV centers)^{31,32}. NV centers are point defects that can exist in two forms, the neutral NV⁰, and the negatively charged NV⁻. Even if both charged states are commonly found in NDs, the NV⁻ has attracted much more attention due to its spin-dependent fluorescence that enables ultrasensitive detection of electric and magnetic fields at the nanoscale (nano-magnetometry³³ and nano-electrometry³⁴), with applications in nano-thermometry³⁵, bioimaging and biosensing³⁶⁻³⁹. NV⁻ centers can be polarized and their polarization can be transferred to the surrounding environment^{40,41}, with potential application in NMR. Charge manipulation may allow long term data storage⁴². Finally, NV⁻ centers are single photon emitters in quantum optics⁴³ and, as a solid state qubit, the NV⁻ has been proposed as a candidate for quantum information technologies⁴⁴.

Detection of small fields requires careful manipulation of NV⁻ spin levels through combined laser and microwave pulse sequences, used in Ramsey interferometry and Hahn echo schemes. By measuring the time evolution of single NV⁻ centers, weak magnetic fields can be detected with high sensitivity (few nT/ $\sqrt{\text{Hz}}$) and sub-nanometer spatial resolution⁴⁵. Sensitivity can be further improved using ensembles of NV⁻ centers⁴⁶, but the price is the loss

of spatial resolution. In addition to that, a local probe, as a diamond of nanometric size, is affected by surface noise that reduces the coherence properties of NV^- spins, strongly limiting the field sensitivity. Practically, strongly NV^- -doped NDs have T_2^* of $\sim 0.1 \mu s$ or shorter^{47,48}, making the use of the standard sequences a hard task. In this thesis, we have explored the dependence of the spin-lattice relaxation time T_1 , which has a much longer characteristic time of few ms, on magnetic interactions. Specifically, we have demonstrated detection of paramagnetic centers by monitoring the spin relaxation dynamics. Interestingly, we found that spin dynamics and charge state conversion between NV^- and NV^0 must be considered together to fully explain the experimental findings.

1.1 Thesis outline

This thesis can be ideally divided in two parts: the first describes a novel route for the production of NDs through laser ablation of carbon materials; the second demonstrates the application of NDs to detection of paramagnetic centers. In the first section of this thesis (Chapters 2-4), we face the problem of synthesis under two perspectives, the theoretical and the experimental one. The main goal is the elaboration of a theoretical model for NDs synthesis and growth, starting from a more general model of nanoparticles synthesis. In the second section of the thesis (Chapters 5-6), we consider the applications of NV^- -enriched NDs in the detection of paramagnetic impurities in biologically relevant conditions.

More specifically, in Chapter 2 we deal with nanoparticles produced by pulsed laser deposition (PLD). Shortly, PLD relies on the irradiation of a pulsed laser on a target. The energy density, wavelength, pulse length and repetition rates vary widely depending on the application. The complicated interaction

between the laser pulse and the target comprises a large number of thermal, diffusional and mechanical processes on different timescales⁴⁹ and, as a consequence, more than one ablation mechanism. Vaporization is always present, while ejection of liquid and solid particles occurs when laser intensity exceeds threshold values. In the theoretical work we considered highly powerful ($\sim 1 \text{ GW cm}^{-2}$) laser pulses with pulse length of 20 ns. We chose these conditions to match the experimental parameters of our set-up. Under these conditions, the target quickly heats at rates of $10^{11} - 10^{12} \text{ K s}^{-1}$, and becomes a superheated liquid, approaching the critical temperature (around 90% of T_c). Fast relaxation mechanisms (i.e. electron-phonon interactions⁵⁰, on timescales of $10^{-12} - 10^{-11} \text{ s}$) thermalize the irradiated spot, so local thermal equilibrium can be assumed upon melting. In this metastable liquid, homogeneous nucleation of vapor bubbles is the main mechanism appointed to the phase transformation⁵¹. The change in phase from a metastable liquid to a “foamy” mixture of vapor bubbles and percolated liquid occurs at dramatic rates, taking therefore the name of explosive boiling or phase explosion⁵². Under vapor generation and expansion, the liquid nanodomains are pushed away from the target, together with vapor and ions, in an expanding plume. The nanodroplets assume a spherical shape by minimizing the internal energy⁵³ and can then be collected on a substrate.

In this thesis, we model phase explosion by considering a continuum thermodynamic model^{54,55}. Accordingly, thermodynamic variables describing the system are considered to behave as continuous functions of temperature up to the critical point. At the same time, fluctuations are modeled through the definition of a nucleation frequency, representing the average number of bubbles (or “nuclei” of the new phase) arising per unit time in a unit volume. Even if continuum models are led to the limits of their validity⁵⁶ in the near-critical region, they are more accessible and scalable⁵⁷ than simulations based on molecular dynamics.

The starting point is then an outline of the thermodynamics and kinetic theory of metastable liquids. The general treatment is intended to hold for both superheated and undercooled liquids, the two metastable systems considered largely in this thesis. Physical quantities that play a role in the phase change, as the critical radius and the nucleation rate are introduced. In a second step we define the main thermodynamic parameters and their temperature dependence close to the critical point. The goal is the modeling of phase explosion to link the bubbles-saturated liquid geometry with the size distribution of nanodroplets ejected from the target, and with the vapor/liquid fraction of ejected material⁵⁴. This was accomplished with the aid of Monte Carlo simulations for a set of metals, finding excellent correspondence between experiments, theoretical predictions and molecular dynamics simulations.

Based on these results we move on focusing more specifically on carbon. The peculiarities of carbon, reflected also in the phase diagram, are emphasized whenever possible and compared with results previously found.

In Chapters 3 and 4 the attention is focused principally on the pulsed laser ablation (PLA) of graphite and the structural change from a graphitic sp^2 to a diamantine sp^3 structure. The ablation of graphite is considered to occur in a cryogenic liquid, water or liquid nitrogen, adding a fast cooling mechanism (again, $10^{11} - 10^{12} \text{ K s}^{-1}$) to the picture. Henceforth, undercooled liquid carbon is considered, in a somewhat "specular" fashion with respect to the superheated liquids of the previous chapter.

The most interesting feature of undercooled liquids is the possibility to solidify preferentially in metastable crystallites instead of forming the true stable phase. This phenomenon, known as phase selection^{58,59}, has been observed in different metals and salts⁶⁰, and in particular in the low pressure, low temperature synthesis of diamond (metastable compared to graphite).

This apparent paradox can be explained by considering the additional effect of surface energy and surface stresses, that rise the pressure inside the nanocrystal and make diamond the true stable phase⁶¹. In Chapter 3, we take on the problem of relative stabilities of NDs and nanographites, and identify the conditions ensuring preferred nucleation of NDs, in the stable region of macroscopic graphite. As a result, we propose a size-dependent modified phase diagram of carbon, accounting for NDs-graphite coexistence lines. Later we consider explicitly nucleation of NDs in undercooled liquid and growth of diamond seeds in the liquid environment. By considering the dynamics of the liquid transient phase and the crystal growth velocity, it is possible to extract the final size of NDs obtained with PLD synthesis.

The theoretical results of Chapter 3 are particularly meaningful when compared to experiments, presented in Chapter 4, in which we give a detailed description of our experimental set up and of the whole process of synthesis. Single crystals and sub-micrometric cluster NDs have been successfully synthesized through UV pulsed laser irradiation of raw graphite in deionized water⁶². Further, we describe a new procedure for graphite removal based on sonication and UV-irradiation of NDs powders in H₂O₂, ensuring safer handling and treatment compared to common procedures that rely on strong boiling acids. In order to characterize our powder, we employed different analytical techniques: scanning electron microscopy (SEM) and energy dispersive spectroscopy (EDS), electron diffraction and Raman spectroscopy. The result of the analyses is the understanding of the thermodynamic path allowing the synthesis of compressively strained NDs, mediated by a metastable liquid phase. At the end of the chapter we provide comparison between theoretical predictions and experimental results. We also contextualize our results in the current research field, by comparison with other available experimental data, and raise questions about the role of laser wavelength and pulse duration.

The second section of the thesis (Chapters 5 and 6) is entirely devoted to the characterization and application of fluorescent NDs enriched with NV centers. The NDs we used are commercially available, and come in two different sizes, 40nm and 100nm, bare or coated by a thin layer of silica. These NDs present strong emission, due to the high concentration of NV centers, potentially an advantage for bioimaging applications. However, interactions between NV centers and with other defects may affect coherence times, thus limiting their use as sensors of the magnetic properties of the environment at a nanoscopic scale. From a more fundamental point of view, the high density of NV centers might open new perspectives in the study of ensemble interactions and collective dynamics^{63,64}.

Chapter 5 reports a thorough characterization of the spectroscopic and magneto-optical properties of NV centers in NDs. In the first part of the chapter, we present a brief theoretical introduction with a description of the Hamiltonian that describes the relevant interactions^{31,32,65}. The experimental section reports a series of experiments, including photoluminescence, optical detection of magnetic resonance (ODMR), Rabi oscillations, Ramsey interferograms and spin-lattice relaxation measurements.

The experiments showed very short T_2^* and a fast decoherence dynamics for NV^- centers in all samples. Interestingly, however, the spin-lattice relaxation time T_1 proved to be much longer, up to hundreds of μs , and potentially a useful reporter of the magnetic properties of the surrounding bath^{66,67}. Moreover, T_1 can be evaluated after optical initialization of the NV centers, without further manipulation involving microwaves. This is particularly important for the study of biological tissues, for which microwaves can be extremely harmful.

Driven by these promising observations, in Chapter 6, we applied T_1 relaxometry to the study of paramagnetic gadolinium surrounding the NDs.

Gadolinium is a contrast agent used in MRI and a good model system to test the sensitivity of this method. In the first part of the chapter, we describe the experimental set up; experimental results are shown and discussed in the subsequent sections. Unexpectedly, we found a complex dependence of the relaxation curves on Gadolinium concentration, pointing to multiple mechanisms that contribute to the evolution of the NV states under interactions with the paramagnetic agent. This phenomenon, not previously reported, can be described in terms of coupled spin and charge dynamics, both sensitive to the external environment. Indeed, optical pumping, used to polarize the NV centers, can also change their charge state and induce photoionization and recharge mechanisms⁶⁸⁻⁷² between NV^- and NV^0 . This phenomenon is particularly apparent at high concentrations of Gadolinium, when T_1 magnetic relaxation times become very short. Finally, we describe T_1 measurements with NDs in blood, demonstrating the use of fluorescent NDs to probe the magnetic properties of deoxyhemoglobin and opening new perspectives for future improvements in a variety of bioimaging studies.

Chapter 2

Superheated liquids: phase explosion and formation of nanoparticles

The synthesis of new materials often relies on the attainment of a transient metastable phase, which acts as a precursor of the new phase. It was found that a metastable phase can favor the synthesis of new materials which would be otherwise difficult to obtain^{73,74}. In turn, metastable phases require extremely fast heating or cooling (up to 10^{12} K s^{-1}) over short timescales (nanosecond down to femtosecond regime). Pulsed laser ablation (PLA) and pulsed laser deposition (PLD) in different media satisfy both requirements under proper conditions.

In the first part of this chapter (Section 2.1) we consider the dynamics of homogenous nucleation of vapor bubbles in a superheated liquid, a phenomenon known as explosive boiling or phase explosion. This phenomenon is expected when the metastable liquid overcomes the binodal line and approaches the spinodal line, beyond a value of temperature of about 90% of the critical temperature T_c . Phase explosion, alongside vaporization and spallation, is a mechanism involved in the laser-assisted

ablation of targets⁷⁵. It is however the most efficient mechanism for short laser pulses (in the nanosecond to femtosecond range)⁷⁶, leading to the ejection of liquid nanodroplets, which, upon solidification, turn into nanoparticles.

Starting from the description of thermodynamic properties of liquids in the near-critical region and the homogeneous nucleation dynamics (Section 2.2) it is possible to model the development of a dense-packed distribution of vapor bubbles and liquid intervolumes. The rupture of the surface, driven by the high pressures involved, give rise to a distribution of liquid nanodroplets. The aim of the model is to obtain information about the nanodroplets size distribution and the content of vaporized atoms (Section 2.3). The framework of the model is a continuum approach, given its simplicity and scalability up to large volumes^{54,55}.

Since the continuum approach provides a good starting point for the description of nanoparticles (NPs) synthesis it is adopted also for carbon. The peculiarities of carbon are introduced in this chapter and will be examined deeply in Chapter 3 and Chapter 4.

At the end of this chapter we show that the theoretical predictions of the continuum model are in good agreement with results of both atomistic simulations and experiments.

2.1 Background: few notes about nucleation theory

Metastability is a thermodynamic concept describing, in our case, the behavior of superheated and supercooled liquids. Thermodynamics alone,

however, does not characterize completely the appearance of a new phase. The event of nucleation and the lifetime of the metastable system can change by many orders of magnitude and a kinetic theory is required to depict the effectiveness of formation of a new phase. In this section we give few notes about the thermodynamics of the homogeneous nucleation of a new phase and introduce the kinetic variables involved in the process^{77,78}.

Classical theory of homogeneous nucleation defines the important variables of the process: the critical radius (the size of a nucleus of the new phase at equilibrium with the surrounding metastable liquid) and the frequency of nucleation (the rate of formation of critical radii per unit volume). Following on this theory, the internal energy of the metastable liquid before the nucleation is

$$U_0 = TS - pV + \mu N \quad (2.1)$$

where T , S , p , V , μ and N are temperature, entropy, pressure, volume, chemical potential and number of molecules in the liquid. The appearance of a small nucleus of the new phase is accompanied by a change in the internal energy

$$U = TS' + TS'' - pV' - p''V'' + \mu N' + \mu''N'' + \sigma a \quad (2.2)$$

where the primes refer to the liquid and the double primes to the new phase, σ is the surface tension and a the surface area of the nucleus. The system is supposed to be in contact with a thermal reservoir at temperature T and a work reservoir that applies a constant pressure p . If the system is isolated and the process is reversible the total entropy, volume and number of particles (system + reservoir) are constant. The difference $U - U_0 = W$ is the work needed to create the new phase. Since T and p are constant, it gives also the variation of the Gibb's free energy, $W = \Delta G$. Finally, by considering all the conditions and constraints, this variation can be written as

$$\Delta G = 4\pi r^2 \sigma + (p - p'') \frac{4}{3} \pi r^3 + (\mu''(T, p'') - \mu'(T, p)) N'' \quad (2.3)$$

in which the nucleus is assumed spherical. The first term on the right side of eq 2.3 is the energy required to create the liquid-vapor interface, the second the volume work against the pressure forces, the third is the "molecular" work, or the energy in excess in the liquid phase. The third term is negative and always balances the second term, which can be positive. In fact, if the nucleus is incompressible

$$\mu''(T, p'') - \mu''(T, p) = v''(p'' - p) \quad (2.4)$$

with v'' the volume per molecule of the new phase. So

$$\frac{4}{3} \pi r^3 (p - p'') + (\mu''(T, p'') - \mu'(T, p)) N'' = \frac{4}{3} \pi r^3 \frac{\Delta\mu(T, p)}{v''} \quad (2.5)$$

and finally

$$\Delta G = 4\pi r^2 \sigma + \frac{4}{3} \pi r^3 \frac{\Delta\mu(T, p)}{v''} \quad (2.6)$$

where $\Delta\mu(T, p) = \mu''(T, p) - \mu'(T, p) < 0$ for pressures p below the equilibrium pressure p_{eq} . The eq. 2.6 has two terms, one corresponding to a volume "bulk" free energy variation, which is negative, and another positive one corresponding to the creation of the interface. For large radii $\Delta G < 0$ and the growth of the new phase is thermodynamically favored. For small radii $\Delta G > 0$ and the new phase tend to collapse. This intermediate region behaves as a potential barrier, whose height decrease with increasing metastability of the liquid. The maximum of the curve defines the critical radius:

$$r_{cr} = \frac{2\sigma v''}{-\Delta\mu} \quad (2.7)$$

and the critical energy

$$\Delta G_{cr} = \frac{16\pi}{3} \left(\frac{\sigma^{3/2} v''}{-\Delta\mu} \right)^2. \quad (2.8)$$

The rate at which critical nuclei appear is indicated by J , the homogenous nucleation rate. From to the early works of Volmer and Weber to more refined theories, the nucleation rate is proportional to the energy barrier in the sense

$$J \propto \exp\left(-\frac{\Delta G_{cr}}{k_B T}\right). \quad (2.9)$$

Given the dramatic dependence of J on the temperature, through the exponent ΔG_{cr} , a liquid can pass from an apparent situation of stability to a strong nucleation regime within a small range of temperatures. In the next section the homogeneous nucleation of vapor bubbles inside superheated liquids is considered more in detail.

2.2 Thermodynamics of superheated liquids and phase explosion

We considered initially homogeneous nucleation in superheated liquids, a process often defined explosive boiling or phase explosion (here the terms critical nucleus and critical bubble are used as synonyms). It involves the appearance and the growth of spherical vapor bubbles that ultimately saturate the liquid. It is useful to rewrite r_{cr} and ΔG_{cr} by explicating their dependence on pressure:

$$r_{cr} = \frac{2\sigma}{p_v - p_l} \quad (2.10)$$

$$\Delta G_{cr} = \frac{16\pi\sigma^3}{3(p_v - p_l)^2} \quad (2.11)$$

where now $p_v(T)$ and $p_l(T)$ are the pressures of the vapor and liquid phases, respectively. The nucleation rate is derived as a solution of the differential equation

$$\frac{dJ}{dt} = \frac{J_s - J}{\tau_{lag}} \quad (2.12)$$

where

$$J_s = \rho_l \sqrt{\frac{6\sigma}{(3-b)\pi m^3}} e^{-\frac{\Delta h_v}{RT}} e^{-\frac{\Delta G_{cr}}{k_B T}} \quad (2.13)$$

is the stationary nucleation frequency as reported by Skripov⁷⁷, in the form proposed by Döring and Volmer and

$$\tau_{lag} = \sqrt{\frac{2\pi m}{k_B T} \frac{4\pi\sigma p_v}{(p_v - p_l)}} \quad (2.14)$$

is the time lag, i.e. the time required for the attainment of the steady state. ρ_l , Δh_v , m and R are the liquid density, the molar enthalpy of vaporization, the atomic/molecular mass and the ideal gas constant, respectively. At constant temperature eq. 2.12 can be easily integrated to give

$$J(t) = J_s \left(1 - e^{-\frac{t}{\tau_{lag}}} \right) \quad (2.15)$$

Clearly, knowing the dependence of thermodynamic parameters close to the critical point is required in order to model the phase explosion process. However, the direct measurement of near-critical parameters is extremely difficult. To overcome this obstacle we followed the common procedure of extrapolating fits of experimental data to higher temperatures, guided by theoretical arguments about the constraints on critical exponents^{56,78,79}.

Quite recently, Blairs and Abbasi⁸⁰ considered a Lennard-Jones potential for liquid metals and gave an empirical relation between the critical temperature T_c on one side and molar volume v_m and surface tension σ_m , both evaluated at the melting temperature T_m , on the other side:

$$T_c = \sigma_m \left[\frac{m \cdot v_m}{(C \cdot v_m)^{5/6} - q} \right]^4 \quad (2.16)$$

where $m = 8.9733 \times 10^{-19}$, $q = -1.0459 \times 10^{-25}$ and $C = 1.484 \times 10^{-24}$ are fitting parameters. The estimates of T_c are listed in Table 2.1 with other thermodynamic parameters characterizing few common metals.

Element	T_m [K] ^a	T_b [K] ^a	T_c [K]	p_c [10 ⁸ Pa]	$\rho_l(T_m)$ [kg/m ³] ^a	$\sigma(T_m)$ [N/m] ^b	$\Delta h_v(T_b)$ [kJ/mol]
Al	933	2792	6319	3.2	2375	1.05	294 ^a
Fe	1811	3134	8059	5.4	6980	1.909	355 ^c
Co	1768	3200	7710	5.4	7750	1.928	375 ^c
Ni	1728	3186	7241	6.5	7810	1.834	378 ^c
Cu	1358	2835	5741	4.6	8020	1.374	300 ^c
Ag	1235	2435	5851	3.3	9320	0.955	255 ^c
Au	1337	3129	7003	3.9	17310	1.162	324 ^a
C ^d	4765	4765	6810	2.2	1613	0.32	99.2

Table 2.1– Parameters used for the thermodynamic modeling and corresponding references: melting temperature T_m , boiling temperature T_b and critical temperature T_c estimated with eq 2.16, critical pressure p_c , liquid density at the melting point $\rho_l(T_m)$, surface tension at the melting point $\sigma(T_m)$ and enthalpy of vaporization at the boiling point $\Delta h_v(T_b)$. ^a Data taken from "Lide, Handbook of Chemistry and Physics"⁸¹. ^b Values of surface tension were taken from Keene⁸². ^c Data taken from Lu and Jiang⁸³. ^d Parameters corresponding to carbon were taken from Leider⁸⁴.

A temperature dependence of surface tension was proposed in 1945 by Guggenheim⁸⁵:

$$\sigma(T) = \sigma_m \left(\frac{\theta}{\theta_m} \right)^{\frac{11}{9}} \quad (2.17)$$

with adimensional temperatures $\theta = \frac{T_c - T}{T_c}$ and $\theta_m = \frac{T_c - T_m}{T_c}$.

For the molar enthalpy of vaporization, we refer to the formula of Watson⁸⁶:

$$\Delta h_v(T) = \Delta h_v(T_b) \left(\frac{\theta}{\theta_b} \right)^{0.38} \quad (2.18)$$

and $\theta_b = \frac{T_c - T_b}{T_c}$. The formula is applicable from T_m to T_c .

Isobaric specific heat capacity for the liquid phase was approximated by a semi-empirical rule:

$$c_{p,l}(T) = c_{p,l}(T_m) \left(\frac{\theta}{\theta_m} \right)^{-0.24} \quad (2.19)$$

Similar laws exist for both the sum and the difference of liquid and vapor densities⁸⁷⁻⁸⁹. By manipulating these expressions and employing available experimental data⁵⁴ it is possible to write separately ρ_l and ρ_v in terms of two coupled power series

$$\begin{cases} \frac{\rho_l(T)}{\rho_c} = 1 + D_0\theta + C_1\theta^\beta + D_1\theta^{1-\alpha} + C_2\theta^{\beta+\Delta} \\ \frac{\rho_v(T)}{\rho_c} = 1 + D_0\theta - C_1\theta^\beta + D_1\theta^{1-\alpha} - C_2\theta^{\beta+\Delta} \end{cases} \quad (2.20)$$

with critical exponents $\alpha = 0.101$, $\beta = 0.325$ and $\Delta = 0.51$. The calculated material-dependent coefficients are plotted in Table 2.2.

The Clausius-Clapeyron line locates the boundary between the phases of liquid and vapor at equilibrium, expressing the saturated vapor pressure p_s as a function of temperature:

$$\frac{dp_s}{dT} = \frac{\Delta h_v(T)}{T[v_v(T) - v_l(T)]} \quad (2.21)$$

where v_v and v_l are the molar volumes of vapor and liquid phases. The eq. can be integrated numerically to obtain p_s . The actual pressure inside a critical bubble is⁷⁸:

$$p_v = p_s \exp \left[\frac{(p_l - p_s)v_l}{RT} \right] \quad (2.22)$$

and the liquid pressure, in turn, is incremented by the recoil effect of vaporized material. By considering the conservation of mass, momentum and energy across the vaporized layer, Anisimov⁹⁰ and later Knight⁹¹ proposed a solution for the recoil pressure of vapor, with a final outcome of $p_l = 0.55 \cdot p_s(T_s)$, the surface temperature being $T_s \approx 0.9T_c$.

Element	ρ_c [kg/m ³]	D_0	C_1	D_1	C_2
Al	634 ± 5	1.1 ± 0.2	1.75 ± 0.04	-0.17	0.08
Fe	1467 ± 53	1.8 ± 0.5	1.51 ± 0.08	-0.24	1.02
Co	≈ 1350	≈ 3.1	≈ 1.3	-0.7	2.01
Ni	2159 ± 45	1.1 ± 0.3	1.75 ± 0.04	-0.15	0.10
Cu	2363 ± 23	1.2 ± 0.2	1.82 ± 0.03	-0.27	-0.02
Ag	2718 ± 55	1.4 ± 0.3	1.68 ± 0.04	-0.57	0.06
Au	5066 ± 5	1.4 ± 0.1	1.73 ± 0.01	-0.64	-0.07

Table 2– Results of the interpolation of vapor and liquid densities. The experimental parameters needed in the calculation are reported in the first column.

Carbon has some differences with respect to the metals under consideration and requires a special analysis. First, the melting point is one of the highest for pure elements (around 4800 K). Second, melting and sublimation take place in the same range of temperatures, the only difference being the pressure: the liquid phase is stable only at high pressures. The triple point between graphite, liquid and vapor has been located at $T_{glv} = 4800 \pm 150$ K and $p_{glv} = 11 \pm 2$ MPa by laser irradiation of a graphite target in a pressurized chamber⁹². Therefore, extreme conditions are required to reach the liquid phase, as those generated during pulsed laser ablation. It is reported, in fact, that during pulse laser ablation, irradiated material can reach temperature of thousands of Kelvins⁵⁷ and pressure of several GPa⁹³, close to the thermodynamic critical point.

It is important that the thermodynamic parameters show internal consistency. Leider et al.⁸⁴ analyzed the properties of liquid and vapor carbon in the proximity of the critical point at $T_c = 6819$ K and $p_c = 223$ MPa. The author found that the vapor above 4500 K is mainly constituted by C_3 and C_7 complexes. By considering the contribution of all the carbon ions, the authors plotted a vapor-liquid coexistence curve. Additionally, the enthalpy of vaporization and the liquid density were also furnished, via the Watson relation and a Riedel equation, by considering a decrease of 20% of liquid density with respect to graphite at triple point. The critical density was found to be 0.64 gcm^{-3} . Thus, the density of saturated vapor can be estimated by reversing the Clausius-Clapeyron equation. The only missing parameter is surface tension and, to the best of our knowledge, there are no experimental available data. The Guggenheim–Katayama equation⁹⁴ relates a prefactor to critical values of T and p :

$$\sigma(T) = K(T_c p_c^2)^{\frac{1}{3}} \left(1 - \frac{T}{T_c}\right)^{\frac{11}{9}} \quad (2.23)$$

where K is a constant whose value is $\approx 2.4 \cdot 10^{-7} \text{ mPa}^{1/3} \text{ K}^{-1/3}$. At the melting point the expression gives $\sigma_m = 0.38 \text{ Nm}^{-1}$. In Figure 2.1 the relevant thermodynamic properties of carbon are plotted together with those of iron, as comparison. The temperature scale was normalized to the respective critical temperatures. Note however, that a value of $0.7T_c$ for carbon just represents the melting point, while for iron the same value refers to a moderate degree of superheating (the melting point being at $0.22T_c$). These differences are even more visible when considering the kinetic variables of nucleation.

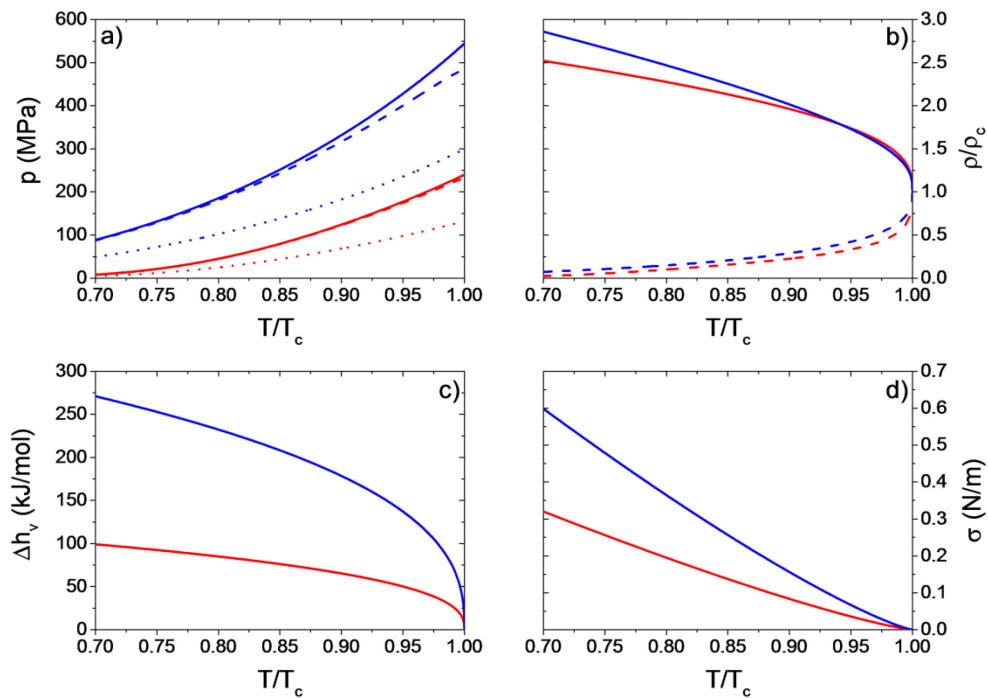


Figure 2.1– Relevant thermodynamic parameters of carbon (in red) and iron (blue). a: Saturated vapor pressure (solid line), vapor pressure inside the bubbles (dashed line) and liquid pressure (dotted lines). For carbon the vapor pressure inside the bubble is almost identical to the saturation pressure. b: Liquid density (solid line) and vapor density (dashed lines) normalized to the respective critical densities. c: Enthalpy of vaporization. d: Surface tension.

All the thermodynamic parameters considered so far have been reduced to functions of temperature only. Therefore a major assumption is whether the temperature can be considered constant in space (no gradients) and in time (no heating of the liquid). For this specific case we plot in Figure 2.2 r_{cr} , J_s , τ_{lag} , the vapor/liquid atomic ratio N_v/N_l and the phase explosion time τ_{pe} for different metals. The last quantity is defined as the time interval between the appearance of the first critical bubble and the breakout of the liquid surface, with ejection of liquid material. It is then a measure of the lifetime of the superheated liquid. If the bubbles have all the same critical volume V_{cr} the quantity has a simple analytic expression:

$$\tau_{pe} = \frac{\alpha}{J_s V_{cr}} \ln \left(1 + \frac{\eta_{max}}{1 - \eta_{max}} \frac{1}{\alpha} \right) \quad (2.24)$$

where $\alpha = \frac{\rho_l}{\rho_v}$ and η is the vapor bubble packing fraction $\frac{V_v}{V_{tot}}$, i.e. the fraction of vapor bubbles volume over the total volume. Monte Carlo simulations⁵⁴ show that the packing fraction increases with time and reaches a maximum value of $\eta_{max} = 0.30$. This value can also determine the vapor/liquid atomic ratio:

$$\frac{N_v}{N_l} = \frac{1}{\alpha} \frac{\eta_{max}}{1 - \eta_{max}} \quad (2.25)$$

Note that $N_v/N_l \approx 0.3$. It only takes into account the vapor in the bubbles and does not consider the atomic yield due to other concurrent ablation mechanisms, as vaporization.

Even if the thermodynamic parameters can have some uncertainty, the kinetic variables behaviors (Figure 2.2) are common to many materials: the critical radius goes to zero with increasing temperature superheat and so does the critical work. In a temperature interval of 200 – 300 K the steady nucleation frequency has a major variation of $\sim 14 - 15$ orders of magnitude. τ_{pe} has a large variation in a very narrow temperature interval. On the

contrary, τ_{lag} varies by a factor 10 in the same range. For low degrees of superheating $\tau_{lag} \ll \tau_{pe}$ and the nucleation can be assumed stationary. We see in Section 2.4 that also for higher degrees of superheating the time lag has a minor effect in the nucleation process.

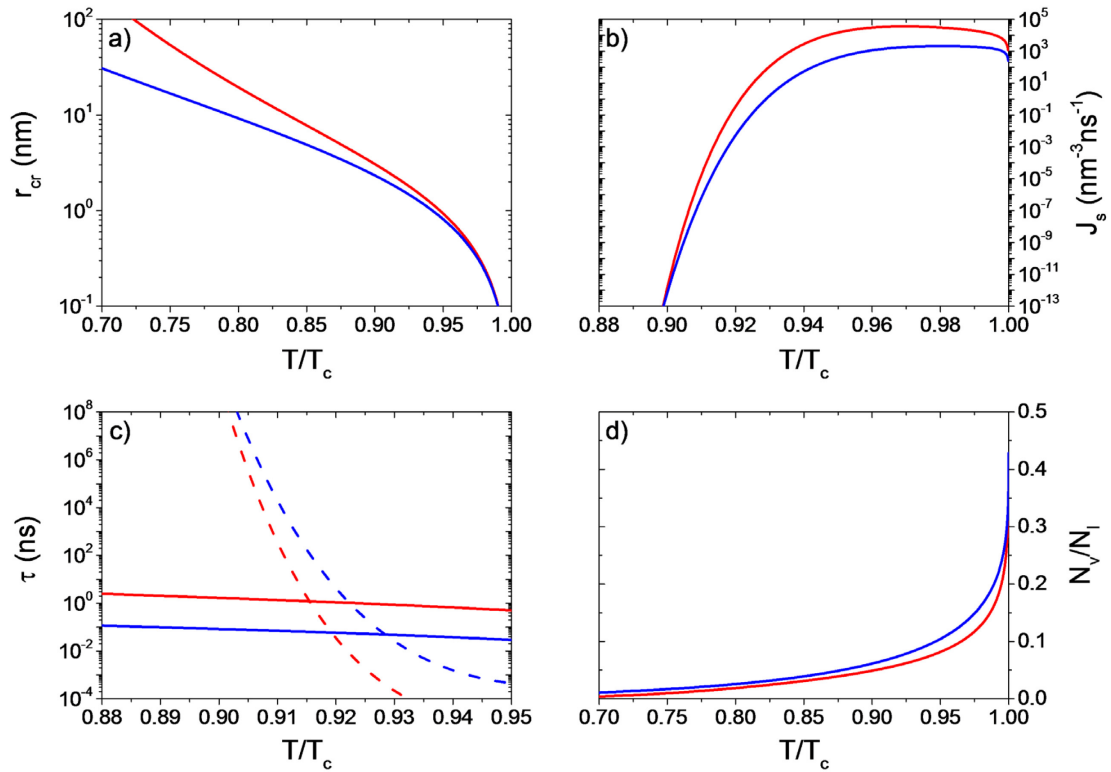


Figure 2.2 – a: critical radius, b: nucleation frequency, c: τ_{lag} (solid line) and τ_{pe} (dashed line), d: vapor/liquid atomic ratio for carbon (red curves) and iron (blue curves).

2.3 Modeling of phase explosion and nanoparticles synthesis

Our main goal in the study of phase explosion is the possibility to extract useful information about the size distribution of the ejected droplets and the fraction of nanoparticles over the total ablated material. Physically, when the liquid is filled with a dense packing of spheres, pressure gradients lead to the ejection of liquid volumes, which arrange in spherical nanodroplets, and vapor. To model this phenomenon we employed Monte Carlo (MC) simulations, based on positioning supercritical spheres, calculated with eq. 2.10, in a large control cubic volume. Computations show that a packing fraction of $\eta_{max} = 0.30$ corresponds to a situation of dense packing, with a “foam” of bubbles in contact with each other and percolated liquid. For this reason, when η reaches the value of 0.3 the simulation interrupts and an algorithm assigns a spherical volume to proper liquid intervolumes. Details of the simulation and the algorithm are reported elsewhere⁵⁴. Figure 2.3 shows an easily viewable 2D analogous of the 3D simulation.

A more refined theory should lift few assumptions of the previous model, as the constant temperature and the steady nucleation, and consider explicitly the growth velocity of bubbles. In this improved model, a number $dN = JV_l dt$ of bubbles is randomly generated in the residual liquid volume V_l in a time interval dt . All the thermodynamic parameters and the kinetic variables depend on temperature, which increases with time at a constant rate of $\frac{dT}{dt} = 10^{11} - 10^{12} \text{ K s}^{-1}$. These values are compatible with a high power ns laser heating the target. In particular, the nucleation rate is not constant in time and can be found by numerical integration of eq. 2.12.

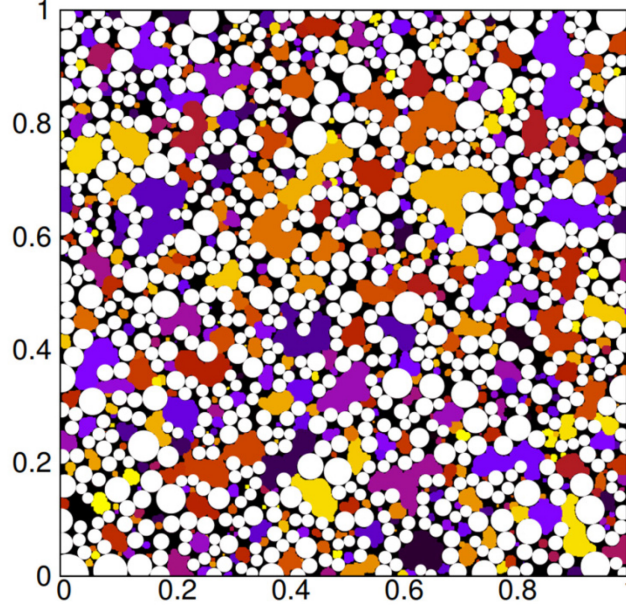


Figure 2.3: 2D simulation of homogeneous nucleation: supercritical bubbles in white and liquid intervolumes with different colors.

The growth dynamics of a single bubble in a superheated liquid was considered experimentally^{95,96} and explained with use of semi-analytical and computational models^{97,98}. A system of coupled equations considers both the work of expansion of the bubble and the heat exchange with the surrounding liquid:

$$\left\{ \begin{array}{l} R \frac{d^2 R}{dt^2} + \frac{3}{2} \left(\frac{dR}{dt} \right)^2 = \frac{p_v(T) - p_\infty}{\epsilon \rho_l} - \frac{2\sigma(T)}{\epsilon \rho_l R} - 4 \frac{\mu}{\epsilon \rho_l R} \frac{dR}{dt} \\ \frac{\partial T}{\partial t} + \epsilon \frac{R^2}{r^2} \frac{dR}{dt} \frac{\partial T}{\partial r} = \frac{K}{\rho_l c_{p,l}} \left(\frac{\partial^2 T}{\partial r^2} + \frac{2}{r} \frac{\partial T}{\partial r} \right) \end{array} \right. \quad (2.26)$$

where R is the bubble radius and r the radial variable (in principle ranging from R to ∞), $\epsilon = 1 - \rho_v/\rho_l$, μ is the dynamic viscosity and K the thermal

conductivity, approximated with the Wiedemann-Franz law⁵⁵. Further, T_∞ and p_∞ are the temperature and pressure in the superheated liquid far away from the bubbles, while T_{sat} is the saturation temperature corresponding to p_∞ . Energy balance sets a boundary condition at the bubble interface:

$$\left(\frac{\partial T}{\partial r}\right)_R = \frac{\Delta h_v}{3K} \frac{1}{R^2} \frac{d}{dt}(R^3 \rho_v) \quad (2.27)$$

and also $T(\infty, t) = T_\infty(t)$. Initial conditions are $R(t=0) = R_c$, $\dot{R}(t=0) = 0$ and $T(r, 0) = T_\infty$.

The system of equations 2.26 is solved computationally on a discrete mesh-grid with regular spatial discretization and a variable time step⁵⁴. No initial disturbance is needed to initiate the bubble growth, differently from the case of the work of Lee and Merte. Here the temperature increases at a constant rate and therefore the critical radius decreases with time, meaning that all the bubbles spontaneously exit from metastability and start to grow.

2.4 Results and discussion

In Figure 2.4 we show a typical solution of eq. 2.26 for single bubbles non interacting with each other, in the case of Al and for a heating rate of 10^{12} K s^{-1} . The growth velocity becomes effective between 50 and 100 ps. At the same time, the growth rate must be compared with the lifetime of the liquid, which is of 80 ps in the present case. This means that the fast nucleation prevents the formation of excessively large radii and, in turn, large nanoparticles.

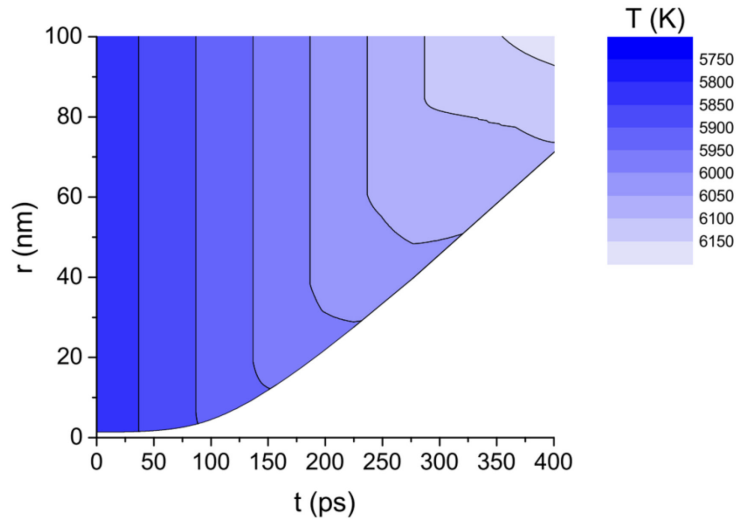


Figure 2.4: Growth of a single bubble in Al. The radius $R(t)$ is plotted as a function of time (edge of the white region). The contour plot shows the temperature field in the liquid phase in the bubble neighborhoods: it demonstrates in particular the cooling effect of the bubble upon expansion.

To be fairly general, the homogeneous nucleation occurs in a very narrow time interval, of the order of 80 – 500 ps, which corresponds to a temperature rise of 50 – 80 K, depending on the heating rate. Even if an unsteady nucleation rate was chosen, the fast nucleation process takes place without a significant time delay, as if τ_{lag} played no role. This is proven also by the observation that the bubble generation is anticipated by an order of magnitude, when the heating rate is increased by an order of magnitude.

Turning to the size distribution, we plot the number of Al nanodroplets with respect to number of atoms per nanodroplet, obtained with different heating rates, in a log-log histogram (Figure 2.5). The droplets size distributions obtained through our simulation follow the power law $f(N) \propto N^{-a}$, where N is the number of atoms per droplet and $a \approx 2$. The

power law is observed in a quite large range, from 300 to 10000 atoms per droplet. No significant variations of the parameter α is noted when going from a steady temperature (panel a, with $\alpha = 1.9$) to the high heating rates of 10^{12} Ks^{-1} (panel d, with $\alpha = 1.92$).

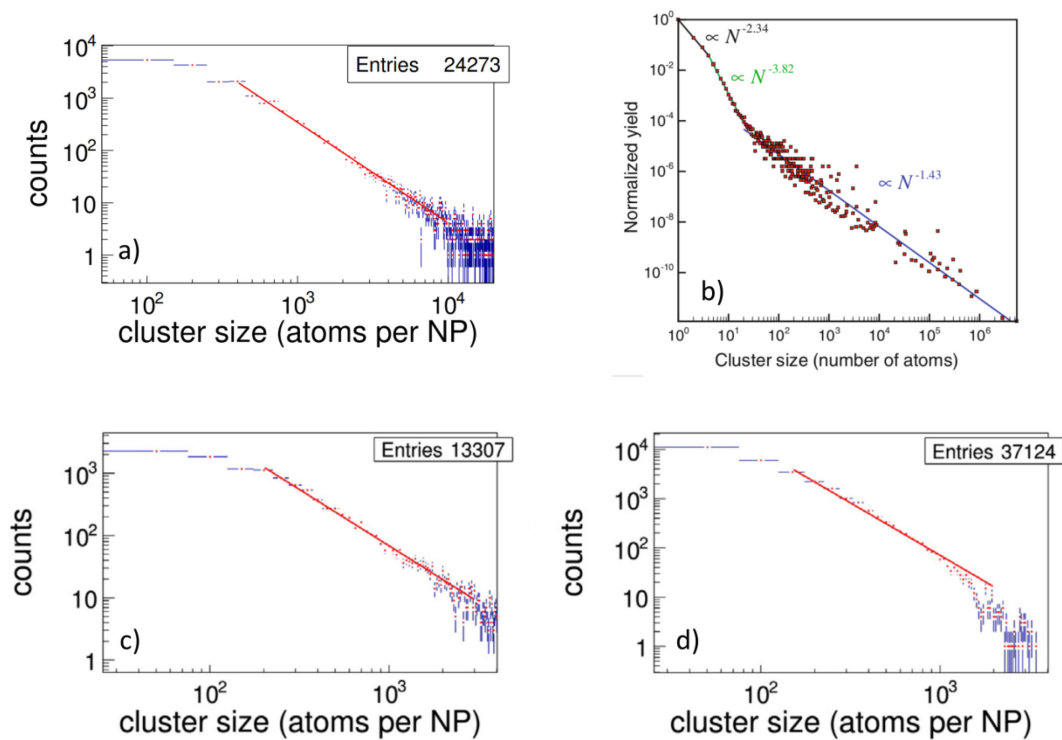


Figure 2.5 – log-log histograms of counts of nanodroplets versus number of atoms per nanodroplet, for Al under different heating rates: a, no heating, c, 10^{11} Ks^{-1} , d, 10^{12} Ks^{-1} , all based on our simulation. Panel b shows the results of a molecular dynamics simulation, reprinted with permission from Wu and Zhigilev⁹⁹, Springer-Verlag, 2013

The value of a , the average diameter of droplets \bar{d}_{drop} and the average number of atoms for droplet \bar{N}_{drop} are reported in Table 2.3. Our value of 1.9 does not differ much to the value of 1.43 found recently with molecular dynamics simulation of an Al target irradiated by a 100 fs laser pulse⁹⁹, shown in panel b. The first three rows of the table refer to Al: it can be seen from the value of the final temperature $\frac{T_f}{T_c}$ that the average diameter \bar{d}_{drop} decreases with increasing temperature, as expected. Note finally that the size distribution of radii follows the even steeper power law of $f(r) \propto r^{-3a}$, meaning that the ejected nanodroplets give rise to a narrow distribution peaked around the average diameter \bar{d} . This is the same conclusion we took by inspection of Figure 2.4: the extremely fast dynamics of nucleation or, equivalently, the short lifetime of superheated Al does not allow the formation of large NPs.

Element	$\frac{dT}{dt}$ [Ks ⁻¹]	$\frac{T_f}{T_c}$ %	a	\bar{N}_{drop}	\bar{d}_{drop} [nm]
Al ^a	--	90.8	1.9	$N_{peak} = 145$	$d_{cr} = 3.52$
Al	10 ¹¹	91.2	1.88	242	2.6
Al	10 ¹²	92.3	1.92	95	1.9
Fe	10 ¹²	93.2	1.97	73	1.7
Co	10 ¹²	93.6	1.86	81	1.8
Ni	10 ¹²	93.0	1.99	89	1.6
Cu	10 ¹²	93.3	2.05	86	1.6
Ag	10 ¹²	92.2	2.00	71	1.7
Au	10 ¹²	92.3	2.06	67	1.7

Table 2.3 – Results of our computational method. T_f is the final temperature, a the exponent of the size distributions power law, \bar{N}_{atom} the average number of atoms per nanodroplet and \bar{d}_{drop} the average diameter of the droplets. ^a Values of aluminum reported in Mazzi et al.⁵⁴ and calculated with MC algorithm for a constant temperature model with high density of percolated bubbles.

The best way to validate our theoretical prediction is by comparison with experiments. Here the size distribution predicted by our MC simulation for liquid silver heated at 10^{12} K s^{-1} is compared with the values of Through Thin Film Ablation (TTFA) of silver in high vacuum, using a KrF nanosecond laser¹⁰⁰. Our method produces a monomodal distribution, peaked at almost 2 nm. On the other hand the experimental histogram, obtained through TEM imaging, shows two components, one centered at about 2 nm and another at about 8 nm. These large particles are not observed in the simulation and could be ascribed to nanoparticles agglomeration on the substrate, a thermodynamically favored process, since coalescence reduces the free energy. This process could also be facilitated by a relatively high density of NPs on the substrate. The same tendency of coalescence, with a shift of the size distribution toward larger values, was observed when increasing the number of laser pulses, with more material deposited on the target¹⁰¹. Nevertheless, the computed size distribution is in good agreement with the first peak of the experimental bimodal distribution, proving the validity of our procedure.

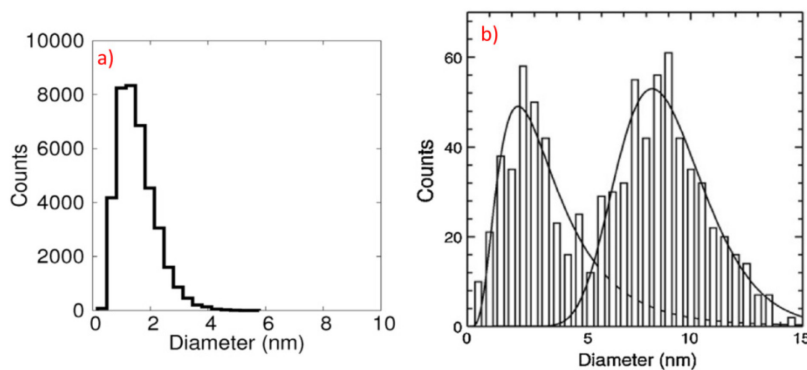


Figure 2.6 – Our theoretical prediction for Ag at a heating rate of 10^{12} K s^{-1} show a monomodal distribution for the size distribution (a). On the contrary, imaging of TTFA Ag nanoparticles using a KrF nanosecond laser¹⁰⁰ shows a bimodal distribution, the larger peak being probably due to clustering.

Chapter 3

Undercooled liquids: nucleation and growth of nanodiamonds

In this chapter we consider the synthesis of nanodiamonds (NDs). It is known that bulk diamond is the stable phase of carbon at pressures higher than 2 GPa. On this basis, many techniques for diamond synthesis rely on the attainment of high pressures, whether it is carried by a shockwave, or by constant high-pressure-high-temperature conditions^{18,22,102}. Nevertheless, chemical vapor deposition (CVD) and rapid quenching of liquid carbon demonstrated the possibility of nucleating diamond at low pressures and low temperatures, in the region of graphite stability. This apparent paradox is explained when considering the effect of surface stresses and surface energy, which rises the pressure inside the nucleating nanocrystals and make diamond the stable phase. This additional effect of surface is not exclusive of carbon and it has been observed for other metastable materials⁶⁰.

In Section 3.1 the surface effects are considered when analyzing the relative stability of a ND and a nanographite, in terms of chemical potentials. The conditions of superior stability of NDs lead to a modification of the phase diagram of carbon, where the size is displayed.

At the same time, NDs do not nucleate directly from graphite, but from a transient liquid phase. Pulsed laser ablation (PLA) of a carbon-based target (normally graphite) is a very fast process, able to generate pressures of several GPa and temperatures of thousands of K, in a timescale of few ns. Under such extreme conditions, nucleation of NDs has been reported^{73,103-106}. When irradiation occurs in a cryogenic liquid, as water or in a pressurized gas¹⁰⁷, a fast thermal dissipation can undercool the molten carbon and trigger the homogeneous nucleation of a solid phase. Direct nucleation from an undercooled liquid parental phase and subsequent growth of the crystal in the melt are the subjects of Section 3.2. In this way we can explain the observation of large crystals, in the sub-micrometer range^{106,108}. The ambiguity which still affects the triple points and coexistence lines of phase diagram of carbon seems to play a marginal role and does not modify the overall picture.

At the end of the analysis, we see that both allowed nucleation and growth in the metastable region determine the final size of NDs. The theoretical predicted size of NDs, obtained by PLA of graphite in water, will serve in the next Chapter, as it will be compared with our experimental values and with other values taken from the literature.

3.1 Stability of nanodiamonds and nanographites

Homogeneous nucleation in supercooled liquids is somehow specular to the nucleation in superheated liquids: the supercooled liquids are metastable with respect to the solid crystalline phase. The kinetic variables that we used in Chapter 2, as the critical radius, the critical work of nucleation, the nucleation frequency and the growth velocity find here an equivalent description. In particular, the Gibbs free energy variation can again be written

as a contribution of two terms, one related to bulk properties and another one to the creation of a liquid-solid interface.

There are however two important differences with respect to superheated liquids. The first is that the liquid and solid phases differ not only in density but also in degree of order. An additional energy term, associated with the crossing of the liquid-solid interface, must then be added. This term can be regarded as an activation energy for diffusion in the liquid^{109,110}. As a result, the nucleation rate of the new phase has a maximum peaked at a certain temperature and then decreases sharply with a further reduction in temperature. Below a certain threshold the system cannot nucleate a new phase and converts into glass.

The second difference is that more than a solid phase can exist. For high degrees of undercooling there are experimental evidences of a metastable phase formation instead of the true stable phase, a phenomenon known as phase selection^{58,59,111}. This high undercooling was obtained with a 25 ns Q-switched ruby laser irradiation of manganese.

In the case of diamond synthesis, which is the topic considered in this chapter, Hwang et al^{61,112} explained the apparent paradox of NDs formation at low pressures and low temperatures during CVD. ND nucleation was seen to be preferred to graphite synthesis at the pressure of 2700 Pa and at the temperature of 1200 K, in the deep region of stability of graphite. Moreover, it was also observed that NDs of $\approx 2 - 5$ nm are more stable than graphite NPs of the same size at low temperatures and pressures^{113,114}. This can be explained by considering the capillary effect: the pressure inside the nanocrystal is higher than the pressure of the surrounding and stability conditions must be revisited, as we show in Figure 3.1.

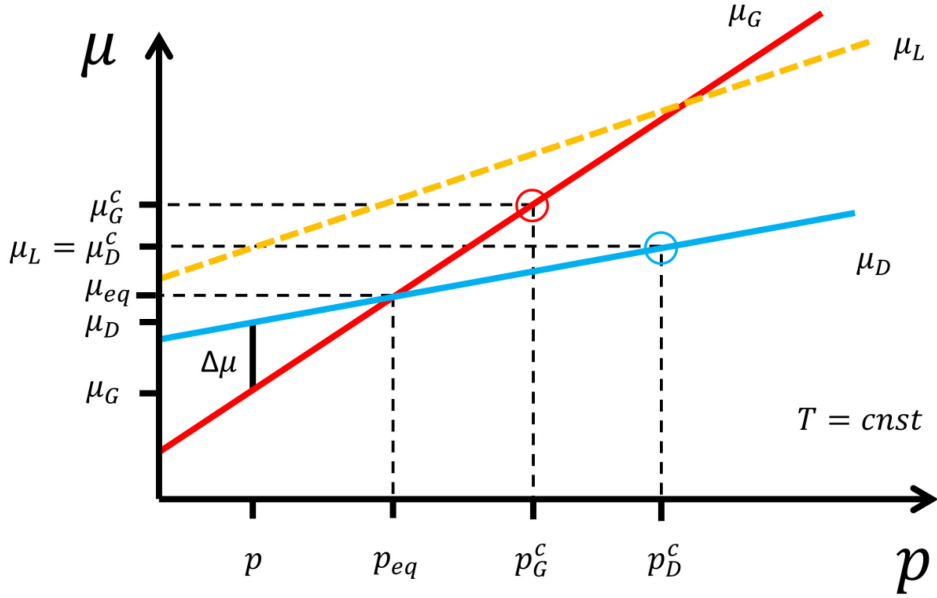


Figure 3.1 – The chemical potentials of diamond (blue line), graphite (red line) and liquid carbon (yellow dashed line) at constant temperature. Below the equilibrium line, the graphite is the stable phase. If the surface stress is considered, the chemical potentials invert and ND is more stable than nanographite (blue and red circles). The slopes of the curves give the molar volumes, assumed constant. Note that the high pressure liquid is denser than graphite^{115,116}, so its molar volume is smaller.

In the region of stability of graphite, at pressure p and temperature T , the chemical potential per molecule of graphite $\mu_G(p, T)$ is smaller than the one of diamond $\mu_D(p, T)$, so $\Delta\mu(p, T) = \mu_D(p, T) - \mu_G(p, T) > 0$. The capillary effect lifts the actual chemical potentials:

$$\begin{cases} \mu_D^c(p, T) = \mu_D(p, T) + \frac{2\gamma_D}{r_D} V_D \\ \mu_G^c(p, T) = \mu_G(p, T) + \frac{2\gamma_G}{r_G} V_G \end{cases} \quad (3.1)$$

where r is the radius of the nanoparticle, V the volume per molecule, γ the surface stress averaged on all the crystal planes and the subscript D, G refer to diamond and graphite, respectively. Incompressible solid phases were considered. Further, let us assume that the number of atoms in the nanographite N_G and in the ND N_D are the same, so $\frac{4}{3}\pi r_G^3/V_G = \frac{4}{3}\pi r_D^3/V_D$. It may happen that $\mu_D^c(p, T) = \mu_G^c(p, T)$ for a certain number of atoms in the nucleus N^* . Then

$$N^* = \frac{32\pi}{3} \left[\frac{V_G^{2/3}\gamma_G - V_D^{2/3}\gamma_D}{\Delta\mu(p, T)} \right]^3. \quad (3.2)$$

The difference in chemical potentials can be related to the exact point in the (p, T) phase diagram as

$$\Delta\mu(p, T) = (V_G - V_D)(p_{eq} - p) \quad (3.3)$$

with the graphite-diamond equilibrium line (after Bundy^{117,118}) $p_{eq} = 2.01 \times 10^6 T + 2.02 \times 10^9$. The critical diameter of the diamond nanocrystal in the conversion from graphite is

$$d_{cr}^*(p, T) = \frac{4V_D^{1/3}}{V_G - V_D} \left(\frac{V_G^{2/3}\gamma_G - V_D^{2/3}\gamma_D}{2.01 \times 10^6 T + 2.02 \times 10^9 - p} \right). \quad (3.4)$$

This means that NDs smaller than d_{cr}^* , which means with less than N^* atoms, will be more stable compared to nanographite with the same number of atoms.

As in the case of superheated liquids, we need the knowledge of the thermodynamic parameters under extreme conditions of temperature and pressure. The molar volumes are set at their values at ambient pressure and temperature, $V_G = 5.29 \text{ cm}^3 \text{ mol}^{-1}$ and $V_D = 3.42 \text{ cm}^3 \text{ mol}^{-1}$. For the surface stress, Yang and Li¹¹⁹ propose a common value of $\gamma = (\gamma_G + \gamma_D)/2$. Since

$\gamma_G \approx 1.1 \text{ Jm}^{-2}$ and $\gamma_D \approx 6.1 \text{ Jm}^{-2}$ the common value^{120,121} is $\gamma = 3.6 \text{ J/m}^2$. Finally, the expression for the critical diameter is

$$d_{cr}^*(p, T) = \frac{8.89 \text{ J/m}^2}{2.01 \times 10^6 T + 2.02 \times 10^9 - p}. \quad (3.5)$$

We plot in Figure 3.2 a modified phase diagram of carbon by taking into account the effect of size. The pressure scale is linear to emphasize the lines of 5 nm and 2 nm NDs stability, drawn with dotted lines unlike the solid lines of macroscopic equilibrium between phases. It can be seen that the model predicts the existence of nanometric diamonds in the region of graphite stability, even at room temperature and pressure, in agreement with other modified phase diagrams¹¹⁹. At the same time, the model might be improved by considering pressure and temperature dependence of the thermodynamic parameters, an overall decrease of surface stress with size⁶⁰ and additional terms in the Gibbs' free energy, as anisotropies and the energies of surfaces, edges and corners^{122,123}. Let's notice that also the liquid-diamond binodal could undergo a size-dependent shift, as suggested by Yang et al¹¹⁹. In Figure 3.2, the metastable region of diamond formation is also indicated, bounded by the analytical extension of the diamond-liquid binodal (red curve), as suggested by Basharin¹²⁴, beyond the diamond-graphite-liquid carbon (DGL) triple point (at $T \approx 5000 \text{ K}$ and $p \approx 12 \text{ GPa}$). The slope of the binodal between graphite and liquid carbon is negative, as expected from a higher density liquid, since $dp/dT = \Delta h/(T\Delta v)$. In the high pressure region the vapor phase is not displayed. The purple rectangle is the region at 8 GPa and between 3500 and 4500 K considered for the calculation of the kinetic variables of the next section.

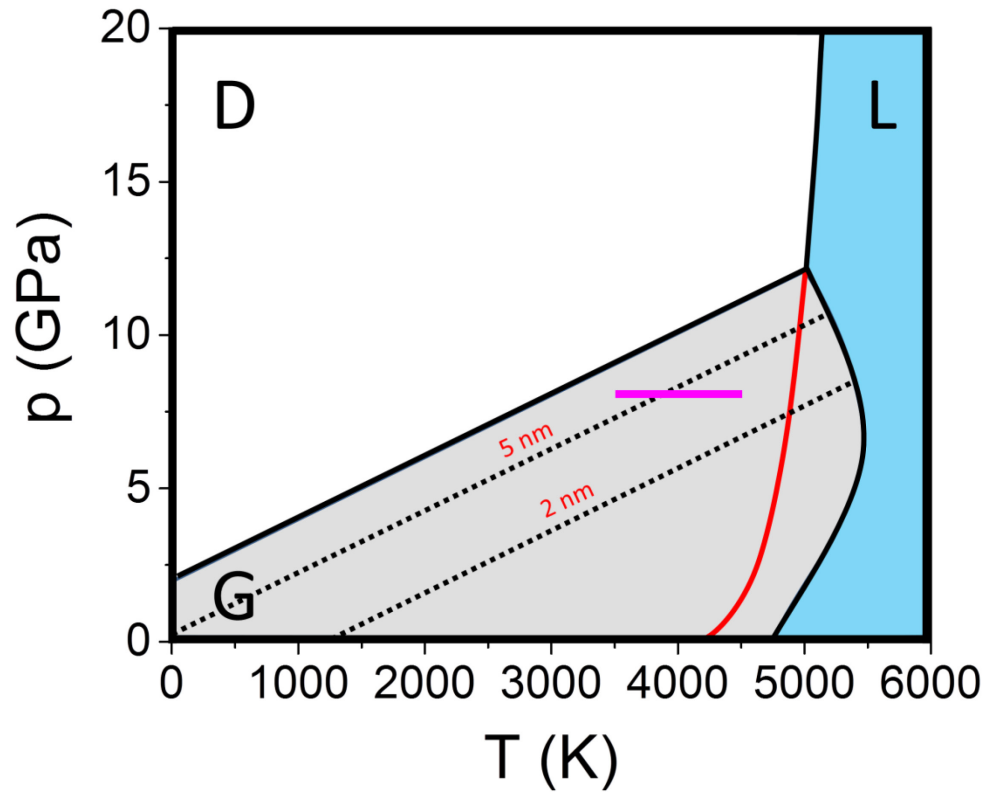


Figure 3.2 – The size-dependent phase diagram of carbon. Lines of stability of 2 and 5 nm are indicated with dotted lines. The red curve is the analytical continuation of the diamond-liquid binodal, which contains the region where nucleation of ND is favored compared to nanographite. The purple rectangle is the temperature interval at 8 GPa selected for the computation of the kinetic variables of nucleation.

Evidence of direct diamond synthesis in the metastable region was given by rapid quenching of liquid carbon, at a low pressure of 12 MPa and at a low temperature of 4160 K¹²⁴. Analogous results were reported by Narayan et al¹⁰⁶ upon single shot irradiation of melted diamond-like carbon (DLC), with a

20 ns ArF laser at fluences of $0.3 - 0.6 \text{ Jcm}^{-2}$. In this case, micrometric diamonds were synthesized, probably because the parental phase already contained a relevant content of sp^3 phase, coming from molten DLC. In both cases the undercooled liquid crossed the melting line of graphite without a phase transition, acquiring $\approx 1000 \text{ K}$ of undercooling.

3.2 Nucleation and growth of nanodiamonds in the metastable region

Under PLD NDs do not nucleate directly from graphite but from undercooled liquid carbon. The value of d_{cr}^* is important to establish whether the diamond phase is favored, but the kinetics of diamond nucleation must be determined from the comparison of the properties of metastable diamond and liquid carbon. Homogeneous nucleation of diamond occurs at constant pressure p and temperature T below the equilibrium crystallization temperature T_m corresponding to p . Then, by defining the degree of supercooling as $\Delta T = T_m - T$, the variation in chemical potential is given by $\Delta\mu = -\Delta s\Delta T$ or $\Delta\mu = -\Delta h\Delta T/T_m$, where Δs is the entropy of fusion and Δh the heat of fusion. The solid-liquid interfacial energy is temperature-dependent⁶⁰:

$$\sigma = \sigma_0(T_m) \left(\frac{T}{T_m} \right)^2 \quad (3.6)$$

with $\sigma_0(T_m) \approx 3.5 \text{ Jm}^{-2}$. The form of eq. 3.6 lowers the critical size and the critical work for nucleation. Differentiation of the Gibbs' free energy (eq 2.6) yields, for the critical radius,

$$r_{cr}(p, T) = \frac{2\sigma VT_m}{\Delta h\Delta T} \quad (3.7)$$

Pressure is buried inside the melting temperature, $T_m = T_m(p)$. Then, the work necessary to build a critical nucleus becomes:

$$\Delta G_{cr}(p, T) = \frac{16\pi}{3} \left(\frac{\sigma^{3/2} V T_m}{\Delta h \Delta T} \right)^2. \quad (3.8)$$

Turnbull and Fisher¹²⁵ in 1949 gave an expression for the nucleation rate:

$$J(p, T) = \frac{RT}{v_l h} \exp \left[- \frac{\Delta G_{cr}(p, T)}{k_B T} \right] \exp \left[- \frac{E}{k_B T} \right] \quad (3.9)$$

Where v_l is the molar volume of the liquid phase, h the Planck's constant and $E \approx 240 \text{ kJ mol}^{-1}$ the activation energy in the crossing of the liquid-solid interface¹⁰⁸. It is not easy to measure experimentally the nucleation rate J , so it is better to consider the relative efficiencies of diamond and graphite nucleations, in the metastable region. The ratio of nucleation rates depends mainly on the critical works from liquid to diamond $\Delta G_{cr}^{LD}(p, T)$ and from liquid to graphite $\Delta G_{cr}^{LG}(p, T)$, because the first exponential of eq.3.9 has the strongest variation with temperature. So

$$\frac{J_D}{J_G} \approx \exp \left[\frac{\Delta G_{cr}^{LG}(p, T) - \Delta G_{cr}^{LD}(p, T)}{k_B T} \right] \quad (3.10)$$

which means that diamond nucleates preferentially if $\Delta G_{cr}^{LD}(p, T) < \Delta G_{cr}^{LG}(p, T)$. In Figure 3.3 $\log \frac{J_D}{J_G}$ is plotted with respect to the temperature of nucleation, below the melting temperature of graphite $T_m \approx 5100 \text{ K}$, corresponding to a constant pressure of 8 GPa. The logarithm of the ratio is positive below 4400 K and down to a lower limit of 3825 K, which represents the onset of vitrification (red dashed line). This lower value was set to $0.75T_m$, in analogy with the reported vitrification range of $0.70 \div 0.85T_m$ for most of the elements¹⁰⁹. Let us notice that the approximation of equal activation energies $E_D \approx E_G$ does not change substantially the picture: even a difference of

100 kJmol^{-1} at 4000 K would just shift vertically the black curve by a value of 1.3. The critical radius of NDs is also plotted: it decreases rapidly with temperature and in the region of effective nucleation has a value of about 1 nm.

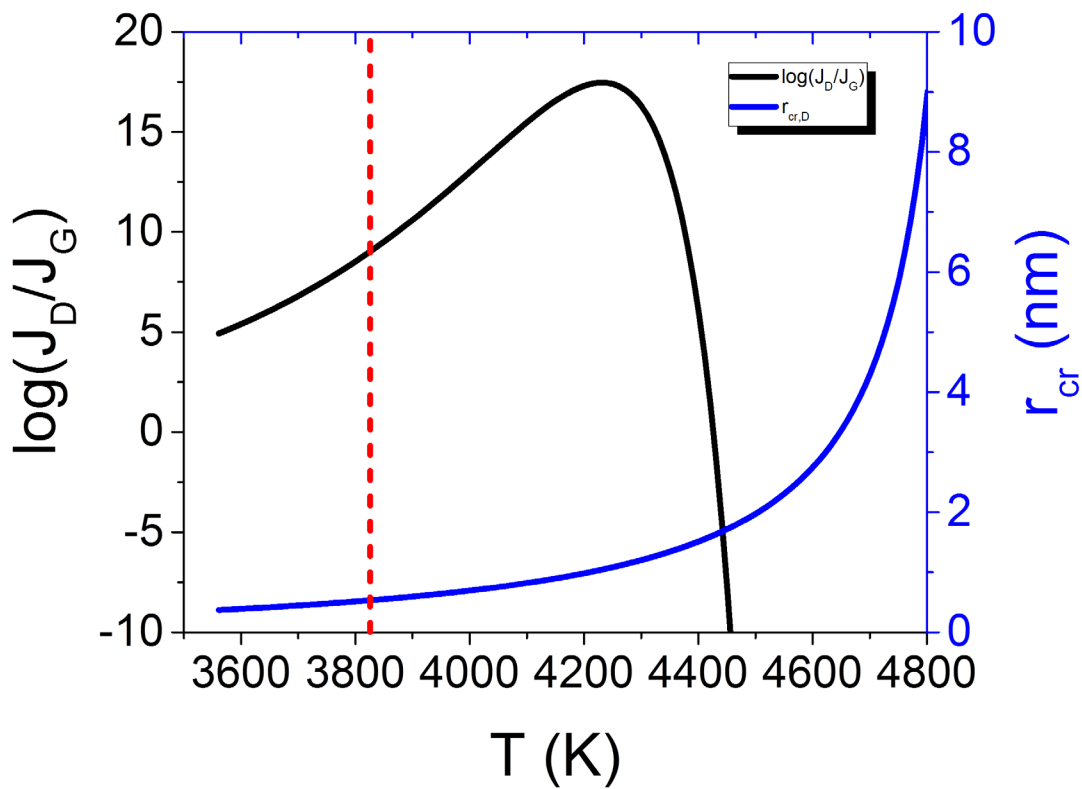


Figure 3.3 – Ratio of nucleation frequencies (black curve) and critical radius of NDs nucleated from liquid carbon at the pressure of 8 GPa. Below 4400 K (14% of undercooling), the nucleation of NDs is favored compared to nanographites. The dashed line represents the limit of undercooling ($0.75T_m$).

The size of NDs is not due only to the critical radius, but it depends mainly on the growth in the liquid parental phase. After nucleation, liquid carbon provides material for the growth of large structures^{104,106,126}, in the range of 100 nm – 1 μm. Figure 3.1 shows that both the chemical potentials of graphite and diamond lie below the line of undercooled liquid carbon. With increasing size of nanocrystals, the pressure term provided by surface stress becomes less and less important, until the difference in chemical potentials at constant pressure is the only driving force for growth. Then, a reasonable assumption is that growth can occur as long as the system remains liquid. The growth velocity is expressed by

$$v = fD\nu \exp\left(-\frac{E}{k_B T}\right) \left[1 - \exp\left(\frac{\Delta\mu}{k_B T}\right)\right] \quad (3.11)$$

where f is the fraction of sites available for attachment (supposed to be 1), $D = 0.154$ is the interatomic spacing of diamond and $\nu = 2.5 \cdot 10^{13}$ Hz is the thermal vibration frequency¹⁰⁸.

Again, the degree of undercooling determines the growth velocity. The choice of the graphite-liquid binodal also affects the growth velocity substantially. In Figure 3.4 we plot the growth velocities attributed to three different binodals, the one proposed originally by Bundy¹¹⁸, the updated version of Zazula¹²⁷ and the calculated line of Ghiringhelli¹²⁸ as a function of the degree of undercooling normalized by the melting temperature of graphite. All the three growth velocities have a maximum, because they come from the product of two terms, one related to metastability (given by $\Delta\mu$, increasing with the undercooling) and another one related to the viscosity term E (decreasing with undercooling). The peak values of the three curves are quite different. The binodal of Ghiringhelli is shifted at high pressures and low temperatures, compared to the other two, so the differences are

expectable. In the three cases the growth velocities cover the range of 0.1 – 1.6 m/s.

3.3 Results and discussion

To calculate the final diameter of NDs we made use of the formula $d_{final} = 2(r^* + v\tau_g)$ where τ_g is the time available for crystal growth. In many cases this time is of the order of magnitude of the duration of the laser pulse^{129,130}, so, as a first approximation, $\tau_g = 20$ ns, the length of our laser pulse (see Chapter 4). A cooling rate of 10^{11} Ks⁻¹ corresponds to a cooling of 2000 K in 20 ns. Such values are commonly encountered in undercooled liquids¹³¹ and are comparable with the heating rates considered in pulsed laser ablation (see Chapter 2).

From the values of Figure 3.4 and taking the constant temperature relative to the peaks, the diameters of the nucleated diamonds are of 68, 37 and 13 nm, for the Bundy's, Zazula's and Ghiringhelli's curves, respectively. These values are comparable with the biggest diamond synthesized with laser ablation techniques, given a sufficient time for the crystallization process. We must notice, however, that in this picture all the surrounding liquid is considered to turn into diamond, neglecting the concurrent mechanisms of graphitization, which is always present. In this sense, d_{final} is the "maximum" diameter that can be obtained in τ_g .

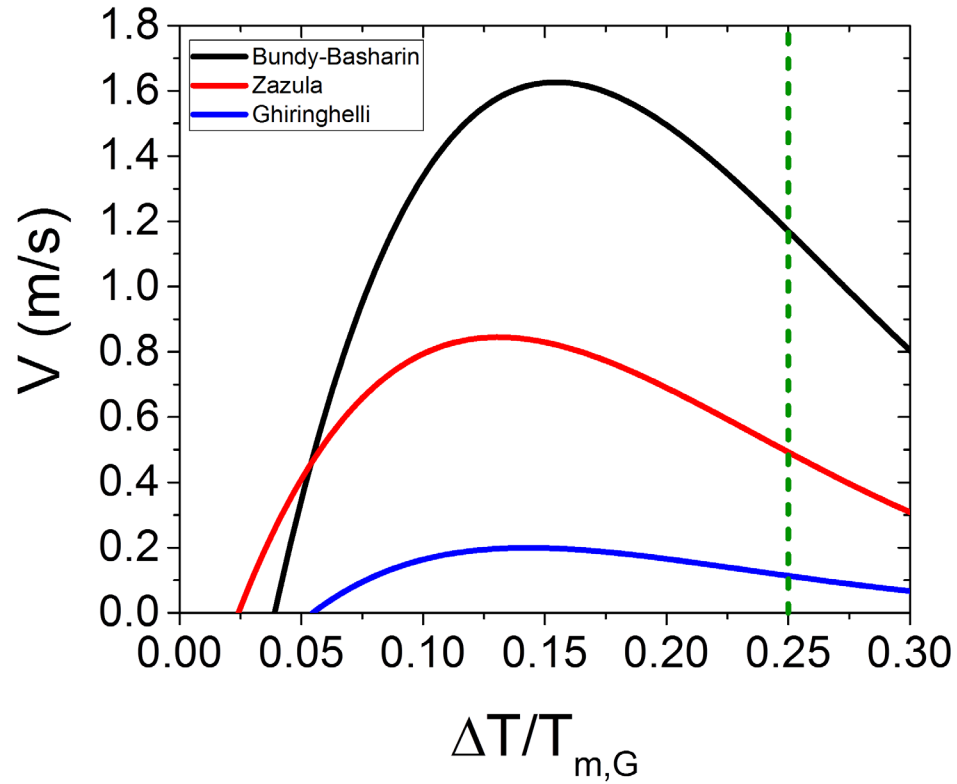


Figure 3.4 – Growth velocities of NDs in the metastable region, corresponding to different choices of binodal lines. The pressure is constant at 8 GPa. The dashed line represents the vetrification threshold, at 25% of the graphite melting temperature.

Chapter 4

Synthesis of nanodiamonds by pulsed laser ablation

In the previous chapter we focused the attention on the theoretical basis of NDs nucleation in a liquid carbon environment. As a conclusion, not only the nucleation of NDs was demonstrated to be preferred to nucleation of graphite in specific experimental conditions, but also crystal growth played an important role in the achievement of large NDs. We want now to validate the theoretical predicted values by comparison with results of experimental procedures.

The experimental work was conducted in the frame of confined pulsed laser ablation¹³² (CPLA), which relies on the focusing of a high power, short pulse laser, on a graphite target in water. If the target is immersed in a liquid during ablation, the plume expansion is dampened by the inertia of the liquid. The vaporized and ionized material is ejected with sonic velocities, so a shock wave is produced at the liquid-solid interface, with pressures of the order of GPa. In particular, the recoil pressure is of the same magnitude, much higher than those generated in vacuum¹³³⁻¹³⁶. A simple but rigorous solution to the problem of pressure evaluation is provided by the Fabbro's model, which is adopted and explained in the chapter.

The liquid has another effect on the ablated material. The high temperature plume now can transfer part of the energy to the surrounding environment through the mechanisms of heat conduction and heat convection, which are absent for the ablation in vacuum. The cooling rate is comparable to the heating rate ($\approx 10^{11} - 10^{12} \text{ K s}^{-1}$) and the molten material turns into an undercooled liquid.

In the first part of the chapter (Section 4.1), an overview of our experimental set up is given. As a distinctive feature, emphasis is devoted to confined pulsed laser ablation (CPLA) in liquid environment at room-temperature and standard atmospheric pressure, which has been recently proposed as a potentially scalable and cost effective process for the production of NDs. Specifically, we perform laser ablation of a substrate of graphite under a water layer that serves both as a confinement factor and as a medium for the suspension of the ablation products¹³⁷. Moreover, a safe physical-chemical method to extract the NDs from the surrounding graphite is developed. The NDs are fully characterized via electron and Raman spectroscopies in Section 4.2. At the end of the chapter, the obtained experimental data are explained in the framework of a thermodynamic model, introduced in chapter 3, which relies on a graphite-liquid-diamond route for the synthesis of NDs. To this purpose a comparison with experimental data taken from the literature is also performed.

4.1 Experimental set up

In our CPLA experiment, a target of graphite was ablated by a KrF excimer laser (Coherent LPX220i) with $\lambda = 248 \text{ nm}$, FWHM of 20 ns, a flat-top profile and repetition rate of 10 Hz (Figure 4.1). We chose a high number of pulses (9000 – 12000 laser shots) to increase the ablated material. Periodically the

target was moved to avoid excessive damage in the same spot and formation of craters. The energy of the laser was varied from ≈ 250 mJ to ≈ 600 mJ, and the beam was focused with a quartz lens with focal length $f = 40$ cm to fractions of mm^2 , achieving laser intensities in the range of 1–10 GWcm^{-2} . The laser spot is irregular, so the power density is averaged on the spot size. This means that the peak intensity in a smaller subregion of the spot could be higher. Due to the spatial irregularity of the laser spot, we measured experimentally the spot size on the focal plane, instead of using the equation

$$\theta w_0 = M^2 \frac{\lambda}{\pi} \quad (4.1)$$

with θ the divergence angle, w_0 the waist diameter in the focal plane and M^2 a factor accounting for the multimodal nature of the excimer beam. We assume that the water does not affect the focal distance and the intensity of the laser substantially. In fact, a thin layer of water l increases the focal length by¹³⁸

$$\Delta f \approx l \left(1 - \frac{1}{n}\right) \quad (4.2)$$

where $n = 1.38$ is the refractive index of water at 248 nm, resulting in a $\Delta f = 0.55$ mm for $l = 2$ mm. This value falls below the spatial resolution of our instruments, so the focal shift was neglected.

A liquid can also absorb partially the incident light. In the present case the absorption coefficient of water is 0.0176 cm^{-1} and then the absorption is minimal. Therefore, the only effect taken into consideration is air-water interfacial reflection, which amounts to $\approx 3\%$.

The graphite target (a disk obtained by cutting a pyrolytic graphite rod) was covered by few millimeters of ultrapure water (conductivity of $0.055 \mu\text{S cm}^{-1}$) during the irradiation. If necessary, water was added to restore

the initial level. The high energy deposited on the graphite target in the water medium created dispersed graphite particles together with embedded NDs.

After ablation, the graphite powders containing NDs were sonicated in acetone for 3 hours and then irradiated with UV light ($\lambda = 365$ nm) in a solution of concentrated hydrogen peroxide for 6 h. Shorter steps of sonication and UV-irradiation were repeated to reach the indicated time. Sonication in acetone had the effect of separating the powder that tends to aggregate. After sonication, acetone was evaporated and hydrogen peroxide added before UV irradiation. The combined chemical treatment removed some of the graphite and exposed free ND crystals. It should be noticed that this procedure, even if slower, is substantially safer and simpler than other methods to remove graphitic residues from NDs¹⁰², typically involving boiling acids (perchloric, piranha solution,...) or explosive compounds (ammonium nitrate). The UV light speeds up the dissociation of hydrogen peroxide into the strong oxidizing hydroxyl radicals $\cdot\text{OH}$. The effectiveness of this chemical treatment will emerge during the Raman analyses.

For the characterization of the product, the samples were prepared by dispersing the graphite particles embedding the NDs into ultra-pure water. A droplet of this suspension was then deposited on a clean 1×1 cm² Si wafer piece, and then soft backing was applied until complete evaporation of water.

Morphological and compositional analyses were performed using a JEOL JSM-7001F Field Emission SEM equipped with an Oxford INCA PentaFETX3 EDXS detector. SEM-EDS analyses were performed at 20 keV energy beam and 10 mm of WD to allow simultaneous acquisition of morphological images and compositional spectra.

A LabRam Aramis confocal microRaman system of JobinYvon Horiba was used for the spectroscopic characterization of the same powders deposited

on Si wafer. The two lines were provided by a He-Ne laser source ($\lambda = 632.8$ nm) and a DPSS laser source ($\lambda = 532$ nm). The signal was collected on an air-cooled multichannel CCD, with a wavenumber accuracy of ≈ 1 cm^{-1} in the range between 450 nm and 850 nm.

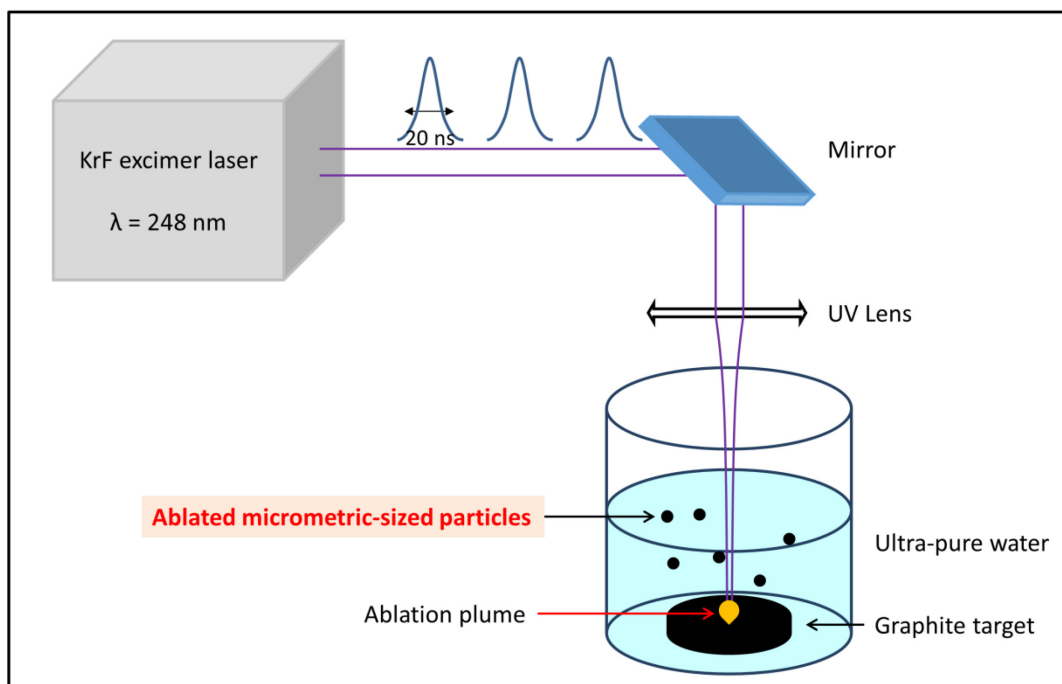


Figure 4.1 – Schematic of the CPLA process. The UV laser output is focused through a quartz lens and irradiates the pyrolytic graphite target. Ablated particles are suspended in water.

4.2 Results and discussion

As indicated in the previous paragraph, ablation of graphite occurred in water. The liquid acted as the confinement medium, where the ablated graphite particles as well as nano- and micro-clusters of assembled NDs were

dispersed. The ablated carbon powder underwent the chemical treatment described above to separate as much as possible of the graphitic phase from the NDs. After this multistep procedure, we used several analytical techniques for the characterization of the material. SEM images (Figure 4.2 b and c) clearly indicate the presence of single and clustered crystallites attributed to NDs agglomerates having a typical size in the range 0.1 – 1 μm . Both isolated and clustered crystallites were surrounded by a graphitic matrix. Energy dispersive spectroscopy (EDS, panel a) shows that the crystals are composed almost exclusively of carbon.

An electron diffraction pattern (Figure 4.2d) taken on a graphitic-embedded crystallite (panel e) exhibits reflection rings that can be indexed as (002n)g reflections of a graphite structure with an interlayer spacing of 3.45 \AA , characteristic of a disordered stacking of graphitic layers, plus reflections that are compatible with a diamond structure. Among these a large ring which can contain at the same time the 2.13 \AA periodicity ((100)g of graphite) and the 2.05 \AA periodicity of (111)d of diamond and a well defined ring of periodicity 1.26 \AA which can be indexed at the same time as (110)g and (220)d.

In order to evaluate the relative content of the carbon hybridizations, sp^2 vs sp^3 , we analyzed the ablation products with Raman spectroscopy at 633 nm and 532 nm laser excitation wavelengths. Carbon with sp^2 -hybridized bonds undergoes a double-resonant Raman scattering¹³⁹ that dominates the Raman spectrum, independently of the excitation wavelength (Figure 4.3). Ablated material displayed both the G-peak and the D-peak, indicating the appearance of disorder in the form of carbon nanoparticles. Successful removal of the graphitic component by UV treatment in H_2O_2 enabled the detection of the characteristic Raman peak of diamond at around 1332 cm^{-1} . Our samples showed a peak at 1337 cm^{-1} that is commonly attributed to compressively-strained nano-crystalline diamonds¹⁴⁰. Compressive strain blue-shifts the line of diamond¹⁴¹ from its typical position at 1332 cm^{-1} and

causes the broadening¹⁴² from $\approx 4 \text{ cm}^{-1}$ to $\approx 10 \text{ cm}^{-1}$. This observation is not surprising, as we showed in the previous chapter that the surface stress could play a role in increasing the pressure inside the NDs. The graphitic G-peak is still visible, while the D-peak is not detected. The difference in the heights of the green and red spectra is due to the higher intensity of the green line compared to the red. The peak at 1380 cm^{-1} could be due to contaminating sodium nitrate¹⁴³.

In order to explain the formation of NDs (Figs. 4.2 and 4.3) from graphite under laser irradiation treatment and water confinement, we have modeled the path in the phase diagram under the thermodynamic constraints that govern this transition (Figure 4.4). The confining medium was water in the present case (confining liquids are reported in many articles^{73,104,144,145}), while confining solid, glass/quartz, are reported by Nian et al.¹³². Regardless of the type of confinement, the CPLA can be represented as a three-step process:

- 1) First, during high power laser irradiation, a very intense plasma plume is created at the graphite-water interface and pressure and temperature reach their peak values of 1–10 GPa and 5000–6000 K, respectively^{103,133,146,147}. These values fall in the liquid region of the carbon phase diagram describing the appearance of a melt layer between the plume and graphite of the bulk target. Ejection of liquid material was also quantitatively described in the paper of Mazzi et al.⁵⁴
- 2) Upon expansion of the plume, temperature and pressure decrease. Heat is also conveyed to water and, if the cooling rate is sufficiently high, the liquid carbon becomes supercooled. At this point nucleation of NDs is initiated.
- 3) Growth of diamond nuclei continues as long as pressure and temperature favor the crystallization of liquid into diamond nuclei.

When temperature and pressure drop excessively, the surrounding carbon material turns into glassy carbon.

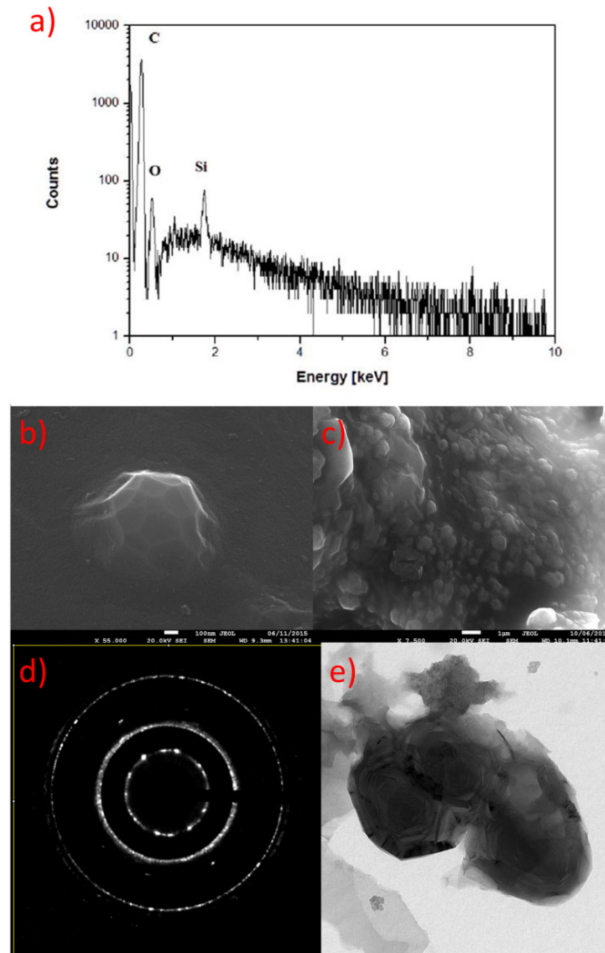


Figure 4.2 – Experimental analyses of typical crystallites of intergrown NDs and graphite. a: Single crystallite with linear size of about 800 nm and b: typical agglomerate of crystallites of 500 nm average size. Panel c shows EDS spectrum taken on crystallites as in panels a and b. The crystallites are composed by carbon and the peak of silicon comes from the substrate, where the sample powders were deposited. Oxygen is always present as a superficial contamination. Panel d displays an electron diffraction done inside the TEM apparatus on crystal shown in panel e.

The transformation process is thus in the form graphite-liquid carbon-diamond (compare to the work of X.D. Ren et al.¹⁴⁸). The presence of a liquid phase is essential, since the model considers the nucleation and the growth of diamond crystals in an undercooled liquid.

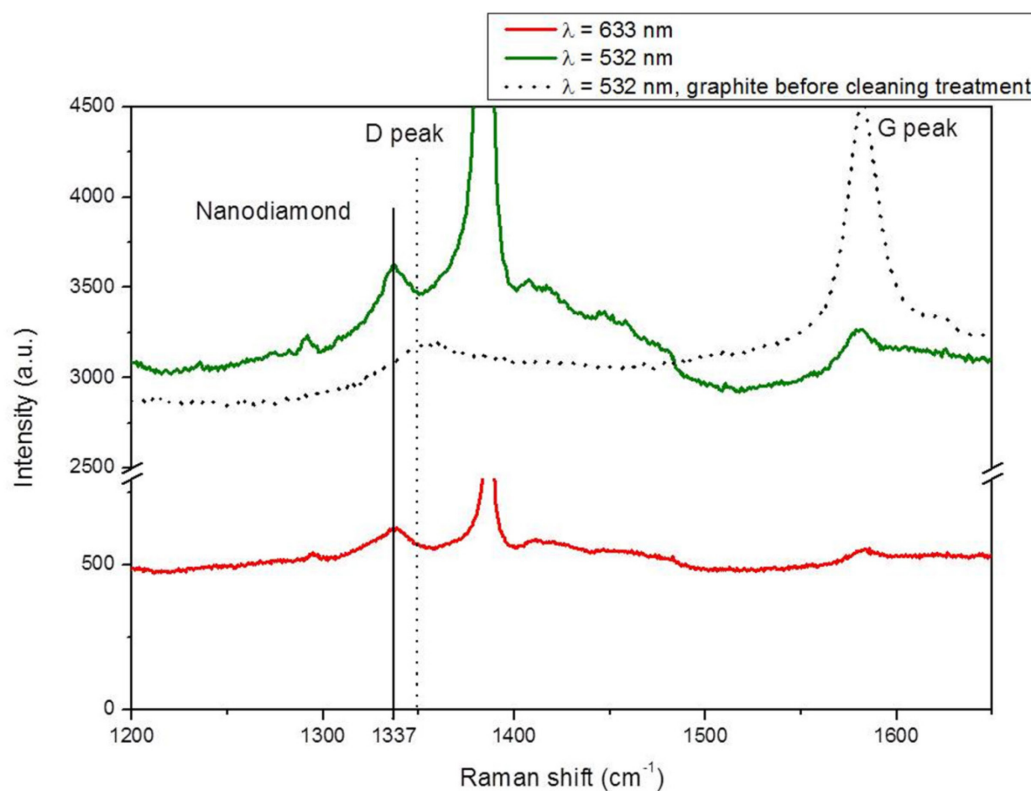


Figure 4.3 – Raman spectroscopic analyses. Raman spectra of chemically treated NDs taken at two different excitation wavelengths (green and red line), and of untreated ablated graphitic powder (dotted line). A peak at 1337 cm⁻¹ becomes clearly visible after the UV/chemical cleaning. After chemical treatment, graphite is still present with a weak peak at 1580 cm⁻¹ (the G peak), while the graphite related D peak at 1350 cm⁻¹ is not detected. The peak at 1380 cm⁻¹ comes from contaminants and was attributed to sodium nitrate.

The description of the high-power laser pulse interacting with the graphite layer, through the heat transport equation and related boundary conditions, requires knowledge of several thermodynamic and optical parameters that are not experimentally available. To avoid use of several free parameters to calculate pressure-temperature values induced in the irradiated graphite sample, we made use of a simpler model, known as Fabbro's model. This model is generally accepted for the estimation of pressure in the plume, which represents the recoil pressure acting on the graphite target¹³³. Fabbro's model is rigorously derived from the first principle of thermodynamics, under the hypothesis of ideal gas behavior of the vapor plume, and states that the evolution of pressure at the graphite-target interface depends on the intensity of the laser I . A simple solution considers a constant laser intensity I_0 during the laser pulse-length τ . Then, pressure is also constant and given by:

$$p = \sqrt{\frac{\alpha}{2\alpha + 3}} Z I_0$$

where α is the fraction of internal energy of plasma related to thermal energy, and $1 - \alpha$ the ionization fraction of internal energy (usually $\alpha = 0.1 - 0.5$). The quantities $Z = \frac{2Z_g Z_w}{(Z_g + Z_w)}$ and Z_g , Z_w are the reduced shock impedances of the system and the shock impedances of graphite and water, respectively. A number of papers^{133,146}, mostly involving foils of Al, Cu, Zn and steel immersed in water, have shown a good agreement of this model with experimental data. In particular, during pulsed laser ablation of metal targets in water, the generated plume can easily attain pressures of 1 – 10 GPa for laser intensities of 1 – 10 GW cm⁻². For the calculation of the pressure in eq. 4.3, we chose $\alpha \approx 0.25$ as in previous works^{135,149}. The shock impedances^{149,150} were taken as $Z_w \approx 1.65 \times 10^6$ kg m⁻² s⁻¹ and $Z_g \approx 12.0 \times 10^6$ kg m⁻² s⁻¹. Therefore, $Z \approx 2.9 \times 10^6$ kg m⁻² s⁻¹. In the present work, the highest value of the effective intensity of the laser was 4.5 GW cm⁻², corresponding to a

pressure of 3.17 GPa. Temperature was estimated to be in the interval of 4000 – 6000 K, as in other works^{103,147}. Actually, these conditions of temperature and pressures fall in the liquid region of the phase diagram of carbon (Figure 4.4). The pressure exerted by the plasma/plume is so high that, in the inner layers, the transition occurs from graphite to liquid carbon. There is experimental evidence¹⁵¹ of graphite melting for laser fluences exceeding the threshold of 0.6 J cm^{-2} , with a ruby laser ($\lambda = 694.3 \text{ nm}$) and 30 ns of pulse duration. The melt depth increases almost linearly with the laser fluence and reaches a value of about 200 nm for $2 - 3 \text{ J cm}^{-2}$. To the best of our knowledge there are no available experimental data for our laser fluences, in the proximity of 100 J cm^{-2} . However, analytical models that consider both vaporization and melting¹⁵² predict up to $1 \mu\text{m}$ thick melt layer at intensities of 1 GW cm^{-2} , as in our case. A thickness of several hundred nanometers is compatible with the size of our final structure (Figure 4.2).

After melting, the system undergoes cooling, because the molten graphite is in thermal contact with the bulk graphite and surrounding water, and temperature and pressure decrease abruptly. The cooling velocity of the molten graphite is expected to be as high as $10^{10} - 10^{11} \text{ K s}^{-1}$ and, in these conditions, within a few nanoseconds and in undercooling state, the system is brought into the region of stability of diamond or metastability of graphite, where the nucleation of diamond is favored^{124,153}.

To estimate the size of the NDs obtained under our experimental conditions, we looked at the theory of the homogeneous nucleation. We recall the definition of critical radius r^* (the radius of a nucleus at thermodynamic equilibrium with the surrounding liquid):

$$r^*(T, p) = \frac{2\sigma v_D}{\Delta\mu} \quad (4.4)$$

where σ is the surface energy, $\Delta\mu$ is the difference between the chemical potential of diamond μ_D and the liquid carbon μ_L and v_D is the molecular volume of diamond.

The melting temperature $T_m(p)$, depending on the pressure, is located on the binodal line, defined by the Clausius-Clapeyron:

$$\frac{dp}{dT} = \frac{l}{T\Delta v} \quad (4.5)$$

with $\Delta v = v_L - v_D$, v_L being the molecular volume of liquid carbon and $l = 125 \text{ kJ mol}^{-1}$ the enthalpy of fusion¹²⁷. We refer to the work of Ghiringhelli et al¹⁵⁴ for the evaluation of the diamond and liquid molar volumes, v_D and v_L . Surface tension is a function of both temperature and radius of NDs⁶⁰:

$$\sigma = \sigma_0(T_m) \left(1 - \frac{3D}{2r}\right) \left(\frac{T}{T_m}\right)^2 \quad (4.6)$$

with $D = 0.154 \text{ nm}$ being the interatomic spacing of diamond and $\sigma_0(T_m) \approx 3.5 \text{ J m}^{-2}$.

The final size of the crystals was mainly due to the growth of diamond nuclei in the liquid. Let us rewrite the growth velocity (eq. 3.11)

$$v = fD\nu \exp\left(-\frac{E}{k_B T}\right) \left[1 - \exp\left(-\frac{|\Delta\mu|}{k_B T}\right)\right] \quad (4.7)$$

where f is the fraction of sites available for attachment (supposed to be ≈ 1), $E \approx 240 \text{ kJ mol}^{-1}$ is the molar adsorption energy necessary to cross the liquid-solid interface and $\nu = 2.5 \cdot 10^{13} \text{ Hz}$ is the thermal vibration frequency^{108,117,155,156}. To calculate the final diameter of NDs we made use of the formula $d_{final} = 2(r^* + v\tau_g)$ where τ_g is the time available for crystal growth. In many cases this time is of the order of magnitude of the duration of the laser pulse^{129,130}, so we set τ_g to twice the pulse-length of the laser. In

the same time interval we can assume a constant pressure, equal to its peak value¹³⁵. Accordingly, the system pathway in Figure 4.4 shows a clear increase of pressure and temperature from ambient conditions to the liquid region, followed by a fast cooling at almost constant pressure. It is to be intended, of course, that this is true on average of the ablated material, while single nano- and micrometric cluster can undergo different conditions (different pathways in the phase diagram). The different lines and points refer to diamond-liquid binodals and triple points proposed by different authors (see the caption of Figure 4.4 for more details).

In Figure 4.5, the blue-dashed box represents the region in which the size of our single NDs crystals falls. These crystallites are intermixed clusters of NDs and graphite, while the size of single NDs crystallites – measured with SEM – spans the range of 30 – 70 nm and does not display great differences due to the change in laser intensity, from 2.4 to 5.2 GW cm⁻². The theoretical estimations are in reasonable agreement with the experimental data, despite the fact that the presented model considers only the thermodynamic state of the system and does not take into account laser wavelength and pulse duration, which, however, play a role mainly in the thermal history of the irradiated material.

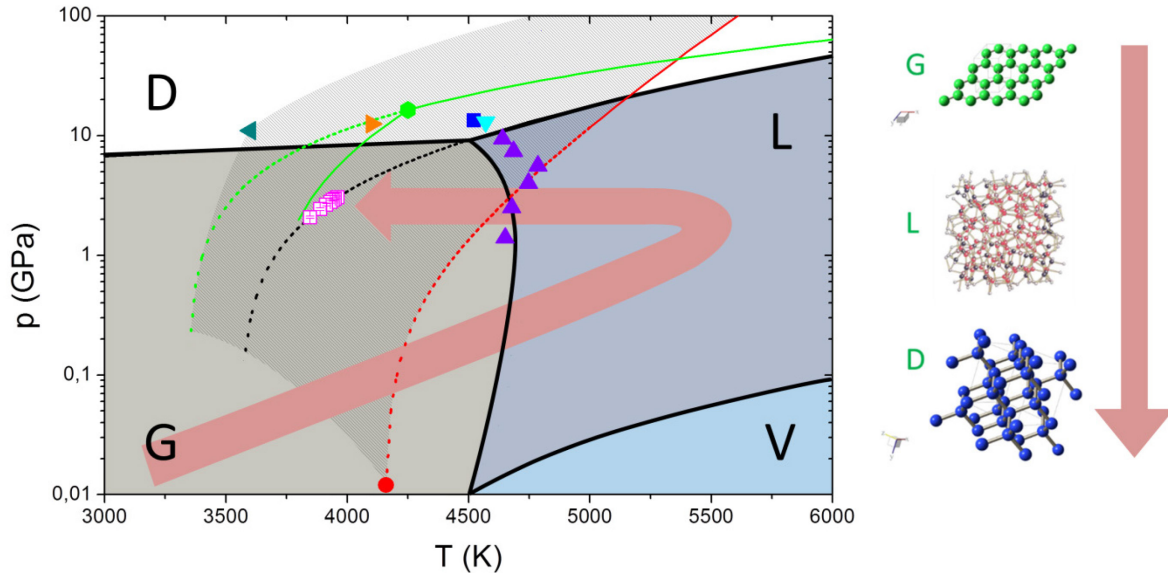


Figure 4.4 – The phase diagram of carbon. The four regions of diamond D (white), graphite G (light grey), gaseous carbon V (light blue) and liquid carbon L (blue) are separated by coexistence lines (in black¹¹⁸). The coexistence line between diamond and liquid carbon (DL-line) falls in the grey-dashed region, which is bounded by the green DL-line (Ghiringhelli et al¹⁵⁴), and by the red DL-line (as described by Basharin¹²⁴), and encloses the black DL-line (according to Zazula¹²⁷). The dashed lines indicate the analytical continuations of the three curves. The dashed lines define a stable or metastable region for diamond nucleation. The red dot represents a metastable diamond at $p=0.012$ GPa and $T=4160$ K, obtained by quenching liquid carbon¹²⁴. The purple triangles indicate the region of graphite melting measured by Togaya¹⁵⁷. The dark green leftward triangle, orange rightward triangle, light green hexagon, blue square and light blue downward triangle represent the diamond-graphite-liquid triple points (DGL-points) according to Fateeva¹⁵⁸, Bundy¹¹⁸, Ghiringhelli¹⁵⁴, Glosli et Ree¹⁵⁹, and van Thiel et Ree¹¹⁶, respectively. The purple squares describe our experimental system crossing the DL-line of Zazula from the right and becoming an undercooled liquid. Pressures of the purple squares were calculated from experimental laser intensities¹³³. The red arrow indicates the evolution of the system in our experiment: from ambient temperature and pressure to liquid carbon, then to an undercooled liquid and finally to metastable diamond and graphite.

In order to try to understand the role of the laser parameters, especially the wavelength, in determining the final NDs size, we compared our model with experimental data from the literature (graph of Figure 4.5). The colors indicate the wavelength of the exciting laser: 1064 nm for the red points, 532 nm for the green points, 355 nm for the black point and 248 nm for the blue-dashed region. We also plot three curves showing the final size single-crystal, d_{final} , due to nucleation and growth in a supercooled liquid, by considering the DL-lines of Basharin¹²⁴, Zazula¹²⁷ and Ghiringhelli¹⁵⁴. The DL binodal line has still some uncertainty. In fact, for the laser intensity of 4.5 GW cm^{-2} the final size of NDs is found to be of 5.5 nm, 15.8 nm or 59.2 nm whether we account for the DL binodals of Ghiringhelli, Zazula or Basharin, respectively. All the points relate to NDs synthesized in water by PLA. The starting material was graphite, either in the form of microparticles suspended in water^{148,160-163} or in the form of a bulk target¹⁰³⁻¹⁰⁵. Apart from the pentagon¹⁰⁵, NDs produced with IR laser are one order of magnitude smaller than NDs produced with green and UV lasers, regardless the intensity of the laser. Mortazavi et al.¹⁰⁵ compared the results of graphite ablation with an ArF 193 nm and a Q-switched ND: YAG 1064 nm laser. They argued that the ArF laser is more capable to dissociate the carbon bonds and increase the sp^3/sp^2 ratio, while the 1064 nm laser leads the formation of a variety of carbon structures, including NDs. In fact, a IR laser excites more species in the plasma plume, as the C_2 dimers, that reduce the sp^3 fraction¹⁶⁴. Further, a strong excitation of the plasma with an IR laser can induce dissociation of the confining liquid molecules, thus causing interaction of C atoms with other non-carbon ionic species and the generation of different bonds additional to sp^3 diamond bonds. The size of our single crystals seems to confirm this trend. Finally, the biggest structures (green points) are presumably intergrown polycrystals of cubic and hexagonal diamonds, according to the authors¹⁶⁵.

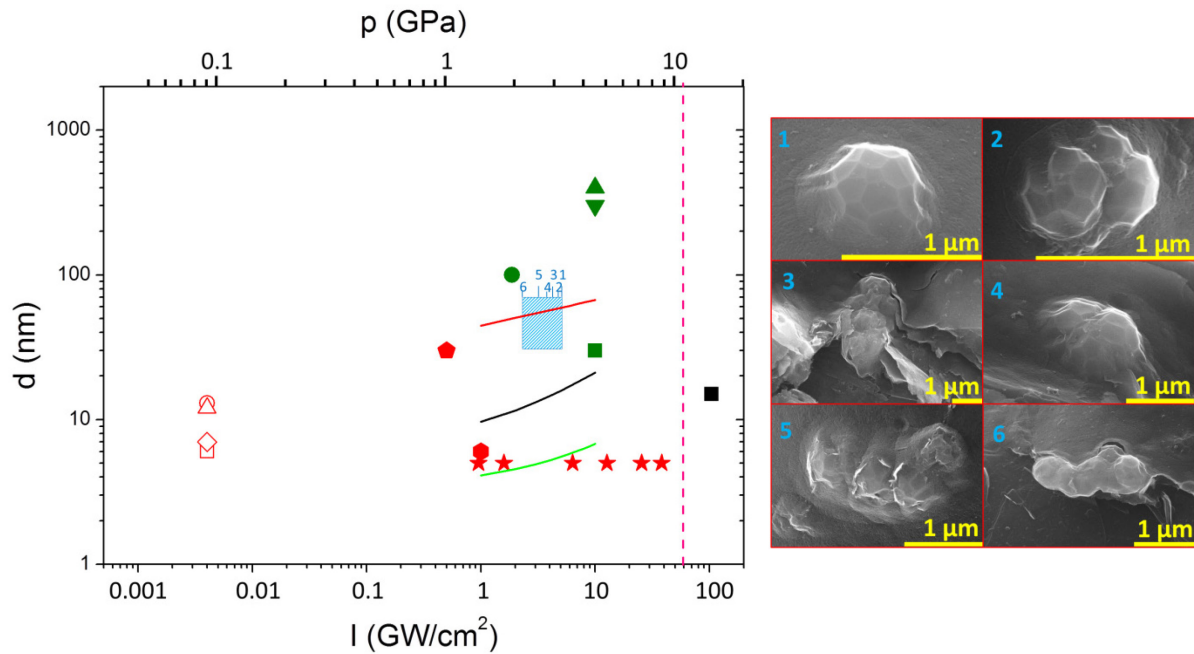


Figure 4.5 – Experimental size of NDs as a function of laser intensity. The dashed-blue box represents the region in which the size of our single NDs crystals falls. It spans a range from 30 to 70 nm, centered at 50 nm, with laser intensities from 2.4 and 5.2 GW cm⁻². This box encloses our experimental results, whose SEM images are shown in the right panels (numbered from 1 to 6). It can be seen that the size of our NDs clusters do not vary appreciably with laser intensities. Red points are taken from Sun¹⁶⁰ (empty square), Hu¹⁶¹ (empty circle), Ba¹⁶² (empty diamond and empty triangle), Ren^{148,163} (hexagon and stars) and Mortazavi¹⁰⁵ (pentagon) and correspond to ultrafine NDs produced with a 1064 nm laser. The black square was obtained with a 355 nm laser¹⁰³. Finally, the green points correspond to diamond produced with a 532 nm, taken from Yang^{104,145,165} (circle, upward triangle and downward triangle) and Wang⁷³ (square). Solid points correspond to ns laser pulses (5 – 20 ns pulse lengths), while empty points correspond to laser pulses of 0.4 – 1.2 ms. The pink dotted line indicates the threshold for the region of absolute stability of diamond at 4500 K, i.e. the temperature of the DGL triple point according to Bundy. The purple, orange and green curves represent the theoretical size of a single diamond crystal as a function of pressure for a supercooled liquid crossing the DL-lines continuations of Basharin¹²⁴, Zazula¹²⁷ and Ghirinhelli¹⁵⁴, respectively. The apparent discrepancy between theory and data may be explained by the fact that the biggest crystals experimentally observed consist of agglomerates of smaller crystals (polycrystals).

In addition to the preferential excitation of particular ionic species in the plasma, different wavelengths lead also to different energy densities in the surface layers of graphite. The Beer-Lambert law relates the laser intensity at a certain depth in the graphite with the laser intensity at the interface I_0 and depends on the penetration depth δ_λ :

$$I(z, \lambda) = I_0 e^{-z/\delta_\lambda}. \quad (4.8)$$

The calculated values of the penetration depth (from values of dielectric relative permittivity) are 45 nm for $\lambda = 1064$ nm, 31 nm for $\lambda = 532$ nm, 9 nm for $\lambda = 248$ nm and 19 nm for $\lambda = 193$ nm. The higher energy density deposited with a UV laser is expected to induce a more efficient dissociation of carbon atoms from the initial sp^2 lattice.

It must also be noticed that pulse duration seems to be a relevant parameter for the crystallization/agglomeration process. Some of the crystals are obtained by laser pulses of 0.4 – 1.2 ms (empty points in Figure 4.5). Clearly, in this case, the growth mechanism should be different from the nucleation in a supercooled liquid. Long heating time at relatively low intensity could allow the entire system to thermalize at the same temperature, with much lower cooling velocity at the end of the laser pulse.

Pressures calculated from the intensity of the laser through eq. 4.3 in our experimental conditions or in literature reports, are lower than the pressures corresponding to the region of diamond phase (Figure 4.4 and Figure 4.5). In some cases¹⁶⁰⁻¹⁶², the estimated pressure is about 0.1 GPa, much less than the 10 GPa required to have the absolute stability of diamond. Nonetheless, diamonds of various sizes were nucleated under these experimental conditions. This apparent inconsistency might have two explanations. The first is that Fabbro's model underestimates the pressures generated in the plume acting on liquid carbon, in the case of graphite. More precisely, the local pressure could be higher. This is not surprising, because of the complexity of

the problem of the laser-surface interaction in high energy-density regime. The second explanation has been given in Chapter 3: the formation of nanoscopic diamonds can occur even in the deep region of absolute stability of graphite, through the additional effects of surface tension and proximity of chemical potentials of diamond and liquid carbon (see Chapter 3).

Liquid carbon molecules make a transition toward more stable configurations. The diamond chemical potential lies between the liquid and the graphite chemical potentials: liquid carbon is driven to the diamond configuration before reaching the more stable graphitic phase. If the cooling process is sufficiently rapid, part of the system is “blocked” in the diamond phase. This last hypothesis is corroborated by the possibility of obtaining diamond at the very low pressure of 0.012 GPa at the temperature of 4160 K, by quenching liquid carbon¹²⁴. Presumably, nucleation of diamond continues as long as thermodynamic conditions are favorable, but the melted carbon surrounding the NDs solidifies into graphite or glassy carbon, creating NDs-graphite shell particles and clusters of intermixed NDs and graphite.

4.3 Conclusions

I conclude the first part of the thesis by summarize the most important results. We have demonstrated that CPLA of graphite in water under ambient conditions is a viable route to produce NDs suspended in an aqueous medium. Moreover, we proposed a simple and safe procedure to extract the NDs from the embedding graphite. The NDs produced with the presented method can be delivered in a water suspension, a formulation that is advantageous for biological applications, e.g. for administration to cell and tissue cultures. Finally, the experimental results can be explained in terms of a metastable phase (diamond) nucleating in an undercooled liquid

(undercooled carbon). This allows a robust comparison between the theoretical predicted size of NDs, based on the results of chapters 2 and 3, and the experimental results of both our procedures and other data taken from the literature.

CONCLUSIONS

Chapter 5

Basic properties of nitrogen-vacancy centers in nanodiamonds

This chapter is mainly devoted to the characterization of the properties of NV centers in commercial NDs and the understanding of the peculiarities of NDs compared to macroscopic diamonds. The NDs we used are commercially available (from Bikanta corporation), and come in two different sizes, 40 nm and 100 nm, bare or coated by a thin layer of silica. They are enriched with NV centers, to an average density of 5 ppm. For this reason, luminescence of NDs is intense, which can be an advantage in bioimaging. For the characterization of these systems we employed different spectroscopic and magneto-optic techniques, commonly adopted in the investigation of NV centers in bulk diamond as well. The experimental results are introduced by a theoretical framework describing the basic physics of NV centers and, in particular, of the ground state triplet. Far from being a thorough and complete analysis of the physics of NV in NDs, the theoretical description serves as a guideline to interpret the experiments. These, in turn, are designed to explore the sensing capabilities of fluorescent NDs, to understand their advantages and drawbacks when applied in the imaging of biological system and to study the effects of size and coating. In Table 5.1 we summarize the main characteristics of the NV -enriched NDs, as indicated by the suppliers.

Type	Diameter (SEM) [nm]	Diameter (DLS) [nm]	Functionalization
40 nm bare	42±16	107±0.8	none
100 nm bare	120±37	188±7	none
100 nm SiO ₂	120±37 core, 9±2 shell		silica

Table 5.1 – Size of NV-enriched NDs calculated by scanning electron microscopy (SEM) and by dynamics light scattering (DLS), as indicated by the suppliers. Also shown the functionalization of the surface.

5.1 The basic physics of NV centers

The NV center is a point defect in diamond that consists of a nitrogen atom and a neighboring vacancy substituting a couple of carbon atoms (Figure 5.1a). The three dangling bonds of carbon atoms provide an electron each to the center and other two come from the outer shell of nitrogen. This five-electrons configuration is the neutral form of the NV, known as the NV⁰. A sixth electron can be provided by the environment, for instance by substitutional nitrogen donors: the addition of another electron generates the negatively charged center, or NV⁻. It was reported that the balance between NV⁻ and NV⁰ depends on the concentration of substitutional nitrogen⁶⁸ and on the distance from the diamond surface¹⁶⁶, the NV⁻ being favored at high nitrogen densities and in the inner layers of diamond. Of the two centers, the NV⁻ has attracted much more attention due to the possibility of manipulating the population in the ground state sublevels, and its sensitivity to external fields, with applications in nanoscale magnetometry³³, electrometry³⁴, thermometry³⁵, and bio-imaging³⁶⁻³⁹. Furthermore, the centers can be polarized and can transfer the polarization to the surrounding environment^{40,41}, with potential application in NMR. As a solid state qubit, the NV⁻ has been proposed as candidate for quantum information

technologies⁴⁴. In this work we generically refer to the negatively charged center as the NV center, unless otherwise specified.

Nitrogen is naturally found in Type I diamonds¹⁶⁷ (up to a concentration of 0.1 – 0.2%) and in HPHT synthetic diamonds¹⁶⁸. Alternatively, nitrogen might be implanted in high purity diamond samples¹⁶⁹. Vacancies are generated during irradiation with electrons or ions and during annealing the vacancies move toward substitutional nitrogen to generate the centers^{170,171}. This second procedure allows to obtain a desired density of NV centers, from individual to ensembles, depending on the applications⁴⁷.

IR \ χ	E	C_3	C_3^2	σ_{v1}	σ_{v2}	σ_{v3}
A_1	1	1	1	1	1	1
A_2	1	1	1	-1	-1	-1
E	2	-1	-1	0	0	0

Table 5.2 – Characters of every element of the symmetry group C_{3v} are listed for each irreducible representation.

The symmetry of the system is C_{3v} , with the nitrogen lying on the symmetry axis (parallel to the \hat{z} axis) and three vertical reflection planes containing the three carbon atoms. The six elements of the group are the identity E , two rotations C_3 of $\pm 120^\circ$ and three reflections on vertical planes σ_v (one is shown in Figure 5.1a). The elements of the group can be represented by matrices acting on vectors^{32,172} describing the dangling bonds σ_1 , σ_2 , σ_3 and σ_N . Among all the representations, the irreducible representations (IRs) give the best description, since the wave functions of the system transform according to one of the possible IRs of the group, which in the present case

are called A_1 , A_2 (one dimensional) and E (two dimensional). In Table 5.2 we indicate the characters $\chi_e^{(r)}$ of the group elements in the r -th IR. Note that the two rotations, on one side, and the three reflections, on the other side, have the same characters, because they belong to the same class (and the number of classes in a group is equal to the number of IRs¹⁷³).

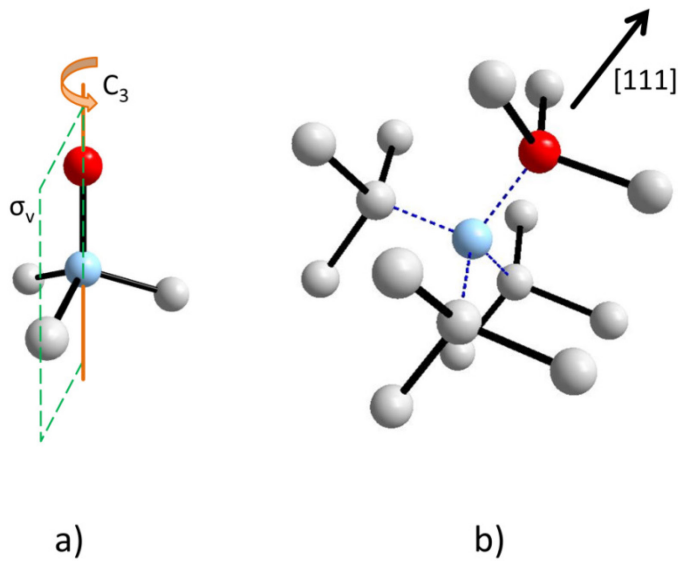


Figure 5.1 – a: schematics of an NV center, with a reflection plane σ_v and the symmetry axis C_3 . b: the center inserted in the diamond lattice. The center is aligned along one of the four $[111]$ equivalent directions.

The four single-electron orbitals φ_r are obtained from the dangling bonds σ_i by means of the projection operators $P^{(r)}$:

$$\varphi_r = P^{(r)} \sigma_i = \frac{l_r}{h} \sum_e \chi_e^{(r)} R_e \sigma_i \quad (5.1)$$

where $h = 6$ is the number of elements in the group, l_r is the order of the r -th IR and R_e the operation. Two non-degenerate totally symmetric orbitals a_1 and $a_{1'}$, transform according to the IR A_1 . Two doubly-degenerate states e_x and e_y transform according to the IR E . Explicitly³¹:

$$a_1 = (\sigma_1 + \sigma_2 + \sigma_3) + \lambda\sigma_N \quad (5.2a)$$

$$a_{1'} = \sigma_N - \lambda'(\sigma_1 + \sigma_2 + \sigma_3) \quad (5.2b)$$

$$e_x = \frac{2\sigma_1 + \sigma_2 + \sigma_3}{\sqrt{6}} \quad (5.2c)$$

$$e_y = \frac{\sigma_2 - \sigma_3}{\sqrt{2}} \quad (5.2d)$$

where λ and λ' are related to the Coulomb interaction energy. We refer to the work of Maze³² for more details.

The (energetically increasing) orbitals $a_{1'}$, a_1 and (e_x, e_y) must be filled with six electrons: $a_{1'}$ and a_1 can accommodate four (two each), so the last two must allocate in the (e_x, e_y) orbitals. Two electrons are needed to fill the shell so it is more convenient to adopt a two-holes description instead of a six-electrons one. Again, the two-holes spatial wave function must transform according to the A_1 , A_2 and E IRs. The spin can be found in a triplet ($S = 1$) or in the singlet ($S = 0$) configurations, while the total wave function must be antisymmetric. Hence, the First Hund's rule can predict the ground state configuration: it is a spin triplet (S is maximized), which is symmetric, with an antisymmetric spatial wave function, A_2 . The notation for the ground state is then 3A_2 . In Table 5.3 we list the total wave function, with the electronic configuration and the state labeling according to the C_{3v} symmetry. In the

hole notation, the ground state is indicated with e^2 and the excited state with ae .

Electronic configuration	State	State label	m_s
$e^2(T)$	$ e_x e_y - e_y e_x\rangle \otimes \uparrow\uparrow\rangle$	3A_2	+1
	$ e_x e_y - e_y e_x\rangle \otimes \uparrow\downarrow + \downarrow\uparrow\rangle$		0
	$ e_x e_y - e_y e_x\rangle \otimes \downarrow\downarrow\rangle$		-1
$e^2(S)$	$ e_x e_x - e_y e_y\rangle \otimes \uparrow\downarrow - \downarrow\uparrow\rangle$	} 1E	0
	$ e_x e_y + e_y e_x\rangle \otimes \uparrow\downarrow - \downarrow\uparrow\rangle$		0
	$ e_x e_x + e_y e_y\rangle \otimes \uparrow\downarrow - \downarrow\uparrow\rangle$	1A_1	0
$ae(T)$	$ a_1 e_x\rangle \otimes \uparrow\uparrow\rangle$	3E	+1
	$ a_1 e_x\rangle \otimes \downarrow\downarrow\rangle$		-1
	$ a_1 e_x + e_x a_1\rangle \otimes \uparrow\downarrow + \downarrow\uparrow\rangle$		0
	$ a_1 e_y\rangle \otimes \uparrow\uparrow\rangle$		+1
	$ a_1 e_y\rangle \otimes \downarrow\downarrow\rangle$		-1
	$ a_1 e_y + e_y a_1\rangle \otimes \uparrow\downarrow + \downarrow\uparrow\rangle$		0
$ae(S)$	$ a_1 e_x + e_x a_1\rangle \otimes \uparrow\downarrow - \downarrow\uparrow\rangle$	1E	0
	$ a_1 e_y + e_y a_1\rangle \otimes \uparrow\downarrow - \downarrow\uparrow\rangle$		0

Table 5.3 – Adapted from Maze *et al.*³² The states configuration is expressed in the hole notation. States are labeled with spatial and spin functions, which emphasize the triplet or singlet configurations.

The ground state 3A_2 is a spin triplet, while the excited state 3E has a more complicated structure, with total six levels. Metastable singlet states 1E and 1A_1 lie energetically between the 3A_2 and the 3E and are not accessible from the ground state through electrical dipole transitions, since the orbital wave functions are the same. Nevertheless, spin-orbit interaction couples the triplet states with the intermediate singlets with different coupling strength according to the spin projection. We will consider this interaction in detail

when measuring optically induced magnetic resonance (ODMR) in the next paragraph. Two possible wave functions of the ground state and excited state are shown in Figure 5.2a,b.

I started the characterization of our samples with the spectroscopic measurement of photoluminescence (PL), recorded with a confocal microRaman system (see chapter 4 for technical details). Figure 5.2c indicates the ground and the excited states involved in the electronic transition, with a sketch of the vibrational bands, represented for simplicity by a harmonic potential with equally spaced vibrational levels. The excitation wavelength is 532 nm. In Figure 5.2d we plot the collected luminescence of the 100 nm uncoated, the 40 nm uncoated and the 100 nm silica-coated NDs. For better comparison, the spectra were normalized to the peak intensity. In both absorption and emission, the electron transition is accompanied by the creation of phonons. Consequently, a zero phonon line (ZPL) at 637 nm is clearly visible in the emission spectra, as well as an extended phonon sideband up to 800 nm. This behavior obeys the Franck-Condon principle, which states that effective transitions between the ground and one excited vibrational state occur when the two wave functions are highly overlapped. The ZPL at 575 nm and the phonon sideband of the NV^0 are also visible.

From the fit of the NV^- luminescence we measured phonon energies of ≈ 65 meV, a value close to those reported in previous works¹⁷⁴⁻¹⁷⁷. In the case of the NV^0 , the spacing is about 40 – 45 meV. Further, the ratio between the ZPL luminescence I_{ZPL} and the total integrated luminescence I_0 can be used to estimate the Huang-Rhys factor S , defined experimentally as $-\ln(I_{ZPL}/I_0)$. The factor S gives the approximate number of phonons emitted during the optical decay. By inserting the extracted data we find $S = 3.86 - 4.07$ for the NV^- and $S = 2.76 - 3.3$ for the NV^0 . Both the values of ≈ 4 and ≈ 3 phonons for the NV^- and the NV^0 , respectively, are in good agreement with previous estimates^{176,178-180}. Within the phonon sideband of the NV^- , no major

difference is encountered in the factor S and in the spacing of phonon replica in the three spectra. This is reasonable, since the vibrational modes are quasi-local and involve few atoms around the defect^{175,176}, being almost insensitive to the - already large - size of the NDs.

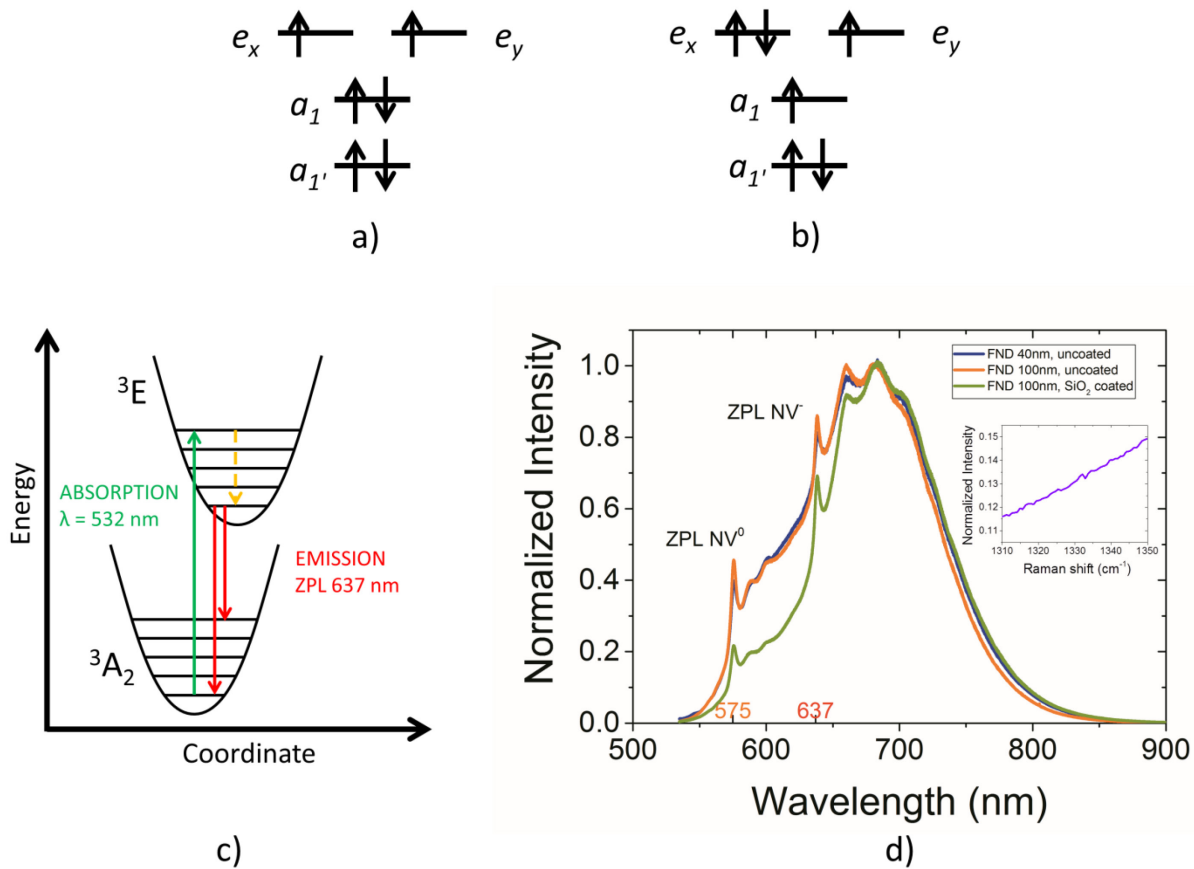


Figure 5.2 – Two possible wave functions of the ground and excited states are sketched in panels a and b, respectively. Panel c shows the ground and excited electronic states with vibronic structure. Collected PL is displayed in panel d, taken with a 532 nm laser excitation, for the 40 nm uncoated (blue line), 100 nm uncoated (orange line) and 100 nm silica-coated (green line) NDs. A striking difference of PL in the NV^0 region can be ascribed to the silica coating, which seems to favor the amount of NV^- compared to NV^0 . PL is so strong that it completely overtakes the Raman peak of diamond at 1332 cm^{-1} (inset of panel d).

On the other hand, our spectra of Figure 5.2d show that at wavelengths longer than 680 nm the three spectra coincide, but around 575 nm the NV^0 emission of the silica-coated NDs (green curve) is lower than the other two. From the ZPLs ratio I_{NV^-}/I_{NV^0} and the S factors one can express the ratio between the concentrations of NV^- and NV^0 , with a procedure analogous to the one of Acosta et al.⁴⁷. With the concentrations normalized according to $[NV^-] + [NV^0] = 1$, we find $[NV^-] = 0.79$ for the silica-coated NDs, and lower values of 0.59 and 0.60 for the 40 nm and 100 nm uncoated NDs, respectively. Defects, especially on the surface, can increase the concentration NV^0 with respect to NV^- and a proper surface termination is often required¹⁸¹⁻¹⁸³. Comparison of the spectra suggests that surface termination or coating are more important than size in determining the ratio I_{NV^-}/I_{NV^0} , at least for NDs of tens of nm. The intensity of the laser could also affect the ratio, through the mechanism of photoionization⁶⁸. This effect will be examined in more detail in the next chapter. Finally, we notice that the Raman peak of diamond is totally exceeded by the strong luminescence and no signal is detected (inset of panel d).

5.2 The spin Hamiltonian

The crystalline field sets the basis for the description of the ground and the excited states and the corresponding degeneracy of levels. Additional interactions that consider explicitly spin lift these degeneracies and make the system a suitable tool for detecting magnetic, electric and strain fields, just through a thorough measurement of luminescence. Here we just give a short list of the interactions that play a prominent role, since the full derivation is beyond the scope of this work and we refer to other works for more information⁶⁵. The form of the Hamiltonians terms can be separate in an axial component along the symmetry axis (let's be oriented along the direction \hat{z})

and a transverse component on the perpendicular plane, reflecting the symmetry of the C_{3v} group. A summary of the coupling constants is given in Table 5.4. The Hamiltonian of the ground state is:

$$\mathcal{H} = \mathcal{H}_{SS} + \mathcal{H}_{SO} + \mathcal{H}_Z + \mathcal{H}_{HF} \quad (5.3)$$

where \mathcal{H}_{SS} is the spin-spin interaction term, \mathcal{H}_{SO} the spin-orbit, \mathcal{H}_Z accounts for the Zeeman interaction of the electron spin with a magnetic field and \mathcal{H}_{HF} is the nuclear hyperfine term. All the values are normalized by the Planck constant h , so the Hamiltonian is expressed in frequency units. More in detail

$$\mathcal{H}_{SS} = D_{gs} \left(S_z^2 - \frac{\mathbf{S}^2}{3} \right) + E(S_y^2 - S_x^2) \quad (5.4)$$

The longitudinal zero-field splitting (ZFS) D_{gs} arises from spin-spin interaction and removes the degeneracy between the $m_s = 0$ and the $m_s = \pm 1$ spin levels of the ground state. It depends on temperature, because the thermal expansion affects the average distance between the electrons in the center¹⁸⁴, with a value at room temperature of ≈ 2.87 GHz. The transverse component of spin-spin interaction E measures the strain and it is therefore sample-dependent, with typical values of few MHz.

The spin-orbit Hamiltonian

$$\mathcal{H}_{SO} = \lambda_z L_z S_z + \lambda_{\perp} (L_x S_x + L_y S_y) \quad (5.5)$$

has a negligible second-order effect on the ground state and a first order on the excited state¹⁸⁵. Additionally, λ_z links states with $m_s = 0$ in the same electron configuration, while λ_{\perp} links states with $m_s = \pm 1$ to singlets in different electronic configuration. This can be visualized more clearly if the transverse part is written in terms of ladder operators, $\lambda_{\perp} (L_+ S_- + L_- S_+)$.

When an external magnetic field is applied, the energy levels are shifted according to the Zeeman interaction, valid for *strong* magnetic fields. The Hamiltonian term is

$$\mathcal{H}_Z = \frac{g_s \mu_B}{h} \mathbf{B} \cdot \mathbf{S} \quad (5.6)$$

where $g_s \approx 2,003$ is the Landé g-factor of the electron⁶⁵, with small differences between axial and transverse components¹⁸⁶, and μ_B the Bohr magneton. Since the spin is oriented along the z-axis, only B_z contributes to the splitting. Clearly, NV centers with different orientations feel different effective magnetic fields.

Coupling coefficient	Symbol	Value	Reference
Axial ZFS	D_{gs}	2.87 GHz	Chen et al. ¹⁸⁴
Axial SO ^a	λ_z	5.5 MHz	Maze et al. ³²
Transverse SO ^a	λ_{\perp}	7.3 MHz	Maze et al. ³²
Landé g-factor	g_s	2.003	Felton et al. ¹⁸⁶

Table 5.4 – Coupling constants used in the spin-spin, spin-orbit and Zeeman interactions. ^a the SO parameters refer to the excited state.

The nuclear hyperfine term depends on the type of nucleus:

$$\mathcal{H}_{HF} = P_{gs} \left(I_z^2 - \frac{\mathbf{I}^2}{3} \right) + A_z S_z I_z + A_{\perp} (S_x I_x + S_y I_y) \quad (5.7)$$

The first is a quadrupolar term that is non zero for ¹⁴N and vanishes for ¹⁵N and ¹³C. The isotopic composition of nitrogen is 99.6% of ¹⁴N and 0.4% of ¹⁵N, while ¹³C constitutes 1.1% of the total carbon atoms. The second term gives the hyperfine coupling with axial (A_z) and transverse (A_{\perp}) constants. The

nitrogen under consideration is the one of NV center itself. On the contrary, the carbon can be found in the first neighbor position (one of the three atoms around the vacancy) or farther, with different interaction strengths¹⁸⁶⁻¹⁸⁸. Table 5.5 lists the coupling constants for the hyperfine interaction. In the Hamiltonian we have neglected additional interactions whose magnitude is usually lower, or which are not used in the common schemes of ODMR, as Zeeman splitting of the nuclear spin levels and electric field-dipole interaction. Figure 5.3a shows the spin-spin, Zeeman and ¹⁴N hyperfine interaction on the ground state sublevels.

Coupling coefficient	Symbol	Value (MHz)
Quadrupole parameter ¹⁴ N	P_{gs}	-5.01
Axial hyperfine ¹⁴ N	A_z	-2.14
Transverse hyperfine ¹⁴ N	A_{\perp}	-2.70
Quadrupole parameter ¹⁵ N	P_{gs}	-
Axial hyperfine ¹⁵ N	A_z	3.03
Transverse hyperfine ¹⁵ N	A_{\perp}	3.65
Quadrupole parameter ¹³ C	P_{gs}	-
Axial hyperfine ¹³ C ^a	A_z	199.7
Transverse hyperfine ¹³ C ^a	A_{\perp}	120.3

Table 5.5 – Coupling coefficients in the hyperfine potentials with nuclei of ¹⁴N, ¹⁵N and ¹³C. Values are taken from Felton et al.¹⁸⁶. ^a Values referred to first neighbor atoms.

As anticipated, spin-orbit mixes levels with different spin projections and different orbital wave functions. The outcome of this mechanism can be seen in the ODMR spectra. When the NV center is optically excited, the system goes from a spin level of the ground state to a level of the excited state with the same spin projection, because of selection rules of the electric-dipole

transitions. In the excited state, the system can decay radiatively to the ground state with the emission of a photon (again a spin-preserving transition) or it can decay non-radiatively to an intermediate singlet through the SO interaction. The rate constants for the non-radiative decay are zero for $m_s = 0$ and $30 \cdot 10^6 \text{ s}^{-1}$ for $m_s = \pm 1$ (Figure 5.3b), resulting in a weaker luminescence from the $m_s = \pm 1$ of the excited state. This non-radiative pathway is known as intersystem crossing (ISC). As a consequence, upon laser pumping ISC depletes the population of the $m_s = \pm 1$ levels of the ground state and increases the population of $m_s = 0$, which becomes optically polarized. The $m_s = \pm 1$ levels can be again populated by a resonant microwave radiation (matching the zero field splitting of 2.87 GHz plus or minus the Zeeman and/or hyperfine energies), resulting once more in a reduced fluorescence emission. This microwave-dependent drop in luminescence is shown in Figure 5.3c. The ODMR spectrum was taken from the collected emission of 100 nm uncoated NDs over a large area of $\sim 330 \times 330 \mu\text{m}^2$ (panel d), with a modified Nikon Ti-E inverted wide field microscope. The two shallow side resonances are due to the ^{13}C hyperfine interaction. In this particular sample the ZFS components are $D = 2871 \text{ MHz}$ and $E = 5 \text{ MHz}$. Finally, panel e shows the scheme adopted for ODMR.

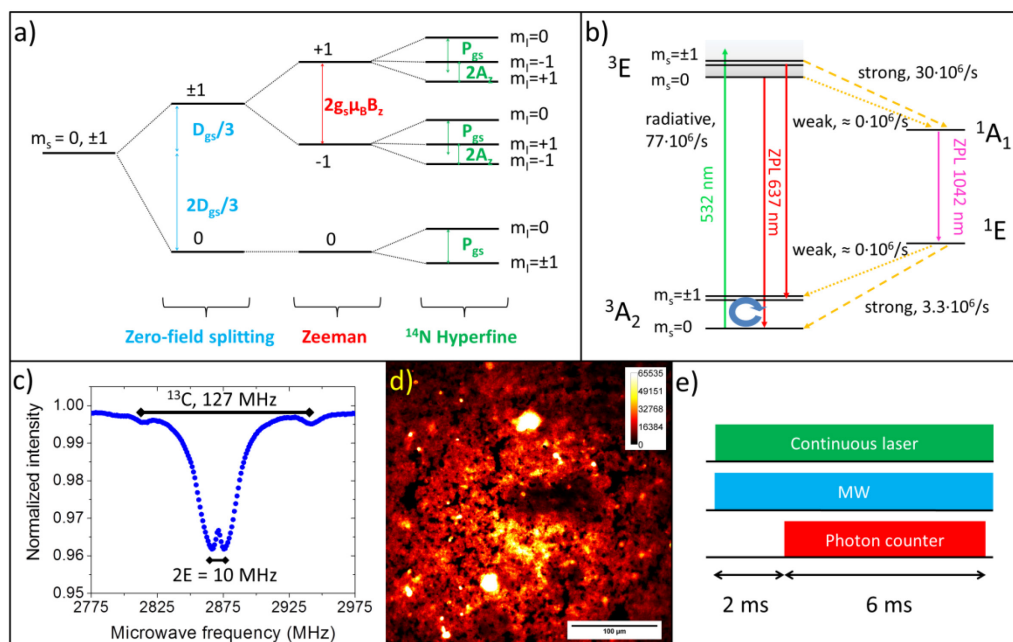


Figure 5.3 – Ground state sublevels are depicted in panel a, with coupling coefficients due to ZFS, Zeeman and ^{14}N hyperfine interactions. b: excitation (green line) can be followed by optical relaxation (red line) or a non-radiative decay, called intersystem crossing (ISC), through singlet dark states. The ISC is selective in the spin projection and luminescence can be modulated by the application of an external microwave field (panel c, over sample in panel d). e: the sequence adopted in continuous wave ODMR (CW ODMR).

5.3 Experimental set up

The experimental set up is sketched in Figure 5.4. It is composed by two independent parts, the first containing the laser excitation and the detection (enclosed by the grey dashed box) and the second containing the microwave circuits and the possibility to apply a magnetic field (in the pink dashed box). For the optical excitation, we used two 532 nm lasers: either a high-power Verdi G5 of Coherent or a low-power GEM of Laser Quantum. The two laser beams were polarized with a linear polarizer and the intensity

optionally reduced with neutral density filters. Two acousto optic modulators, either the ISOMET M1133-Aq110-2 or the AA Opto Electronic MT200-A0,5-VIS were used to pulse the high and low power lasers, respectively. Laser pulses were focused with a 40X Olympus Plan Achromat Objective (0.65 NA, 0.6 mm WD) onto the sample. Luminescence was collected with the same objective and coupled into a fiber before detection with a photon counter (Excelitas SPCM-AQRH-14-FC). A combination of a shortpass and a highpass filters was adopted to limit the detection bandwidth to the interval 620 – 750 nm.

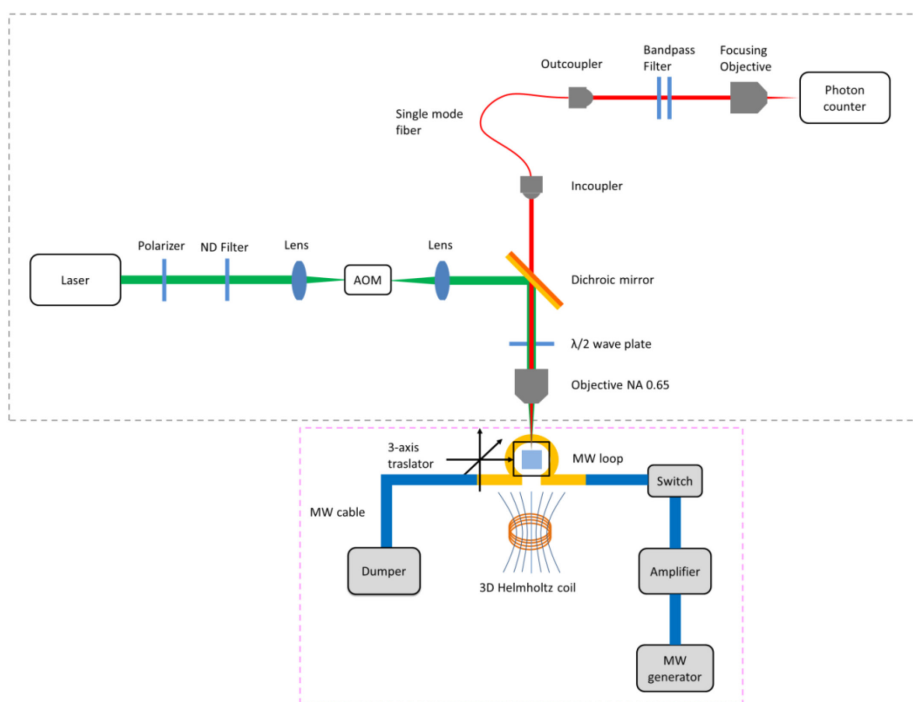


Figure 5.4 – The experimental set up is composed by a part containing the optical line (enclosed by the grey box) and another for the microwave line (pink box). The diamond sits on a loop, with the possibility of 3D motion and application of a magnetic field.

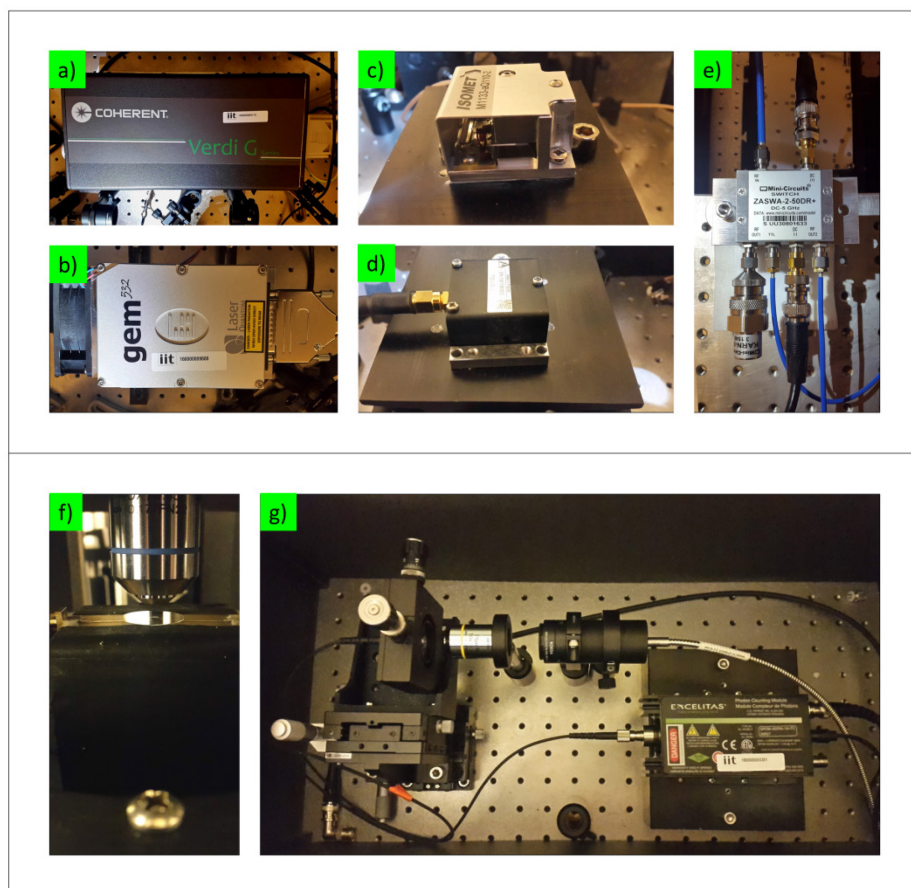


Figure 5.5 – Pictures of the devices used to perform the experimental part. Either a high power Verdi (a) or a GEM (b) green lasers were focused through acousto-optic modulators (c, d) to obtain pulsed excitations. mw pulses were also controlled with a switch (e). The diamond sample sat on a loop for mw excitation, under a microscope objective (f). The luminescence were collected by the same objective and brought to a photon counter, enclosed in a box (g)

Microwaves were generated by a Keysight N5171B generator, then amplified and selectively pulsed with a mw switch (Mini-Circuits, ZASWA-2-50DR+). The sample was lying on a custom-made Au-coated copper loop, connected to the mw line, to make the mw field uniform at the sample position. Optionally the 3-axis Helmholtz coil 100G HHC of MicroMagnetics

could provide a magnetic field up to 100 G along each axis and a 3-axis translator was able to move the position of the focal spot on the sample.

The AOM, mw generator, mw switch and photon counter were remotely controlled via TTL pulses by PBESR-PRO-300 pulse generator by SpinCore Technologies and data were collected by a data acquisition card (PCIe-6323 of National Instruments). The main devices are shown in Figure 5.5.

5.4 Characterization of the NDs through optical analyses

We characterized our NDs to understand the capabilities as a probing system in different environments. First we checked the pump power dependence on the photoluminescence. It is known that, under continuous pumping, the photoluminescence reaches a steady value that is determined by the various decay rates between the ground and excited states, which we indicate collectively as k . Then, the number of photon detected per unit time is

$$R(I) = R_{\infty}(k, \varphi) \frac{I}{I + I_s} \quad (5.8)$$

where I_s is the saturation intensity and R_{∞} the maximum emission rates which depends also on the photon detection efficiency φ . In Figure 5.6 the experimental data are fitted with the hyperbole of Eq. 5.8 with parameters $I_s = 23.8 \text{ mW}$ and $R_{\infty} = 28.0 \cdot 10^6 \text{ counts s}^{-1}$. The collected emission was reduced by a 3.8 optical density (OD) filter, meaning a reduction of a factor ~ 6300 in the number of photons.

In Figure 5.7a and 5.7b the ODMR spectra of 100 nm SiO₂-coated NDs are plotted as a function of the laser pump power and microwave power, respectively. The contrast decreases with the pump power (panel c), a phenomenon that could be related to photoionization of the NV⁻. However, the signal to noise ratio (snr) increases with laser power, so the proper conditions of laser pumping are a tradeoff between contrast and snr. On the other side, with high mw power contrast is high, but there is also a broadening of the resonance dips (panel d). Again, a tradeoff between contrast and resolution in frequency is required. By extrapolating the FWHM at zero mw power, it is possible to give a raw estimate of the dephasing time T_2^* , which will be explained in details in the next chapter. For the SiO₂-coated NDs we found $T_2^* = 68$ ns, a value that is in good agreement with the dephasing time obtained with more sophisticated procedures of Ramsey interferometry.

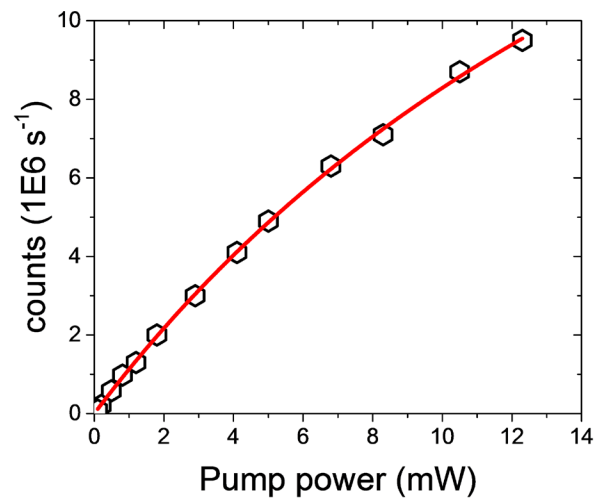


Figure 5.6 – Luminescence, expressed in counts s⁻¹, as a function of laser intensity. The power of the laser was taken far from the saturation level to minimize the effect of photoionization of the NV⁻ centers.

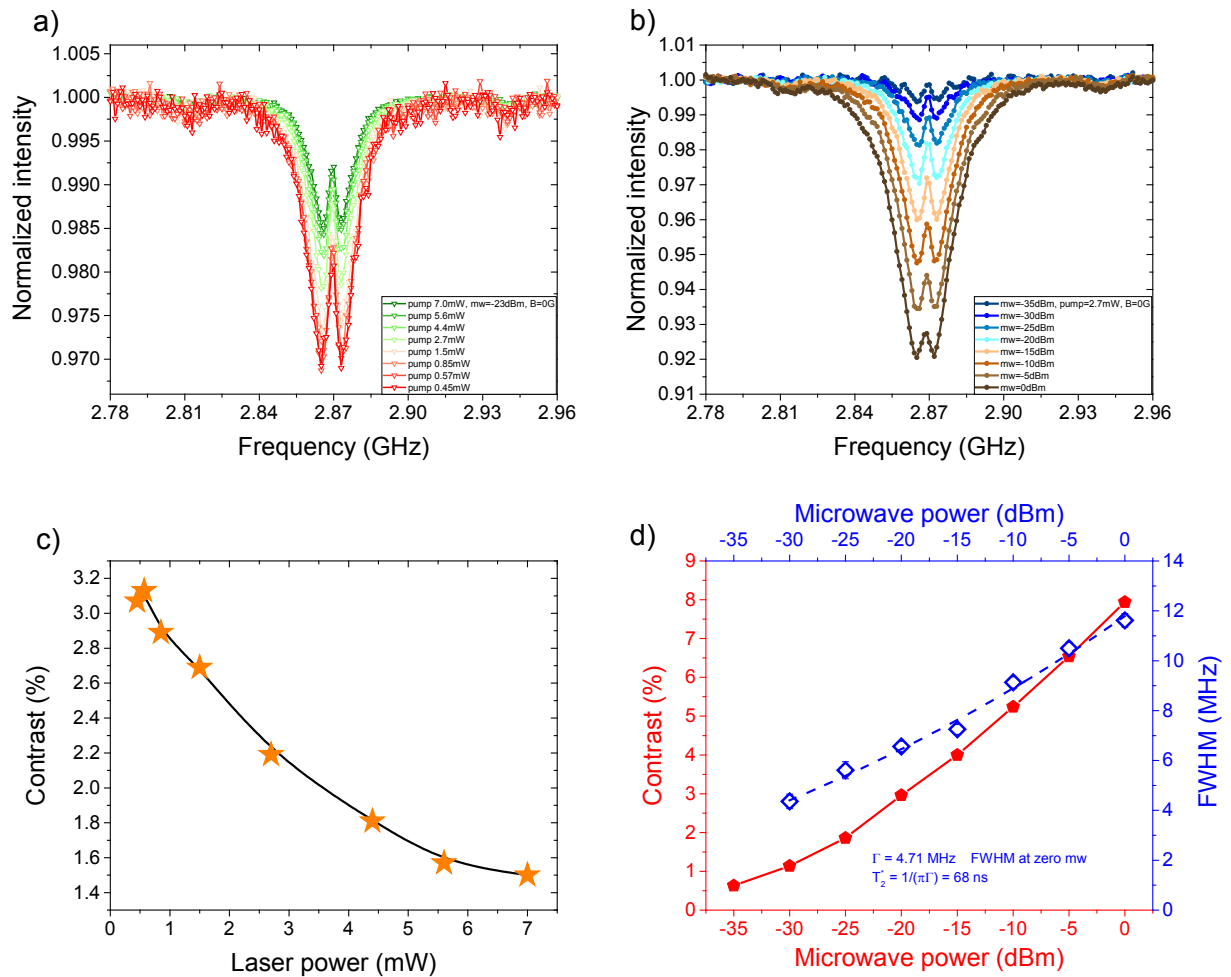


Figure 5.7 – ODMR contrast as a function of laser power (a, c) and mw power (b, d). The contrast decreases with increasing laser power, probably related to the phenomenon of photoionization, and increases with mw power. From the FWHM it is possible to estimate the dephasing time T_2^* (panel d).

The FWHM has been estimated for the three types of NDs under the same conditions of laser intensity irradiation (3.3 mW) and mw power (−23 dBm at generator). The ODMR spectra were modified for a better comparison:

naming $I(\nu)$ the intensity as a function of frequency, I_{off} the off-resonance value of I , far from the dips, and I_{min} the minimum value of I at the dips, in Figure 5.8 we plotted the normalized intensity

$$\frac{I_{off} - I(\nu)}{I_{off} - I_{min}} \quad (5.9)$$

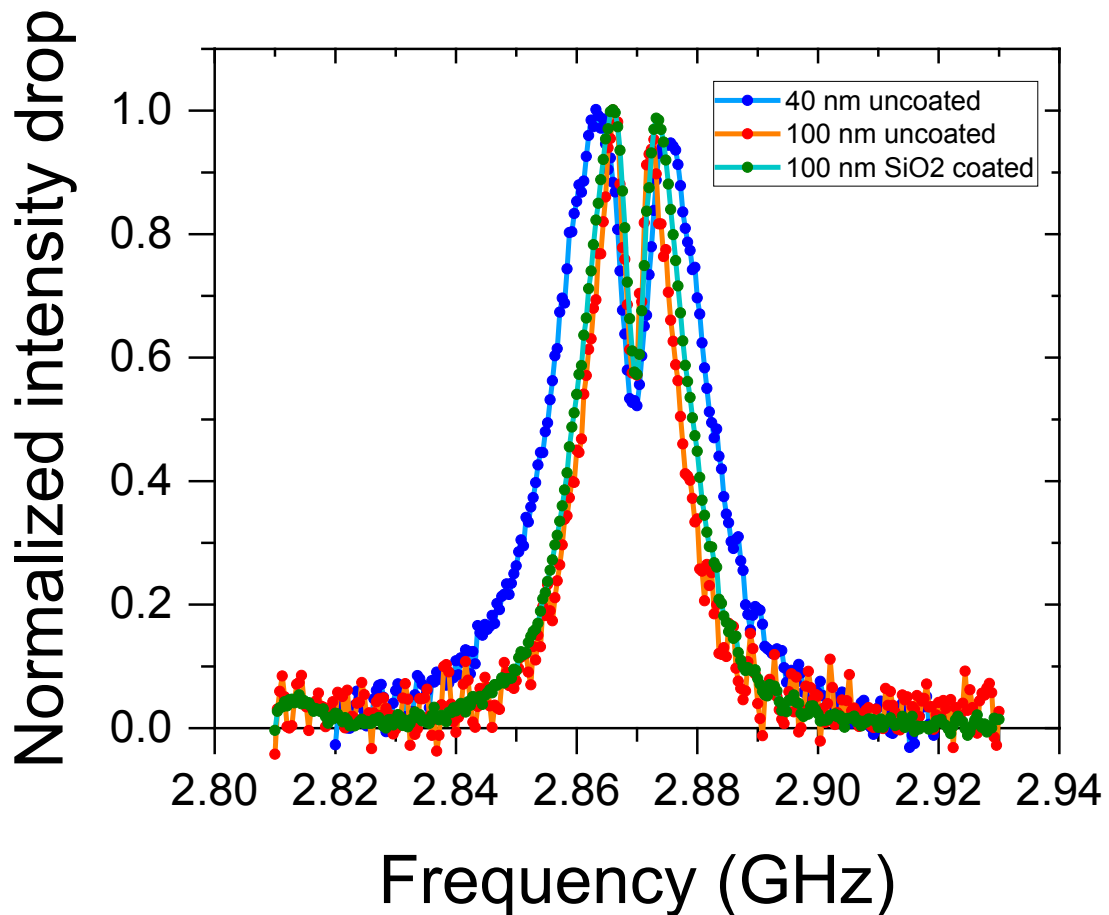


Figure 5.8 – ODMR normalized in order to emphasize the broadening due to size. The 40 nm uncoated NDs have a larger FWHM, resulting in a shorter dephasing time.

From the analyses, it seems that the coating is not affecting substantially the broadening of the ODMR and the 100 nm NDs. Both the uncoated (red curve/points) and the silica-coated (green curve/points) have almost the same FWHM in those conditions, around 6.4 MHz. On the contrary, the 40 nm uncoated have a broader FWHM, around 9.4 MHz. This reflects on the length of the dephasing time T_2^* , that will be examined in the next paragraph, through the relation^{47,189} $T_2^* = 1/(\pi\gamma_{inh})$, where γ_{inh} is the inhomogeneous broadening, obtained by extrapolating the FWHM at zero mw field. The estimated value of $T_2^* \approx 70$ ns for the 100 nm uncoated and 100 nm silica-coated NDs reduces to almost 50 ns in the case of 40 nm uncoated NDs. This suggests that in a minor volume the NV centers are more sensitive to radicals on the surface¹⁹⁰ and, possibly, that a smaller volume implies higher surface-induced strain acting on the centers and a more defective structure of the lattice^{191,192}. Irrespective of this difference, T_2^* is short in all the three samples when measured in connection with ensemble of NV centers in a large single crystal.

In most of the experiments we kept a low sub-threshold pumping intensity (2 – 10 mW) to avoid the phenomenon of photoionization as much as possible and to increase the contrast, while, on the other side, ensuring a sufficient initialization of the $m_s = 0$ spin ground state. At the same time, the microwave (MW) power was kept at –23 dBm before amplification (corresponding to almost 8 mW at the NDs sample holder) to limit the line broadening.

As a first application, we wanted to check the capabilities of NV-enriched NDs in the sensing of magnetic fields in the range ≤ 50 G. The application of a magnetic field results in the Zeeman splitting of the $m_s = \pm 1$ spin levels. If the laser focal spot contains a large number of NDs with random orientations,

the magnetic field projects on the differently oriented NV centers with a certain probability, giving a distribution of splitted energies. For low magnetic fields, the splitting in frequencies is symmetric⁴⁸:

$$\nu_{\pm} = D \pm \sqrt{\nu_0^2 \cos^2 \vartheta + E^2} \quad (5.10)$$

with

$$\nu_0 = \frac{g_s \mu_B B}{h} \quad (5.11)$$

and ϑ is the angle between the magnetic field and a center. The collected ODMR signal is the convolution between the single resonance lineshape and the probability to have a certain orientation between the magnetic field and an NV axis, considering also the transition probability among different spin levels¹⁹³. Since ν_{\pm} do not depend on the azimuthal angle φ and are quadratic in $\cos \vartheta$, this probability is just $\sin \vartheta$, or, for the $m_s = +1$ level

$$p(\nu) = \sqrt{1 + \frac{E^2 - (\nu - D)^2}{\nu_0^2}} \quad (5.12)$$

between the unperturbed value $\nu_{\vartheta=\pi/2} = D + E$, and $\nu_{max} = D + \sqrt{\nu_0^2 + E^2}$, and zero outside. For the $m_s = -1$ level the probability is reversed between $\nu_{min} = D - \sqrt{\nu_0^2 + E^2}$ and $\nu_{\vartheta=\pi/2} = D - E$. The resonance lineshape is approximately a Lorentzian peaked around a center frequency ν_c

$$L(\nu) = A - \frac{AV\Gamma^2}{4(\nu - \nu_c)^2 + \Gamma^2} \quad (5.13)$$

where A is the offset, V the contrast and Γ the full width at half maximum (FWHM). The convolution

$$p(\nu) * L(\nu) \quad (5.14)$$

is plotted in Figure 5.9 for two values of magnetic field. At the low value of 10 G, the fit reproduces correctly the ODMR shape. At 50 G the fit is able to reproduce amplitude and width, but it is centered at lower frequencies. This can be explained by the fact that at high magnetic fields the Zeeman splitting of the $m_s = \pm 1$ levels is not symmetric, but it is dragged at higher frequencies and depends strongly on the mutual orientation between B and the NV axis^{48,194}. The experimental spectrum therefore is centered around 2878 MHz, some 7 MHz more than the computed convolution. Finally, we estimated a single layer of NDs deposited on the glass substrate, with few tens of NDs in the focal spot of the laser. Increasing the magnetic field, there are fewer NV centers contributing to a particular frequency, resulting in the broadening of the ODMR with a drop in the contrast. Our results are consistent with those of a recent paper¹⁹³ in which the ODMR coming from an ensemble of randomly oriented NDs is investigated in details.

The results reported indicate that in principle it is possible to measure the amplitude of magnetic fields of several G even with clusters of randomly oriented NDs, by looking at the broadening and at the shift of the central “peak” in the ODMR spectra.

5.5 Spin dynamics

In this paragraph we focus on the spin dynamics of NV centers and on ways of manipulating the population in the ground state sublevels by applying sequences of laser and mw pulses. The surroundings can interact with the NV centers and lead to a loss of population in suitably prepared states, or to a depolarization of the optically polarized $|0\rangle$ ground state. Three parameters describe the timescales at which those interactions strongly influence the NV spin dynamics: the dephasing time T_2^* , the decoherence time T_2 and the spin-

lattice relaxation time T_1 . They are introduced one by one in the following discussion.

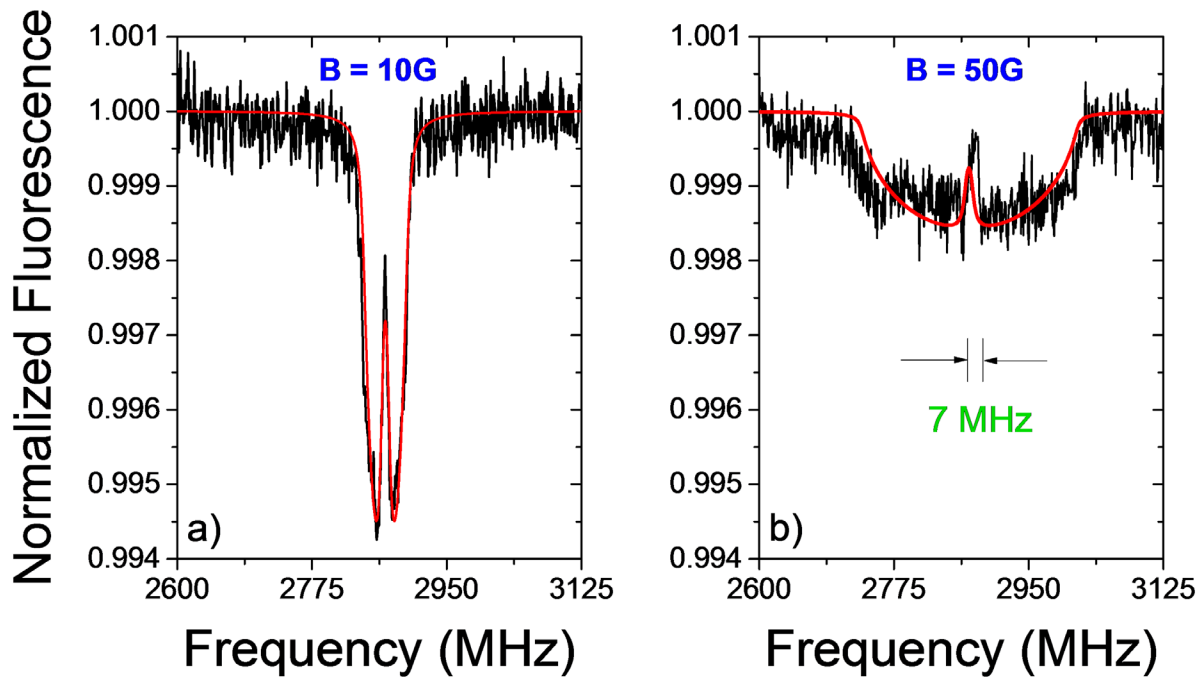


Figure 5.9 – ODMR of NV-enriched NDs ensembles, at the two magnetic fields of 10 G (a) and 50 G (b). The ODMR are a superposition of single Lorentzian lineshapes at different frequency shifts. With 50 G of magnetic field the center of this convolution is moved at higher frequencies.

Within the ground state of the NV center the $m_s = \pm 1$ levels are splitted by the transverse ZFS $2E$ in addition to the splitting induced by an external magnetic field. Each couple of states $|0\rangle, |+1\rangle$ and $|0\rangle, |-1\rangle$ constitutes a two levels system analogous to a spin state $S = \frac{1}{2}$ that can be described by a general Hamiltonian of the form

$$\hat{H} = \frac{1}{2} \begin{pmatrix} E_0 + W_z & W_x - iW_y \\ W_x + iW_y & E_0 - W_z \end{pmatrix} = \frac{1}{2} E_0 + \frac{1}{2} \mathbf{W} \cdot \boldsymbol{\sigma} \quad (5.15)$$

where $\mathbf{W} = (W_x, W_y, W_z)$ and $\boldsymbol{\sigma} = (\sigma_x, \sigma_y, \sigma_z)$ and $\sigma_{x,y,z}$ are the Pauli matrices. The evolution of a state $|\Psi(t)\rangle = \alpha(t)|0\rangle + \beta(t)|-1\rangle$ can be readily visualized on the Bloch sphere, where the north pole is chosen to be the state $|0\rangle$ and the south pole the state $|-1\rangle$ (Figure 5.10). Then

$$|\Psi_0\rangle = \cos \frac{\vartheta}{2} |0\rangle + e^{i\varphi} \sin \frac{\vartheta}{2} |-1\rangle \quad (5.16)$$

with ϑ the polar angle and φ the azimuthal angle with respect to the x -axis. The application of an external microwave field with a frequency ω resonant or slightly detuned with the separation ω_0 and orthogonal to the z -axis results in a Hamiltonian of the form

$$\hat{H} = \frac{\hbar}{2} \begin{pmatrix} -\omega_0 & \omega_d e^{i\omega t} \\ \omega_d e^{-i\omega t} & \omega_0 \end{pmatrix} \quad (5.17)$$

and $\hbar\omega_d$ gives the amplitude of the driving microwave field. As a result, the population in the state $|0\rangle$ oscillates periodically between a maximum and minimum value, with a probability to find the state in $|-1\rangle$ given by

$$P_{-1}(t) = |\langle -1 | \Psi(t) \rangle|^2 = \frac{1}{2} \frac{\omega_d^2}{\Delta^2 + \omega_d^2} \left[1 - \cos \left(t \sqrt{\Delta^2 + \omega_d^2} \right) \right] \quad (5.18)$$

where $\Delta = \omega - \omega_0$ is the detuning. At resonance $\Delta = 0$ and is possible to invert completely the population from $|0\rangle$ to $|-1\rangle$, by applying a π pulse of length $t_\pi = \frac{\pi}{\omega_d}$. A $\pi/2$ pulse of length $\frac{\pi}{2\omega_d}$ creates a superposition $\frac{1}{\sqrt{2}}(|0\rangle + e^{i\varphi}|-1\rangle)$ that is aligned along the \hat{x} -axis for $\varphi = 0$ and along the \hat{y} -axis for $\varphi = \pi/2$. In the rotating frame approximation the \hat{x} - and \hat{y} -axes precede around \hat{z} with frequency ω , so the magnetic field is constant, let us say along \hat{x} , and the $|\Psi(t)\rangle$ rotates in the yz plane.

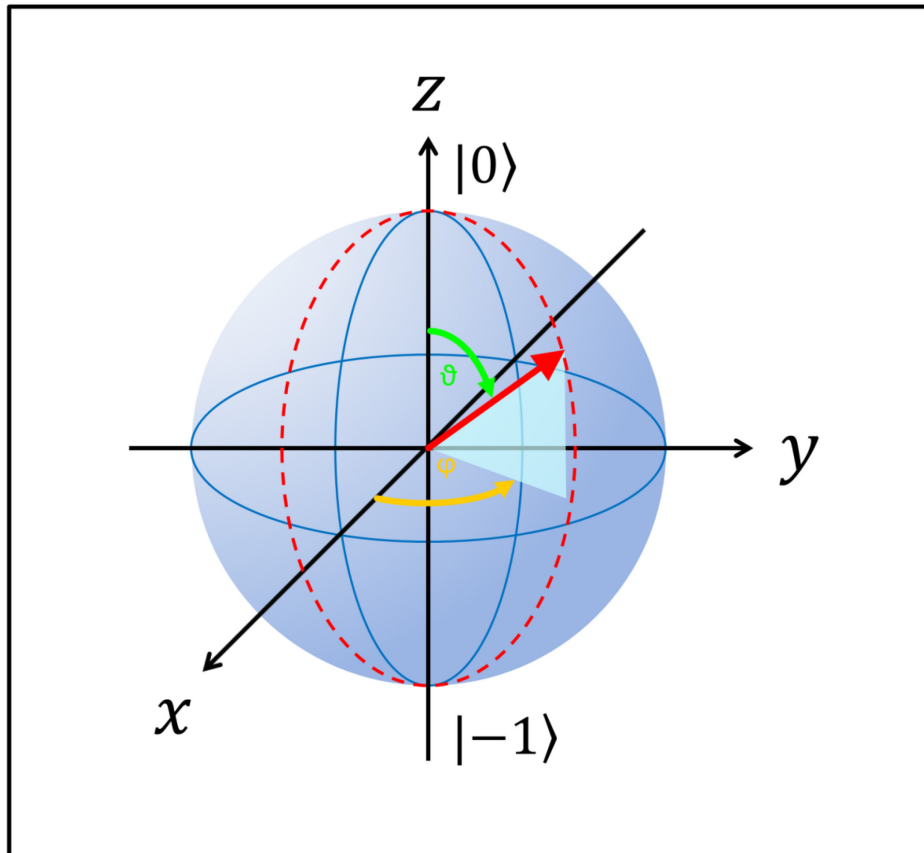


Figure 5.10 – Bloch sphere representation of a two-level spin system. The couple of spin states $|0\rangle$ and $|-1\rangle$ occupy the north and south poles of the Bloch sphere, respectively, and every other point on the sphere (red arrow) is a superposition of these two states and can be represented by a couple of polar and azimuthal angles (ϑ and ϕ).

Since the population of the two states $|0\rangle$ and $|-1\rangle$ is proportional to the collected luminescence, it can be addressed optically through a combined sequence of laser and MW pulses (Figure pulse sequence 5.11c). A 3D plot of

Rabi nutation curves taken on NV ensembles as a function of time and MW power is shown in Figure 5.11a. The spin is coupled with the environment^{44,64,195} and quickly loses coherence. When many electrons are initialized in the $|0\rangle$ state the system is polarized. However, the local environment is different for each NV center and the time evolution of the spin is affected by external perturbation. Paramagnetic defects as ^{13}C nuclear spins and the electronic magnetic moments of substitutional nitrogen, for instance, give rise to a local additional magnetic field acting on the NV spins, with a coupling strength that depend mostly on the amount of these inhomogeneities and their spatial distribution^{45,196}. Then, the local environment leads to a dephasing of the initial equally polarized spins with a characteristic time known as the dephasing time T_2^* , ranging from 100 ns in HPTH diamonds to 100 μs in ^{12}C isotopically pure CVD. The NV spins can be partially decoupled from the environment by employing the Hahn-Echo or multiple-echo pulse sequences, thanks to which the effect of slow varying fields cancels out. As a result, coherence might be increased to timescales much longer than T_2^* , of the order of the decoherence time T_2 (up to 1 s in isotopically pure diamonds at low temperatures¹⁹⁷). The decay times T_2^* and T_2 allow to investigation of the local environment in diamond lattice^{44,195}.

A rough overestimate of T_2^* comes from the exponential envelope of the Rabi oscillations, fitted in our case by the single exponential decay function

$$I(t) = I_0 + Ae^{-t/T_{\text{Rabi}}} \cos(\omega(t - t_0)) \quad (5.19)$$

The decay time T_{Rabi} is determined by a complicated interplay between the strength of the driving field ω , the coupling between the NV centers and a bath of spins, and the intrabath dynamics^{63,64}. Values of ≈ 200 ns have been obtained by fitting the envelope, so T_{Rabi} is significantly larger (3 – 4 times) than T_2^* calculated from the FWHM of the ODMR curves. In our case the detected luminescence is an overlap of signals coming from an

inhomogeneous ensemble of spins and the Rabi oscillations decay fast, compared to the case of single NV (Figure 5.11a). As a consequence, oscillations are detected only at strong driving fields or, equivalently, at high microwave powers, more than few Watts. The Rabi frequency obeys the usual linear relation with the magnetic field B or with the square root of the microwave power¹⁹⁸ (Figure 5.11b). Let's remark that, when analyzing organic matter, elevate microwave intensities are extremely harmful and must be avoided, posing a limitation in the use of these pulse sequences.

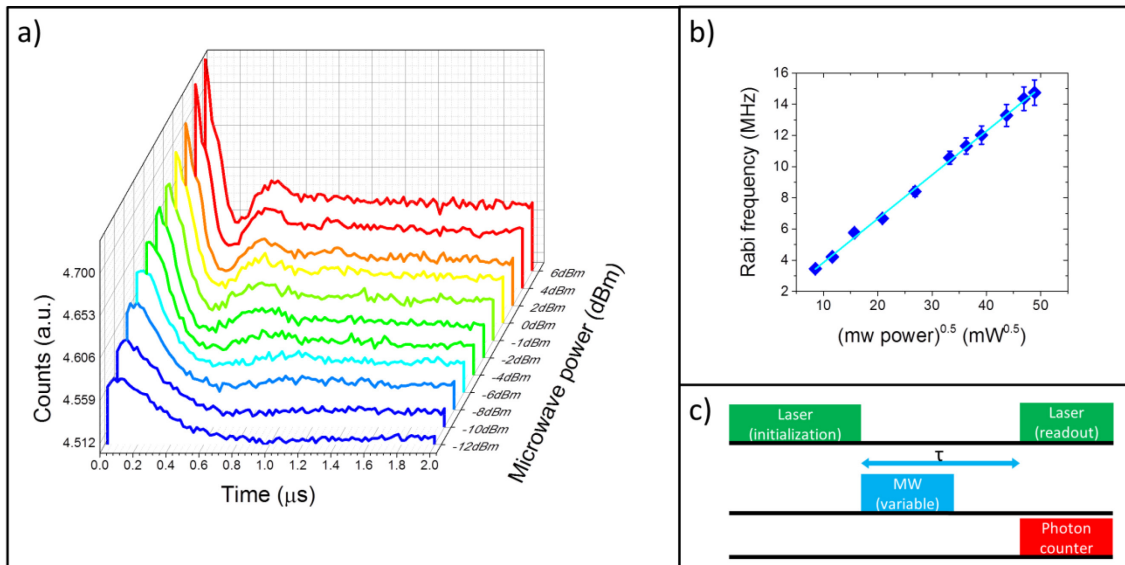


Figure 5.11 – Rabi nutations at different mw power (a), taken with the sequence pulse shown in panel c. The signals come from an inhomogeneous ensemble of NV spins and overlap to give a fast decaying curve. The Rabi frequency is plotted as a function of square root of the mw power, displaying a linear trend (b).

The decay envelope of Ramsey interferometry gives a more accurate evaluation of T_2^* (Figure 5.12b). The Bloch sphere of Figure 5.12a summarizes visually the time evolution of the NV spins: the spin ensemble is initially polarized in the $|0\rangle$ state and then flipped onto the equator state $\frac{1}{\sqrt{2}}(|0\rangle + e^{i\varphi}|-1\rangle)$ with a $\pi/2$ pulse. After that, spins precess during the free induction decay time t with a frequency dependence on the local strength of magnetic field, with faster (pink) and slower (yellow) components, resulting in a net loss of common phase. A second $\pi/2$ pulse orients the spin to the "south pole", the spin state $|-1\rangle$, ready for optical readout (Figure 5.12c). It should be noticed that the dephasing time is comparable with the value extrapolated from the ODMR FWHM at different MW powers (Figure 5.5d) and both are shorter than the Rabi decay time by a factor of ~ 3 .

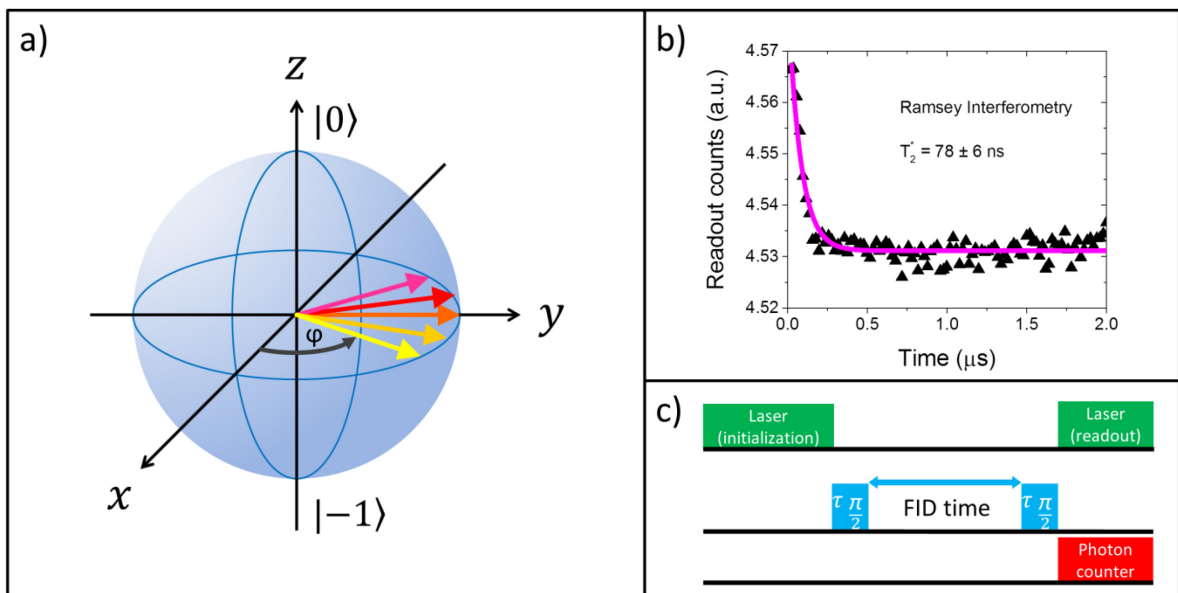


Figure 5.12 – a: Bloch sphere representation of free induction decay pulse sequence (shown in panel c). The decay represents a loss in coherence of initially polarized spins, due to external perturbation. Panel b shows the decay as a function of time. From the envelope it is possible to extract a dephasing time T_2^ of ≈ 78 ns.*

The perturbation of the environment is not limited to dephasing. The NV spin can effect a “longitudinal” transition from the “north pole” to the “south pole” of the Bloch sphere, i.e. from $|0\rangle$ to $|-1\rangle$. The time characterizing this transition is the spin-lattice relaxation time T_1 . Phonons are responsible of the variability of T_1 with temperature^{199,200}. A shortening of T_1 may come from nuclear spins, paramagnetic defects, perturbation from external magnetic fields^{200,201} and even from high density of NV centers through the mechanism of flip-flop cross-relaxations. However, under normal conditions the inequality $T_2^* < T_2 < T_1$ holds, and T_1 can be several orders of magnitude longer than T_2^* , even with a high level of defects in the diamond. Long dynamics is appreciable when investigating the properties of the environment and T_1 has been adopted more and more often as a robust tool to investigate the magnetic properties around the center. In addition to that, T_1 relaxometry needs only optical initialization, without any further manipulation with microwaves. Therefore, both longer dynamics and absence of microwave fields are valuable properties of T_1 relaxometry when implemented to biological sample.

In Figure 5.13 we show a comparison between the T_1 of the three different types of NDs. The data were acquired under the same experimental conditions of laser power intensity and time of initialization. We observed an irregular deposit of NDs on the glass and different subregions in the deposit display variable levels of luminescence. For this reason, the initialization of the NV centers might be slightly different in the three types of NDs (compare also Figure 5.6), depending on the amount of NDs. The small difference in the offset of T_1 at longer times can then be ascribed to a tiny difference in the conditions of initialization and to the choice of normalization at the initial point. Apart from that, the uncoated NDs have a comparable T_1 , longer than 0.6 ms, while for the silica coated NDs T_1 is a little shorter (0.47 ms). An additional contribution to the dephasing in the silica coated NDs might come

from the high amount of NV centers (compare Figure 5.2d) and more effective flip-flop interactions inside the ND lattice⁷². As expected, T_1 is much longer than T_2^* , four orders of magnitude (compare results of Figure 5.5, Figure 5.12).

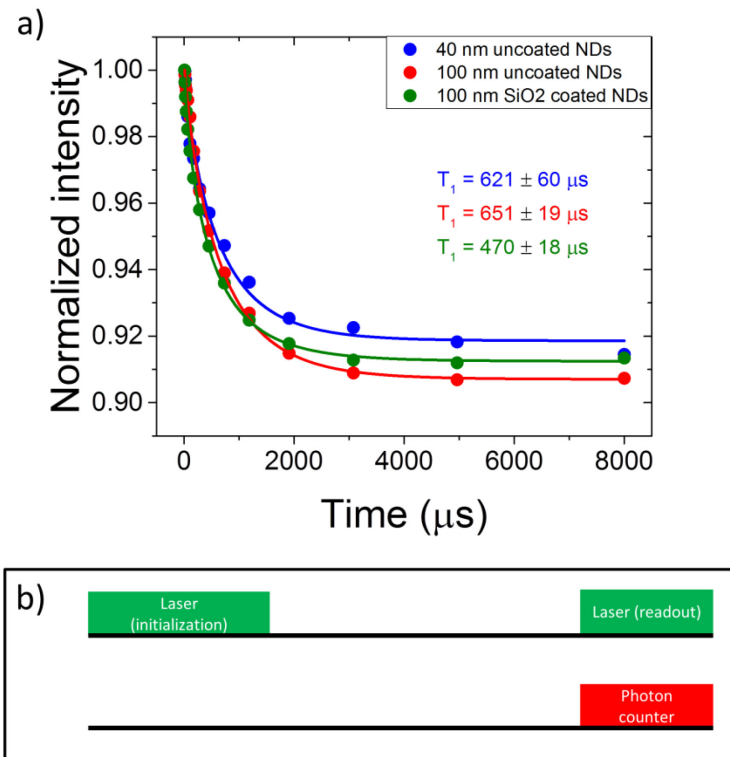


Figure 5.13 – a: spin-lattice relaxometry of our luminescent NDs. T_1 is four orders of magnitude longer than T_2^* and does not require mw fields, which makes it more promising in biosensing. Panel b shows the pulse sequence adopted.

5.6 Conclusions

I conclude this chapter by summarizing the results obtained in the analyses of NDs. The high concentration of NV centers and high density of NDs deposited on the glass slide results in a strong luminescent signal that can be readily detected with our set-up. The ODMR is composed by the superposition of different resonance spectra, with no sign of hyperfine splitting due to ^{14}N , ^{15}N and ^{13}C . The randomness of NV orientation in the focal spot of the laser is demonstrated also by the application of a magnetic field that broadens the ODMR signal. Nevertheless, with a proper convolution, it is possible to measure the magnitude of the magnetic field applied with possible applications in the high-field magnetometry. Detection of low magnetic fields is made difficult by the short dephasing time, of the order of 70 ns for the biggest NDs of 100 nm, regardless of the coating, and 50 ns for the 40 nm NDs. This suggests a more disordered structure for the smallest NDs, a result which seems to be consistent with general observations. On the other side, the spin-lattice relaxation time has proven to be four orders of magnitude longer. Importantly, T_1 can be measured without the need of microwave pulses. These two aspects could make it a suitable tool in biosensing, bioimaging and, in general, in the detection of paramagnetic species in the surroundings of the nanodiamonds. In the analyses of T_1 , we observed a value close to 0.65 ms for the uncoated NDs and around 0.47 ms for the silica coated NDs. This observation is linked with a difference in the photoluminescence spectra of the three NDs samples. In fact, the SiO₂-coated NDs display a low luminescence coming from neutral NV⁰ compared to the uncoated NDs, implying a lower amount of NV⁰ and, in turn, a higher amount of NV⁻. The interaction between different NV⁻ has been proposed as a source of T_1 reduction, compatible with experimental observations. In the next chapter we will use these results to investigate the effect of paramagnetic Gd

and blood on T_1 shortening and find an interesting interplay between charge and spin dynamics.

CONCLUSIONS

Chapter 6

Coupled charge and spin dynamics of T_1 relaxation in the presence of paramagnetic species

We saw in the previous chapter that the dephasing time of NV ensemble in nanodiamonds is extremely short. This means that it is difficult to investigate the magnetic environment with ODMR, Rabi and Ramsey sequences. On the other side, T_1 is much longer, around 0.6 ms, with no big differences with respect to NDs size (100 nm or 40 nm) or induced by a thin silica coating. As we pointed out, T_1 can be measured by optical initialization and readout, without involving microwave pulses, a valuable condition when working with biological samples. To start with, we checked the sensitivity of NDs to external paramagnetic gadolinium, a contrast agent used in nuclear magnetic resonance for its high magnetic moment. It must be noted that the possibility of measuring a single spin, in particular of Gd, by T_1 relaxometry has recently attracted a lot of interest and can open new perspectives in the biomedical field^{66,67,190,202,203}.

This chapter is entirely based on the experimental measurement of T_1 . In the first section we show the results of T_1 relaxometry in the presence of Gd,

describing the effect of laser power and Gd concentration on the luminescence shape. As it will be discussed, the luminescence clearly detects two components, one related to the usual T_1 relaxation and the second attributed to charge recombination (recharge), after a photoionization of NV centers during the preparation pulse. It will be shown that a single exponential decay, consistent with spins relaxation, is not enough to describe the evolution of luminescence coming from ensembles of NV centers. Only by considering two coupled dynamics of charge and spin it is possible to reproduce the evolution of the luminescence.

Even if the photodynamics of the two charge states NV^0 and NV^- has been intensively studied, some aspects are not fully understood. Under laser irradiation, the NV^- may lose an electron and be photoionized into NV^0 . The recharge process (back conversion $NV^0 \rightarrow NV^-$) is also induced by laser radiation^{71,204,205}. The photoionization of NV^- occurs either via a two-photon process (under intense irradiation), where one photon excites the system from the ground state to the 3E triplet and the second photon sends the electron into the conduction band, or via a single-photon process (under weaker irradiation), where the excited state cedes an electron to a close defect via tunneling^{68,206}. The single-photon process is likely to depend on the amount of defects, such as vacancies and substitutional nitrogen atoms, capable of trapping and donating electrons²⁰⁷. In particular, substitutional nitrogen is an electron donor and it was speculated that it can affect the charge state of proximate NV, by forming coupled systems⁶⁸ of the type $[NV - N]$.

In a recent work⁷² it was experimentally reported that the recharge mechanism $NV^0 \rightarrow NV^-$ occurs in the dark, without any optical and thermal excitation. This evidence supports the picture of tunneling-mediated charge diffusion. Our NDs have an NV content of 5 ppm. Assuming a tenfold concentration of substitutional nitrogen (common in HPHT diamonds, the starting bulk material of our NDs), we obtain 50 ppm of nitrogen, either in

neutral (N^0) or charged state (N^+). Due to this high nitrogen content⁶⁸ and the experimental evidences take from literature, we implicitly consider the possibility of charge transfer between the NV centers and single or “networks” of nitrogen impurities. The details of this model will be presented in the next section. Despite being a hazardous source of spin depolarization⁷⁰, charge dynamics, together with spin dynamics, gives a striking demonstration of NV sensing the magnetic noise.

In the second and final section we repeat the same kind of measures with rat’s blood. Deoxygenated hemoglobin (deoxyhemoglobin) is paramagnetic and supposed to play a role in T_1 shortening. We will see that spin dynamics alone can describe the experimental observations, with no sign of coupled charge and spin dynamics.

6.1 T_1 relaxometry with gadolinium

Mixtures of NDs and gadolinium were realized in two different ways. In the first set of experiments several solutions of Gd complexes at different concentrations were obtained by dilution of gadoteridol (0.5 M) with deionized water; the solutions were then added to a suspension of NDs and sonicated for several minutes to avoid clustering. A droplet of each mixture was deposited on thin glass slides and let dry. Each sample was then measured in turn. In the second set, a droplet of suspended NDs was deposited on a glass slide and later Gd was added recursively. At each step, the droplet was let evaporate and T_1 relaxation was recorded, before adding another droplet. In this way it was possible to increase gradually the material deposited onto the NDs without changing the sample. The two methods did not display appreciable differences.

The experimental results of the recursive addition of Gd, at constant laser power of 5 mW before focusing, are shown in Figure 6.1. 4 μg of NDs were deposited onto a glass slide, obtaining a spot of diameter ≈ 2 mm and height ≈ 350 nm. The average diameter of the spot was measured with a caliper, while the height was calculated from the mass of the precipitate by considering a molar mass of 12.01 g mol^{-1} for the NDs. Then Gd was deposited, ranging between $10^{-4} \mu\text{mol}$ and $0.12 \mu\text{mol}$. With no Gd, the expected T_1 exponential decay was observed ($T_1 \approx 0.6$ ms, panel a). With increasing amounts of Gd, a new component appeared at longer times, getting more and more prominent. At the same time the spin-lattice decay became steeper until the dynamics was dominated by the growing component. While the first decay curve has been attributed to longitudinal relaxations, the new component has not been reported in the literature so far, to the best of our knowledge. The whole decay profile was empirically fitted by a double exponential, with a global function of the type

$$I(t) = I_{eq} [1 - \alpha(I_P, c_{Gd}) e^{-t/T_r} + \beta(I_P, c_{Gd}) e^{-t/T_1}] \quad (6.1)$$

with I_{eq} the equilibrium intensity (at long times), T_r a *second characteristic time* and the pre-exponential coefficients (amplitudes) α and β depending on the intensity of the preparation pulse I_P and on the Gd concentration c_{Gd} . Even if the fitting function can be improved, for instance by considering two stretched exponentials, we chose to minimize the number of parameters, to avoid artifacts due to the fitting. The double exponential function is able to capture the full dynamics, with only tiny discrepancies around 3 ms (Figure 6.1c,d). A way to improve the fitting will be considered later in the discussion.

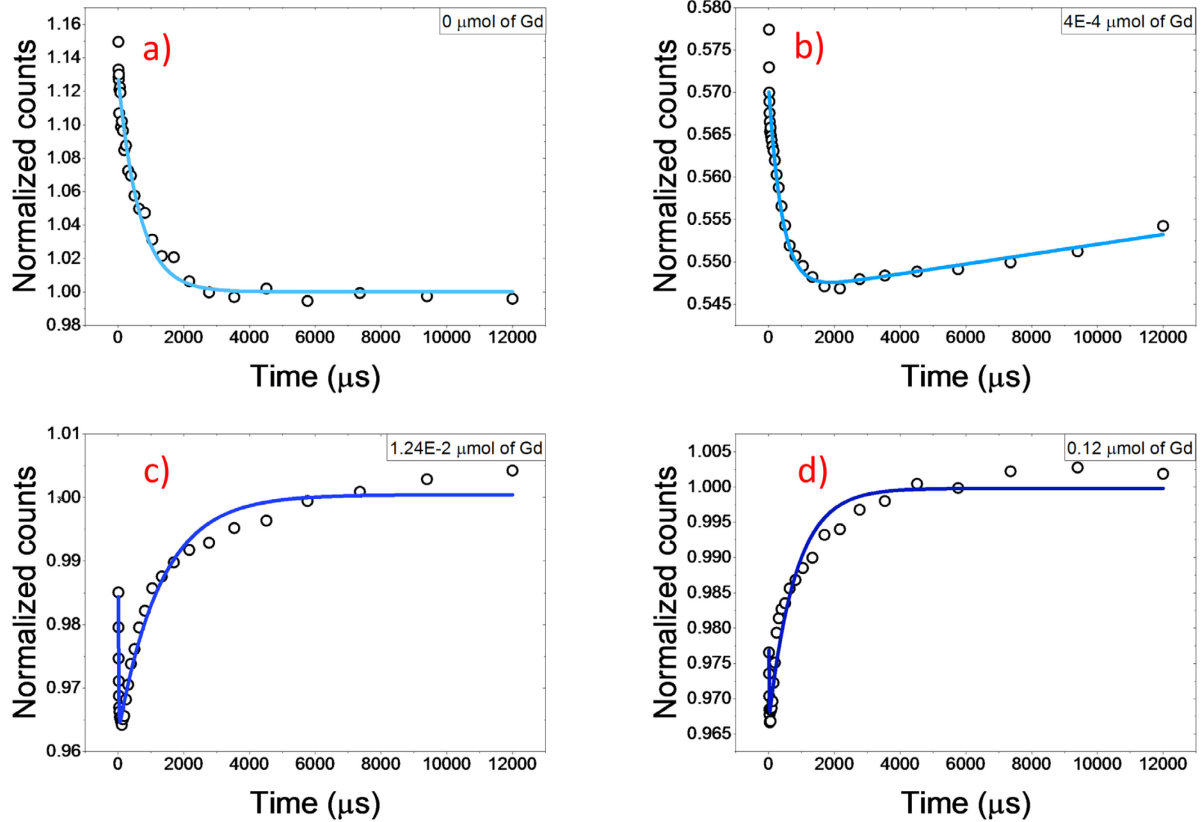


Figure 6.1 – T_1 relaxation curves with increasing amount of Gd deposited on 100 nm bare NDs. With no Gd deposited (a) only a single exponential decay is detected, related to the usual spin-lattice relaxation. With increasing Gd concentration (b, c, d), a longer component related to recharge of the NV^0 becomes more and more visible. As an effect, the probing pulse detects a number of NV^- growing with time and the luminescence increases.

We could describe qualitatively the observed unusual behavior by invoking charge and spin dynamics in a two-step model. First, a fraction of the NV^- is polarized and another is photoionized, during the initialization pulse. The outcome is a non-equilibrium configuration: the $m_s = 0$ level is preferentially

polarized over the $m_s = \pm 1$ levels and the ratio NV^0/NV^- increases. In our picture, photoelectrons get trapped into intraband defects. After the laser switches off, the spins tend to redistribute equally among the ground state triplet and the electrons might recombine in the NV^0 . As anticipated, this second relaxation process, named recharge, has been thought to occur under light excitation until recently, when recharge during the dark time was reported⁷². The dynamics of recharge increases the number of NV^- with time and, consequently, could explain the rise in luminescence. Based on this assumption, we call T_r the recharge time throughout the chapter.

The decay times T_1 , T_r and the coefficients α and β of curves like those in Figure 6.1 are plotted in Figure 6.2. As displayed, α and β do not vary substantially in the broad range spanned by the amount of Gd deposited on NDs. Additionally, it appears that the dynamics of the recharge components of curves related to little Gd (below 1 nmol) extend well beyond the time limit of our present experiments, fixed at 12 ms. For these reason we do not display the fitting parameters in Figure 6.2. On the other side, T_1 decreases considerably with increasing amount of Gd. This reduction of T_1 was explained before in terms of high-frequency noise produced by a paramagnetic environment acting on the NV spins. Explicitly^{67,190},

$$\frac{1}{T_1} = \frac{1}{T_1^{bulk}} + \frac{3\gamma_e^2 \langle B_{\perp}^2 \rangle f_{Gd}}{2\pi f_{Gd}^2 + D^2} \quad (6.2)$$

where γ_e is the electron gyromagnetic ratio, $D = 2.87$ GHz is the ZFS, $\langle B_{\perp}^2 \rangle$ is the variance of the zero-mean transverse magnetic field produced by the fluctuating Gd spins and f_{Gd} is its frequency. Equation 6.2 states that longitudinal relaxation is highly enhanced when the frequency of the magnetic noise matches the ZFS separation. Tetienne et al.¹⁹⁰ reported that the main contribution to f_{Gd} comes from intra-bath dipolar coupling and it scales as $\sqrt{\sigma}$, where σ is the density of Gd paramagnetic spins at the ND

surface. The variance $\langle B_{\perp}^2 \rangle$ was found proportional to σ . Therefore, the second term of Equation 6.2 scales as $\sigma^{3/2}$ at low spin concentration and as $\sigma^{1/2}$ at high spin concentration. Put in other words, in a log-log scale, the slope of T_1 with respect to σ varies between -0.5 and -1.5 . Figure 6.2a indicates a slope of $-2/3$, consistent with this theoretical prediction, once assumed that the spin density at the NDs surface increases with recursive addition of Gd complexes. Apparently it seems that also T_r is affected by the amount of Gd, even though to a lesser extent. The reduction of T_r by an order of magnitude, between 1 nmol and 0.1 μ mol of Gd deposited, has not been understood completely and will be the subject of future investigation. The qualitative difference between curves b and d of Figure 6.1 is not due to a change in the pre-exponential coefficients α and β (which are almost constant), but to a shortening of T_1 , from $\approx 650 \mu$ s without Gd to $\approx 5 \mu$ s with a lot of Gd. This reduction uncovers the longer dynamics of recharge. We want to emphasize that T_1 relaxometry proved to be sensitive to fractions nmoles of Gd (actually 0.1 nmol) deposited on 0.3 μ mol of NDs, as it can be seen by the shortening of T_1 , from 0.65 ms (rectangular tick on the y axis) to 0.25 ms. This sensitivity is unprecedented. Quite recently, Steinert et al.⁶⁷ built a microfluidic device on a diamond containing an array of NV centers. Gadolinium was flowed in the channel and detected by longitudinal relaxations of optically polarized NV spins. By inspecting the Gd-assisted T_1 relaxation, lowest concentrations of 250 μ M of Gd, with oriented NV, and of 80 μ M of Gd, with all four NV axes, were detected. Because of complete evaporation of the solution, we were able to detect 0.1 nmol deposited, which corresponds to an initial concentration of 50 μ M. This high detection efficiency could be facilitated by the elevated density of NV centers and by the large surface/volume ratio typical of nanoparticles, which results in a large area of interaction.

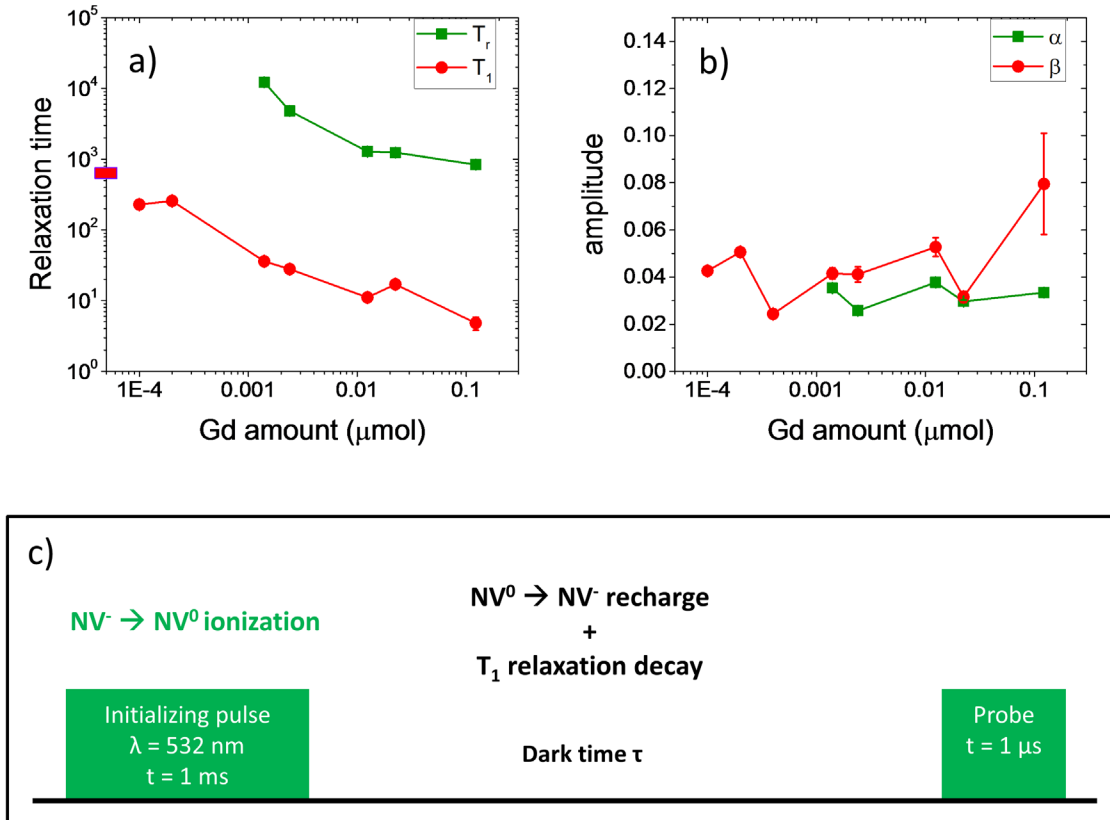


Figure 6.2 – Plot of the spin-lattice relaxation time and recharge time (a) and plot of the pre-exponential coefficients (b) as a function of deposited Gd, as obtained by the biexponential fit of experimental curves. α and β do not show a strong variation in the experimental range, while T_1 and T_r change by two orders of magnitude. Panel c shows the mechanism of recharge and relaxation during the dark time, i.e. between the initializing pulse and the probing pulse.

The Equation 6.1 can be obtained by considering the simple 4-level system of Figure 6.3, where we consider the ground state triplet and a “metastable” state $|M\rangle$ that actually collects a number of levels, depending on the decay mechanism considered. Here $|M\rangle$ contains the excited state, the conduction band and the dark singlet states of the NV^- , populated upon intersystem

crossing. It might also contain other intraband levels, allowing the possibility of charge transfer. Naming γ the transition rate between $|0\rangle$ and $|\pm 1\rangle$, I the laser intensity, σ an indicative cross section of absorption and ionization and k, k' the recombination rates, it is possible to write the rate equations in matrix form

$$\frac{d}{dt} \begin{bmatrix} n_0 \\ n_{-1} \\ n_{+1} \\ n_M \end{bmatrix} = \begin{bmatrix} -2\gamma - I\sigma & \gamma & \gamma & k \\ \gamma & -\gamma - I\sigma & 0 & k' \\ \gamma & 0 & -\gamma - I\sigma & k' \\ I\sigma & I\sigma & I\sigma & -k - 2k' \end{bmatrix} \begin{bmatrix} n_0 \\ n_{-1} \\ n_{+1} \\ n_M \end{bmatrix} \quad (6.3)$$

where n_0, n_{-1}, n_{+1} and n_M are the population of the $|0\rangle, | + 1\rangle, | - 1\rangle$ and $|m\rangle$ states, respectively. The solution for n_0 and $n_{\pm 1}$ is found in terms of a double decaying exponential, with decay times $T_1 = \frac{1}{3\gamma + I\sigma}$, $T_r = \frac{1}{k + 2k' + I\sigma}$ and with coefficients functions of the rate constants and laser intensity, i.e. $\alpha(\gamma, k, k', I\sigma)$ and $\beta(\gamma, k, k', I\sigma)$, such that the two components are coupled. By continuous pumping, the level population reach an equilibrium configuration where n_0 and $n_{\pm 1}$ go to zero, and

$$n_M = \frac{I\sigma}{k + 2k' + I\sigma} \quad (6.4)$$

analogous to Equation 5.8. When the laser is switched off, the times become $T_1 = (3\gamma)^{-1}$ and $T_r = (k + 2k')^{-1}$ and the two components are still coupled through the pre-exponential coefficients. We did not see any appreciable difference in the coupled dynamics when changing the duration of the preparation pulse (finally fixed at 1 ms), so we assume that the preparation pulse is sufficiently long and intense to set stationary populations in the four levels.

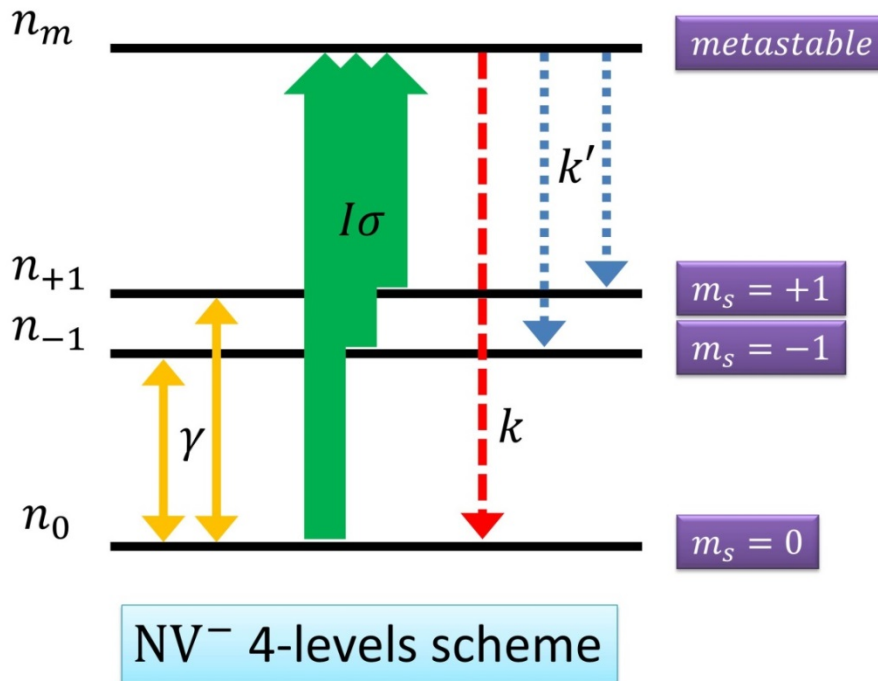


Figure 6.3 – 4-level scheme adopted to extract analytically the biexponential decay. At equilibrium, with laser off, the population is equally distributed in the $|0\rangle$ and $|\pm 1\rangle$ states. When laser is on, the population is pumped into a “metastable” state at a rate $I\sigma$, which represent a collection of states (excited states, conduction band, singlet dark states,...) and relax with different rates (k and k') into the ground state triplet. The population in the ground state triplet is further balanced by direct transitions between the $|0\rangle$ and $|\pm 1\rangle$ states (at a rate γ).

The metastable state $|M\rangle$ contains a group of states. Recombination rates k and k' can stand for radiative and non-radiative transitions and even for charge tunneling. For this reason, the 4-level scheme is highly general and can be adopted to explain, at least qualitatively, a biexponential trend. Let us quickly examine three mechanisms that could lead to such a strong modification of the usual single decay. The singlet states involved in the

intersystem crossing becomes populated under laser irradiation. The population relaxes toward the ground state sublevels, so n_0 and $n_{\pm 1}$ are expected to grow over time. This was actually reported¹⁹⁰. Further, the coupling between the singlet states and the excited and ground states was found to be dependent on high external magnetic field²⁰⁸. Nevertheless, the lifetime of the singlet states is of the order of 200 ns^{190,209}, so this mechanism does not play a role at longer times. Chapman and Plakhotnik⁷⁰ inspected the ionization of the NV^- via a two photon process and elaborated a model based on ten levels. Under optical illumination, the conduction band is populated by photoelectrons, that quickly decay in the excited state, first, and then in the ground state. Again, due to the short lifetime of both conduction band and excited state^{210,211} (less than 50 ns and ≈ 15 ns, respectively), it is unlikely that this mechanism can provide free electrons for recharge few ms after switching off the laser. This picture may be modified if we assume the existence of intraband defects, that can temporarily trap electrons. Manson and Harrison⁶⁸ hypothesized the possibility of forming coupled systems of $[NV]^- - [N]^+$ and $[NV]^0 - [N]^0$, with electrons tunneling between these two charge configurations. Since a lot of NV centers (5 ppm) are associated to many other defects²¹², including substitutional nitrogen, this phenomenon could take place on much longer timescales (around 100 μs)⁷², possible depending also on the relative distance between the NV and the defects²⁰⁷. Therefore, this third mechanism is the most suitable candidate for the interpretation of our experimental data.

Two important remarks to the 4-level model must be added. First, with N levels one can have as much as N decay rates. In our 4-level model, one rate is zero and corresponds to equilibrium, other two build up T_1 and T_r . A fourth decay rate governs a net population transfer between $|+1\rangle$ and $|-1\rangle$, without affecting n_0 and n_M . We considered $n_{+1} = n_{-1}$, so this transition was neglected. In fact, it could play a role only if the $|\pm 1\rangle$ states had a different

initial population, as a consequence, for instance, of the application of a microwave pulse. Second, the dynamics of NV centers varies depending on the position in the ND and on the closeness to external Gd. The collected PL signal comes from several NDs, whose subsurface NV feel a stronger interaction with the external spin bath, compared to the inner NV. A convolution of these decay signals is expected to generate stretched exponentials and is the subject of future investigation.

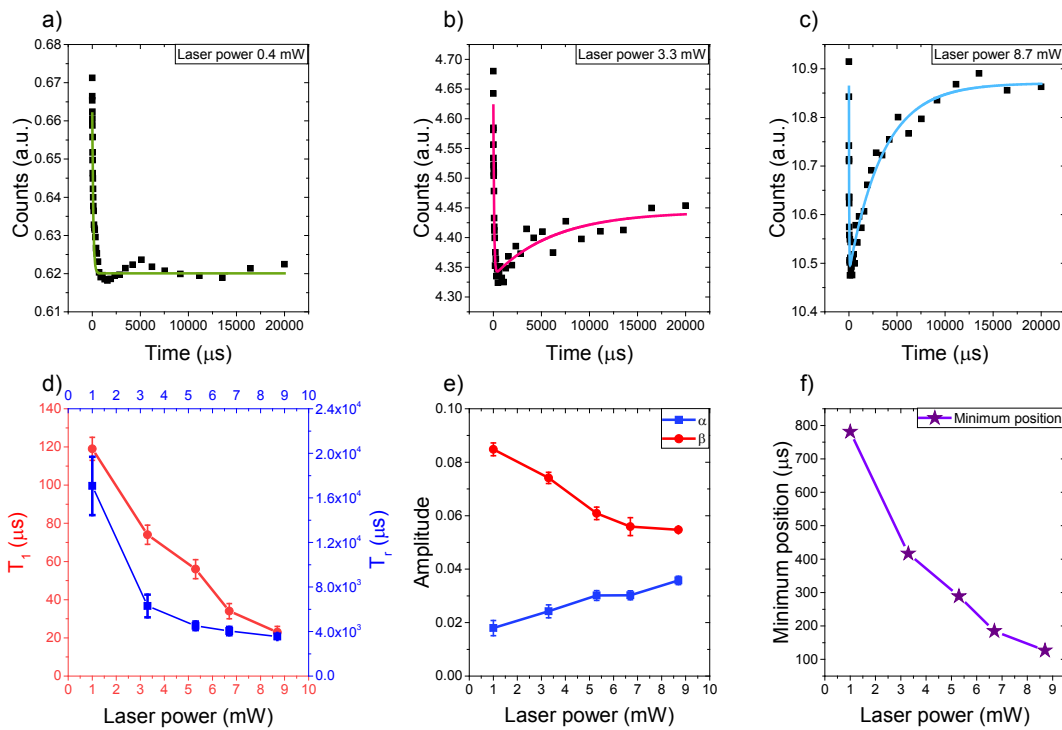


Figure 6.4 – Laser-power dependence of spin and charge relaxations in NDs. The recharge mechanism is facilitated by laser power (a, b, c). The bump in (a) has not been interpreted yet. Panels d and e depict the relaxation times and respective pre-exponential coefficients. The position of the minimum (f) also shifts to early times by increasing the laser power.

The Equation 6.1 was tested in another experiment, where the Gd concentration was kept constant ($5 \cdot 10^{-4} \mu\text{mol}$) and only the laser power was changed (Figure 6.4). It can be seen that the transition rates γ, k, k' depend on the Gd concentration and laser intensity, and in turn T_1, T_r and the coefficients vary also with laser intensity.

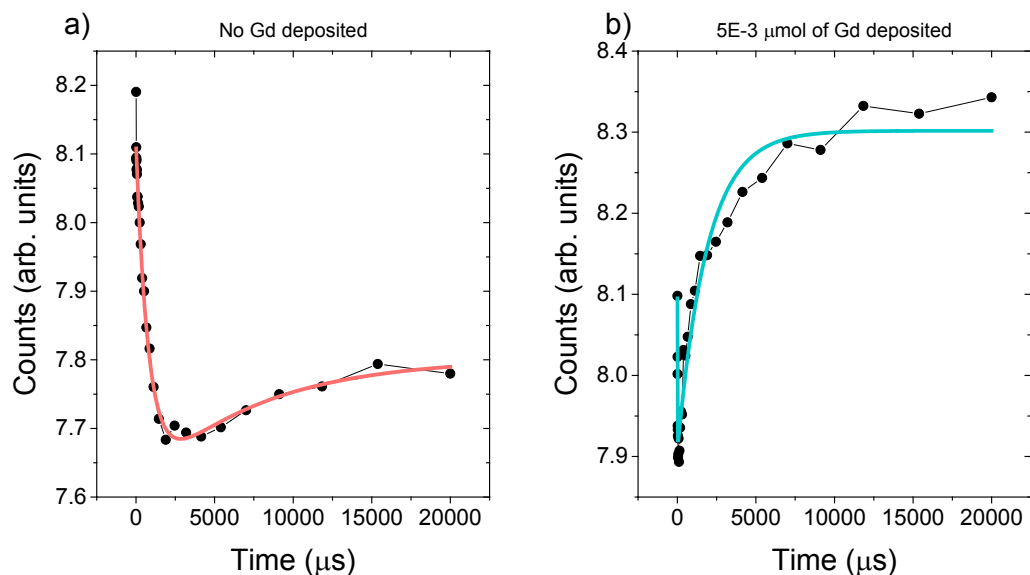


Figure 6.5 – Effect of Gd deposited on 100 nm silica-coated NDs. The silica coating prevents a direct exchange of charges with the external environment, even if the mechanism of recombination is facilitated by the presence of external Gd (panel b) with respect to the case of no Gd deposited (panel a).

In our current picture, it must be noticed that charges are not directly provided from the external environment, since Gd complexes have an overall

neutral charge and the same behavior is obtained with silica-coated NDs, in which the ≈ 10 nm silica layer electrically insulates the NDs (Figure 6.5). The experiments with silica-coated NDs are enlightening for two reasons: first, they show that charge dynamics is uncovered by the presence of Gd, but it is always present if the laser intensity is sufficiently high (compare panels a and b of Figure 6.5 and also Figure 6.4). This again supports the hypothesis of an internal mechanism, with no net exchange of electrons with the surrounding environment. Second, even if the NV spin is coupled with the Gd spin via a dipole-dipole interaction, which scales as the cube of the distance, the NV centers are so sensitive that a 10 nm layer of silica do not exclude the interaction. With $5 \cdot 10^{-3}$ μmol of Gd, T_1 is about 7.5 μs , two orders of magnitude less than the case with no Gd (Figure 6.5a,b). This relatively long range of detection is another valuable trait of NV-enriched NDs.

6.2 T_1 relaxometry with blood

In this final paragraph, the same procedure use to perform T_1 relaxation with Gd solutions was adopted with blood. we mixed 2 μL of 100 nm bare NDs suspension with 2 μL of deoxygenated blood of rat and saline, then deposited the solution on a microscope glass and let it dry. The results of T_1 relaxometry are shown in Figure 6.6. The relaxation curves with and without blood are normalized for a better comparison. Differently from the case of Gd, no signature of the recharge dynamics is detected. However, there is an indication of T_1 shortening, probably due to the paramagnetic nature of deoxyhemoglobin.

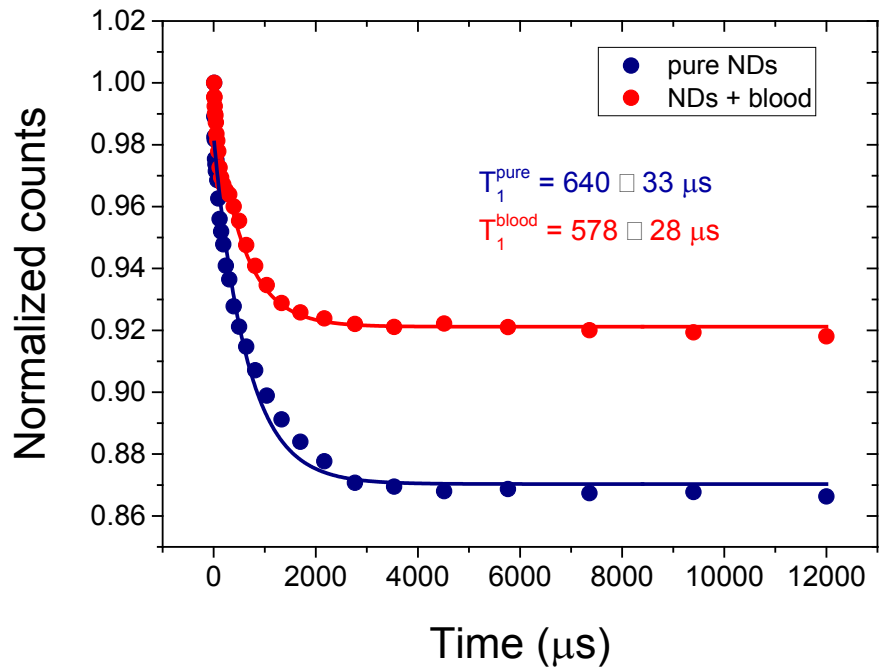


Figure 6.6 – Comparison of the spin-lattice relaxation decays with and without blood added to NDs. The decay is fitted by a single exponential, with no signature of recharge dynamics. There is an indication of T_1 shortening, probably due to the paramagnetic nature of deoxygenated hemoglobin.

Summary

In this thesis I consider both the synthesis and an application in biosensing of NDs. In the first part (Chapters 2, 3 and 4), I demonstrate that PLA of graphite in water is a viable route to produce NDs in aqueous environment, a valuable condition for biological applications. PLA can directly synthesize nanometric diamonds, with potential advantages over alternative methods, like grinding of bulk crystals or detonation techniques. Moreover, I proposed a simple and safe procedure to extract the NDs from the embedding graphite.

Beside synthesis I examine the thermodynamic process leading to nucleation and growth of NDs. Fast laser-induced heating results in the superheating of the target, followed by phase explosion and then by a fast cooling of the molten material. For this reason I provide a theoretical description of the thermodynamics of metastable liquids, both superheated and undercooled, and of the process of phase explosion (Chapters 2 and 3). The investigation of the link between the metastable liquids and the synthesis of nanoparticles is carried out by theoretical analyses, computer simulations and by a robust comparison with our experimental data and with previous literature (Chapter 4).

In the second part of the thesis I explore the use of commercial NV-enriched NDs for sensing of paramagnetic species of biological interest. To this end, I explored the effects of size and surface coating on the optical properties and sensing capabilities of NDs. The relatively high concentration of NV centers in NDs results in high fluorescence levels and fast loss in coherence. The experimental results fit in a theoretical framework, describing

the basic properties and the ground state spin dynamics of these color centers.

The most striking result concerns the dynamics of the spin-lattice relaxation time T_1 . Differently from previous reports, spin dynamics after polarization of NV centers could not be described by a single exponential decay, but showed a complex time evolution that I attribute to charge conversion between the negative and neutral forms of the NV center. Unexpectedly, I found that coupled charge and spin dynamics are strongly affected by paramagnetic interactions, yielding elevated sensitivity to subnanomolar concentrations of gadolinium, a strong paramagnetic contrast agent. The connection between relaxation dynamics and concentration of paramagnetic species can open new perspectives in biosensing and in bioimaging. As a demonstration of a practical application, I tested the sensitivity of NDs in the detection of deoxyhemoglobin, an endogenous paramagnetic species in blood.

Bibliography

- 1 Dan, G., Guoxin, X. & Jianbin, L. Mechanical properties of nanoparticles: basics and applications. *Journal of Physics D: Applied Physics* **47**, 013001 (2014).
- 2 Kelly, K. L., Coronado, E., Zhao, L. L. & Schatz, G. C. The Optical Properties of Metal Nanoparticles: The Influence of Size, Shape, and Dielectric Environment. *The Journal of Physical Chemistry B* **107**, 668-677, (2003).
- 3 Taylor, R. *et al.* Small particles, big impacts: A review of the diverse applications of nanofluids. *Journal of Applied Physics* **113**, 011301, (2013).
- 4 Khan, I., Saeed, K. & Khan, I. Nanoparticles: Properties, applications and toxicities. *Arabian Journal of Chemistry*, (2017).
- 5 Edla, R. *et al.* Highly photo-catalytically active hierarchical 3D porous/urchin nanostructured Co₃O₄ coating synthesized by Pulsed Laser Deposition. *Applied Catalysis B: Environmental* **166-167**, 475-484, (2015).
- 6 Shimamura, K. *et al.* Hydrogen-on-demand using metallic alloy nanoparticles in water. *Nano Lett* **14**, 4090-4096, (2014).
- 7 Liu, Y. *et al.* Study on hydrogen storage properties of Mg nanoparticles confined in carbon aerogels. *International Journal of Hydrogen Energy* **38**, 5302-5308, (2013).
- 8 Hofmann-Amtenbrink, M., Grainger, D. W. & Hofmann, H. Nanoparticles in medicine: Current challenges facing inorganic nanoparticle toxicity assessments and standardizations. *Nanomedicine* **11**, 1689-1694, (2015).
- 9 Singh, R. & Lillard, J. W., Jr. Nanoparticle-based targeted drug delivery. *Exp Mol Pathol* **86**, 215-223, (2009).
- 10 Treuel, L. & Nienhaus, G. U. Toward a molecular understanding of nanoparticle–protein interactions. *Biophysical Reviews* **4**, 137-147, (2012).
- 11 Ramesh, S. Sol-Gel Synthesis and Characterization of Nanoparticles. *Journal of Nanoscience* **2013**, 1-8, (2013).

-
- 12 Li, J., Wu, Q. & Wu, J. Synthesis of Nanoparticles via Solvothermal and Hydrothermal Methods. 295-328, (2016).
 - 13 Phiwdang, K., Suphankij, S., Mekprasart, W. & Pecharapa, W. Synthesis of CuO Nanoparticles by Precipitation Method Using Different Precursors. *Energy Procedia* **34**, 740-745, (2013).
 - 14 Kumar, B. & Thareja, R. K. Synthesis of nanoparticles in laser ablation of aluminum in liquid. *Journal of Applied Physics* **108**, 064906, (2010).
 - 15 Shih, C. Y., Wu, C., Shugaev, M. V. & Zhigilei, L. V. Atomistic modeling of nanoparticle generation in short pulse laser ablation of thin metal films in water. *J Colloid Interface Sci* **489**, 3-17, (2017).
 - 16 Amendola, V. & Meneghetti, M. What controls the composition and the structure of nanomaterials generated by laser ablation in liquid solution? *Phys Chem Chem Phys* **15**, 3027-3046, (2013).
 - 17 Zhigilei, L. V. Dynamics of the plume formation and parameters of the ejected clusters in short-pulse laser ablation. *Applied Physics A: Materials Science & Processing* **76**, 339-350, (2003).
 - 18 Mochalin, V. N., Shenderova, O., Ho, D. & Gogotsi, Y. The properties and applications of nanodiamonds. *Nature nanotechnology* **7**, 11-23, (2011).
 - 19 Bogatyreva, G. P. *et al.* Application of modified nanodiamonds as catalysts of heterogeneous and electrochemical catalyses. *Physics of the Solid State* **46**, 738-741, (2004).
 - 20 Chang, B.-M. *et al.* Highly Fluorescent Nanodiamonds Protein-Functionalized for Cell Labeling and Targeting. *Advanced Functional Materials* **23**, 5737-5745, (2013).
 - 21 Kaur, R. & Badea, I. Nanodiamonds as novel nanomaterials for biomedical applications: drug delivery and imaging systems. *Int J Nanomedicine* **8**, 203-220, (2013).
 - 22 Danilenko, V. V. On the history of the discovery of nanodiamond synthesis. *Physics of the Solid State* **46**, 595-599, (2004).
 - 23 Iakoubovskii, K. *et al.* Structure and defects of detonation synthesis nanodiamond. *Diamond and Related Materials* **9**, 861-865, (2000).
 - 24 Stehlik, S. *et al.* High-yield fabrication and properties of 1.4 nm nanodiamonds with narrow size distribution. *Sci Rep* **6**, 38419, (2016).

-
- 25 Khachatryan, A. K. *et al.* Graphite-to-diamond transformation induced by ultrasound cavitation. *Diamond and Related Materials* **17**, 931-936, (2008).
- 26 Butler, J. E. & Sumant, A. V. The CVD of Nanodiamond Materials. *Chemical Vapor Deposition* **14**, 145-160, (2008).
- 27 Lou, Z., Chen, Q., Zhang, Y., Wang, W. & Qian, Y. Diamond Formation by Reduction of Carbon Dioxide at Low Temperatures. *Journal of the American Chemical Society* **125**, 9302-9303, (2003).
- 28 Baidakova, M. V. *et al.* Structure of nanodiamonds prepared by laser synthesis. *Physics of the Solid State* **55**, 1747-1753, (2013).
- 29 Hu, A., Sanderson, J., Zhou, Y. & Duley, W. W. Formation of diamond-like carbon by fs laser irradiation of organic liquids. *Diamond and Related Materials* **18**, 999-1001, (2009).
- 30 Panich, A. M., Shames, A. I., Zousman, B. & Levinson, O. Magnetic resonance study of nanodiamonds prepared by laser-assisted technique. *Diamond and Related Materials* **23**, 150-153, (2012).
- 31 Doherty, M. W. *et al.* The nitrogen-vacancy colour centre in diamond. *Physics Reports* **528**, 1-45, (2013).
- 32 Maze, J. *et al.* Properties of nitrogen-vacancy centers in diamond: group theoretic approach. (2010).
- 33 Degen, C. L. Scanning magnetic field microscope with a diamond single-spin sensor. *Applied Physics Letters* **92**, 243111, (2008).
- 34 Dolde, F. *et al.* Electric-field sensing using single diamond spins. *Nat Phys* **7**, 459-463, (2011).
- 35 Acosta, V. M. *et al.* Temperature Dependence of the Nitrogen-Vacancy Magnetic Resonance in Diamond. *Physical Review Letters* **104**, 070801 (2010).
- 36 Shenderova, O. A. & McGuire, G. E. Science and engineering of nanodiamond particle surfaces for biological applications (Review). *Biointerphases* **10**, 030802, (2015).
- 37 Balasubramanian, G., Lazarev, A., Arumugam, S. R. & Duan, D. W. Nitrogen-Vacancy color center in diamond-emerging nanoscale applications in bioimaging and biosensing. *Curr Opin Chem Biol* **20**, 69-77, (2014).

-
- 38 Holt, K. B. Diamond at the nanoscale: applications of diamond nanoparticles from cellular biomarkers to quantum computing. *Philos Trans A Math Phys Eng Sci* **365**, 2845-2861, (2007).
- 39 McGuinness, L. P. *et al.* Quantum measurement and orientation tracking of fluorescent nanodiamonds inside living cells. *Nat Nano* **6**, 358-363, (2011).
- 40 Alvarez, G. A. *et al.* Local and bulk ¹³C hyperpolarization in nitrogen-vacancy-centred diamonds at variable fields and orientations. *Nat Commun* **6**, 8456, (2015).
- 41 King, J. P. *et al.* Room-temperature in situ nuclear spin hyperpolarization from optically pumped nitrogen vacancy centres in diamond. *Nat Commun* **6**, 8965, (2015).
- 42 Dhomkar, S., Henshaw, J., Jayakumar, H. & Meriles, C. A. Long-term data storage in diamond. *Science Advances* **2**, (2016).
- 43 Kurtsiefer, C., Mayer, S., Zarda, P. & Weinfurter, H. Stable Solid-State Source of Single Photons. *Physical Review Letters* **85**, 290-293 (2000).
- 44 Childress, L. *et al.* Coherent Dynamics of Coupled Electron and Nuclear Spin Qubits in Diamond. *Science* **314**, 281-285, (2006).
- 45 Balasubramanian, G. *et al.* Ultralong spin coherence time in isotopically engineered diamond. *Nat Mater* **8**, 383-387 (2009).
- 46 Wolf, T. *et al.* Subpicotesla Diamond Magnetometry. *Physical Review X* **5**, (2015).
- 47 Acosta, V. M. *et al.* Diamonds with a high density of nitrogen-vacancy centers for magnetometry applications. *Physical Review B* **80**, (2009).
- 48 Rondin, L. *et al.* Magnetometry with nitrogen-vacancy defects in diamond. *Rep Prog Phys* **77**, 056503, (2014).
- 49 Sundaram, S. K. & Mazur, E. Inducing and probing non-thermal transitions in semiconductors using femtosecond laser pulses. *Nat Mater* **1**, 217-224 (2002).
- 50 Allen, P. B. Theory of thermal relaxation of electrons in metals. *Physical Review Letters* **59**, 1460-1463 (1987).
- 51 Miotello, A. & Kelly, R. Critical assessment of thermal models for laser sputtering at high fluences. *Applied Physics Letters* **67**, 3535-3537, (1995).
- 52 Martynyuk, M. M. Phase explosion of a metastable fluid. *Combustion, Explosion and Shock Waves* **13**, 178-191, (1977).

-
- 53 Kuznetsov, A. I., Koch, J. & Chichkov, B. N. Laser-induced backward transfer of gold nanodroplets. *Opt. Express* **17**, 18820-18825, (2009).
- 54 Mazzi, A., Gorrini, F. & Miotello, A. Liquid nanodroplet formation through phase explosion mechanism in laser-irradiated metal targets. *Physical Review E* **92**, (2015).
- 55 Mazzi, A., Gorrini, F. & Miotello, A. Dynamics of liquid nanodroplet formation in nanosecond laser ablation of metals. *Applied Surface Science* **418**, 601-606, (2017).
- 56 Sengers, J. V. & Sengers, J. M. H. L. Thermodynamic Behavior of Fluids Near the Critical Point. *Annual Review of Physical Chemistry* **37**, 189-222, (1986).
- 57 Bulgakova, N. M. & Bulgakov, A. V. Pulsed laser ablation of solids: transition from normal vaporization to phase explosion. *Applied Physics A Materials Science & Processing* **73**, 199-208, (2001).
- 58 Follstaedt, D. M., Peercy, P. S. & Perepezko, J. H. Phase selection during pulsed laser annealing of manganese. *Applied Physics Letters* **48**, 338-340, (1986).
- 59 Yoon, W., Paik, J. S., LaCourt, D. & Perepezko, J. H. The effect of pressure on phase selection during nucleation in undercooled bismuth. *Journal of Applied Physics* **60**, 3489-3494, (1986).
- 60 Jiang, Q. & Lu, H. M. Size dependent interface energy and its applications. *Surface Science Reports* **63**, 427-464, (2008).
- 61 Hwang, N. M., Hahn, J. H. & Yoon, D. Y. Chemical potential of carbon in the low pressure synthesis of diamond. *Journal of Crystal Growth* **160**, 87-97, (1996).
- 62 Gorrini, F. *et al.* On the thermodynamic path enabling a room-temperature, laser-assisted graphite to nanodiamond transformation. *Sci Rep* **6**, 35244, (2016).
- 63 Dobrovitski, V. V., Feiguin, A. E., Awschalom, D. D. & Hanson, R. Decoherence dynamics of a single spin versus spin ensemble. *Physical Review B* **77**, (2008).
- 64 Dobrovitski, V. V., Feiguin, A. E., Hanson, R. & Awschalom, D. D. Decay of Rabi oscillations by dipolar-coupled dynamical spin environments. *Phys Rev Lett* **102**, 237601, (2009).
- 65 Doherty, M. W. *et al.* Theory of the ground state spin of the NV⁻ center in diamond: I. Fine structure, hyperfine structure, and interactions with electric, magnetic and strain fields. *Phys. Rev. B* **85**, 205203, (2011).

-
- 66 Kaufmann, S. *et al.* Detection of atomic spin labels in a lipid bilayer using a single-spin nanodiamond probe. *Proceedings of the National Academy of Sciences* **110**, 10894-10898, (2013).
- 67 Steinert, S. *et al.* Magnetic spin imaging under ambient conditions with sub-cellular resolution. *Nat Commun* **4**, 1607, (2013).
- 68 Manson, N. B. & Harrison, J. P. Photo-ionization of the nitrogen-vacancy center in diamond. *Diamond and Related Materials* **14**, 1705-1710, (2005).
- 69 Gaebel, T. *et al.* Photochromism in single nitrogen-vacancy defect in diamond. *Applied Physics B* **82**, 243-246, (2005).
- 70 Chapman, R. & Plakhotnik, T. Anomalous saturation effects due to optical spin depolarization in nitrogen-vacancy centers in diamond nanocrystals. *Physical Review B* **86**, (2012).
- 71 Aslam, N., Waldherr, G., Neumann, P., Jelezko, F. & Wrachtrup, J. Photo-induced ionization dynamics of the nitrogen vacancy defect in diamond investigated by single-shot charge state detection. *New Journal of Physics* **15**, 013064, (2013).
- 72 Choi, J. *et al.* Depolarization Dynamics in a Strongly Interacting Solid-State Spin Ensemble. *Phys Rev Lett* **118**, 093601, (2017).
- 73 Wang, J. B., Zhang, C. Y., Zhong, X. L. & Yang, G. W. Cubic and hexagonal structures of diamond nanocrystals formed upon pulsed laser induced liquid–solid interfacial reaction. *Chemical Physics Letters* **361**, 86-90, (2002).
- 74 Wang, C. X. & Yang, G. W. Thermodynamics of metastable phase nucleation at the nanoscale. *Materials Science and Engineering: R: Reports* **49**, 157-202, (2005).
- 75 Zhigilei, L. V., Lin, Z. & Ivanov, D. S. Atomistic Modeling of Short Pulse Laser Ablation of Metals: Connections between Melting, Spallation, and Phase Explosion. *The Journal of Physical Chemistry C* **113**, 11892-11906, (2009).
- 76 Kelly, R. & Miotello, A. Contribution of vaporization and boiling to thermal-spike sputtering by ions or laser pulses. *Physical Review E* **60**, 2616-2625 (1999).
- 77 Skripov, V. P. *Metastable liquids*. (J. Wiley, 1973).
- 78 Debenedetti, P. G. in *Physical chemistry (Princeton, N.J.)*, (Princeton University Press, 1996).

-
- 79 Speedy, R. J. Limiting forms of the thermodynamic divergences at the conjectured stability limits in superheated and supercooled water. *The Journal of Physical Chemistry* **86**, 3002-3005, (1982).
- 80 Blairs, S. & Abbasi, M. H. Correlation between surface tension and critical temperatures of liquid metals. *Journal of Colloid and Interface Science* **304**, 549-553, (2006).
- 81 D.R., L. *Handbook of Chemistry and Physics*. 90ed. edn, (CRC, 2010).
- 82 Keene, B. J. Review of data for the surface tension of pure metals. *International Materials Reviews* **38**, 157-192, (1993).
- 83 Lu, H. M. & Jiang, Q. Surface Tension and Its Temperature Coefficient for Liquid Metals. *The Journal of Physical Chemistry B* **109**, 15463-15468, (2005).
- 84 Leider, H. R., Krikorian, O. H. & Young, D. A. Thermodynamic properties of carbon up to the critical point. *Carbon* **11**, 555-563, (1973).
- 85 Guggenheim, E. A. The Principle of Corresponding States. *The Journal of Chemical Physics* **13**, 253-261, (1945).
- 86 Watson, K. M. Thermodynamics of the Liquid State. *Industrial & Engineering Chemistry* **35**, 398-406, (1943).
- 87 Wang, J. & Anisimov, M. A. Nature of vapor-liquid asymmetry in fluid criticality. *Physical Review E* **75**, 051107 (2007).
- 88 Jüngst, S., Knuth, B. & Hensel, F. Observation of Singular Diameters in the Coexistence Curves of Metals. *Physical Review Letters* **55**, 2160-2163 (1985).
- 89 Apfelbaum, E. M. & Vorob'ev, V. S. The Wide-Range Method to Construct the Entire Coexistence Liquid-Gas Curve and to Determine the Critical Parameters of Metals. *The Journal of Physical Chemistry B* **119**, 11825-11832, (2015).
- 90 Anisimov, S. Vaporization of metal absorbing laser radiation. *Sov. Phys. JETP* **27**, 182-183 (1968).
- 91 Knight, C. J. Theoretical Modeling of Rapid Surface Vaporization with Back Pressure. *AIAA Journal* **17**, 519-523, (2012).
- 92 Musella, M., Ronchi, C., Brykin, M. & Sheindlin, M. The molten state of graphite: An experimental study. *Journal of Applied Physics* **84**, 2530-2537, (1998).
- 93 Kruusing, A. *Handbook of Liquids-Assisted Laser Processing*. 1st edition edn, (Elsevier Science, 2007).

-
- 94 Birdi, K. S. *Surface and Colloid Chemistry: Principles and Applications*. (2009).
- 95 Dergarabedian, P. *The rate of growth of vapor bubbles in superheated water*, California Institute of Technology, (1952).
- 96 Forster, H. & Zuber, N. Dynamics of vapor bubbles and boiling heat transfer. *AIChE Journal* **1**, 531-535 (1955).
- 97 Prosperetti, A. & Plesset, M. S. Vapour-bubble growth in a superheated liquid. *Journal of Fluid Mechanics* **85**, 349-368 (1978).
- 98 Lee, H. & Merte, H. Spherical vapor bubble growth in uniformly superheated liquids. *International Journal of Heat and Mass Transfer* **39**, 2427-2447, (1996).
- 99 Wu, C. & Zhigilei, L. V. Microscopic mechanisms of laser spallation and ablation of metal targets from large-scale molecular dynamics simulations. *Applied Physics A* **114**, 11-32 (2014).
- 100 Murray, P. & Shin, E. Formation of silver nanoparticles by through thin film ablation. *Materials Letters* **62**, 4336-4338 (2008).
- 101 Alonso, J. *et al.* Thin films of silver nanoparticles deposited in vacuum by pulsed laser ablation using a YAG: Nd laser. *Applied Surface Science* **255**, 4933-4937 (2009).
- 102 Ya. Vul, A. & Shenderova, O. A. Detonation nanodiamonds : science and applications. (2013).
- 103 Amans, D. *et al.* Nanodiamond synthesis by pulsed laser ablation in liquids. *Diamond and Related Materials* **18**, 177-180, (2009).
- 104 Yang, G. W. & Wang, J. B. Pulsed-laser-induced transformation path of graphite to diamond via an intermediate rhombohedral graphite. *Applied Physics A Materials Science & Processing* **72**, 475-479, (2001).
- 105 Mortazavi, S., Parvin, P., Reyhani, A., Mirershadi, S. & Sadighi-Bonabi, R. Generation of various carbon nanostructures in water using IR/UV laser ablation. *Journal of Physics D: Applied Physics* **46**, 165303, (2013).
- 106 Narayan, J. & Bhaumik, A. Research Update: Direct conversion of amorphous carbon into diamond at ambient pressures and temperatures in air. *APL Materials* **3**, 100702, (2015).
- 107 Stauss, S., Urabe, K., Muneoka, H. & Terashima, K. in *Applications of Laser Ablation-Thin Film Deposition, Nanomaterial Synthesis and Surface Modification* (InTech, 2016).

-
- 108 Wang, C. X., Liu, P., Cui, H. & Yang, G. W. Nucleation and growth kinetics of nanocrystals formed upon pulsed-laser ablation in liquid. *Applied Physics Letters* **87**, 201913, (2005).
- 109 Jackson, K. A. Nucleation from the Melt. *Industrial & Engineering Chemistry* **57**, 28-32 (1965).
- 110 Turnbull, D. Under what conditions can a glass be formed? *Contemporary physics* **10**, 473-488 (1969).
- 111 Perepezko, J. H., Follstaedt, D. M. & Peercy, P. S. in *Materials Research Society Symposia Proceedings*. 297-302.
- 112 Hwang, N. M. & Yoon, D. Y. Thermodynamic approach to the paradox of diamond formation with simultaneous graphite etching in the low pressure synthesis of diamond. *Journal of Crystal Growth* **160**, 98-103, (1996).
- 113 Jiang, Q., Li, J. & Wilde, G. The size dependence of the diamond-graphite transition. *Journal of Physics: Condensed Matter* **12**, 5623 (2000).
- 114 Barnard, A. S., Russo, S. P. & Snook, I. K. Coexistence of bucky diamond with nanodiamond and fullerene carbon phases. *Physical Review B* **68**, (2003).
- 115 van Thiel, M. & Ree, F. H. Theoretical description of the graphite, diamond, and liquid phases of carbon. *International Journal of Thermophysics* **10**, 227-236, (1989).
- 116 van Thiel, M. & Ree, F. H. High-pressure liquid-liquid phase change in carbon. *Physical Review B* **48**, 3591-3599, (1993).
- 117 Bundy, F. P. The P, T phase and reaction diagram for elemental carbon, 1979. *Journal of Geophysical Research: Solid Earth (1978–2012)* **85**, 6930-6936, (1980).
- 118 Bundy, F. P. *et al.* The pressure-temperature phase and transformation diagram for carbon; updated through 1994. *Carbon* **34**, 141-153, (1996).
- 119 Yang, C. C. & Li, S. Size-Dependent Temperature–Pressure Phase Diagram of Carbon. *The Journal of Physical Chemistry C* **112**, 1423-1426, (2008).
- 120 Jiang, Q. & Chen, Z. P. Thermodynamic phase stabilities of nanocarbon. *Carbon* **44**, 79-83, (2006).
- 121 Zhao, D. S., Zhao, M. & Jiang, Q. Size and temperature dependence of nanodiamond–nanographite transition related with surface stress. *Diamond and Related Materials* **11**, 234-236, (2002).

-
- 122 Magomedov, M. N. On the surface properties of a nanodiamond. *Physics of the Solid State* **52**, 1283-1292, (2010).
- 123 Barnard, A. S. & Zapol, P. A model for the phase stability of arbitrary nanoparticles as a function of size and shape. *The Journal of Chemical Physics* **121**, 4276-4283, (2004).
- 124 Basharin, Y. A., Dozhdikov, V. S., Kirillin, A. V., Turchaninov, M. A. & Fokin, L. R. Phase diagram with a region of liquid carbon-diamond metastable states. *Technical Physics Letters* **36**, 559-562, (2010).
- 125 Turnbull, D. & Fisher, J. C. Rate of Nucleation in Condensed Systems. *The Journal of Chemical Physics* **17**, 71-73, (1949).
- 126 Yang, G.-W., Wang, J.-B. & Liu, Q.-X. Preparation of nano-crystalline diamonds using pulsed laser induced reactive quenching. *Journal of Physics: Condensed Matter* **10**, 7923 (1998).
- 127 Zazula, J. M. On graphite transformations at high temperature and pressure induced by absorption of the LHC beam. *CERN-LHC-Project-Note-78* **4** (1997).
- 128 Ghiringhelli, L. M., Los, J. H., Meijer, E., Fasolino, A. & Frenkel, D. Liquid carbon: structure near the freezing line. *Journal of Physics: Condensed Matter* **17**, (2005).
- 129 Mazhukin, V. I., Lobok, M. G. & Smurov, I. Transient effects in pulsed laser irradiation. *Applied Surface Science* **253**, 7744-7748, (2007).
- 130 Abd El-Ghany, S. E. S. The temperature profile in the molten layer of a thin-film coated on a substrate induced by irradiation with a pulsed laser. *Optics & Laser Technology* **36**, 95-106, (2004).
- 131 Duff, W. H. & Zhigilei, L. V. in *Journal of Physics: Conference Series*. 413 (IOP Publishing).
- 132 Nian, Q. *et al.* Direct laser writing of nanodiamond films from graphite under ambient conditions. *Scientific reports* **4**, 6612, (2014).
- 133 Fabbro, R., Fournier, J., Ballard, P., Devaux, D. & Virmont, J. Physical study of laser-produced plasma in confined geometry. *Journal of Applied Physics* **68**, 775, (1990).
- 134 Devaux, D., Fabbro, R. & Virmont, J. Generation of Shock Waves by Laser-Matter Interaction in Confined Geometries. *Le Journal de Physique IV* **01**, C7-179-C177-182, (1991).

-
- 135 Berthe, L., Fabbro, R., Peyre, P., Tollier, L. & Bartnicki, E. Shock waves from a water-confined laser-generated plasma. *Journal of Applied Physics* **82**, 2826, (1997).
- 136 Peyre, P., Fabbro, R., Berthe, L., Scherpereel, X. & Bartnicki, E. Laser-shock processing of materials and related measurements. *Proc. SPIE* **3343**, 183-193, (1998).
- 137 Zhu, S., Lu, Y. F. & Hong, M. H. Laser ablation of solid substrates in a water-confined environment. *Applied Physics Letters* **79**, 1396, (2001).
- 138 Yan, Z. & Chrisey, D. B. Pulsed laser ablation in liquid for micro-/nanostructure generation. *Journal of Photochemistry and Photobiology C: Photochemistry Reviews* **13**, 204-223, (2012).
- 139 Ferrari, A. C. Raman spectroscopy of graphene and graphite: Disorder, electron-phonon coupling, doping and nonadiabatic effects. *Solid State Communications* **143**, 47-57, (2007).
- 140 Liu, E., Li, L., Blanpain, B. & Celis, J. P. Residual stresses of diamond and diamondlike carbon films. *Journal of Applied Physics* **98**, 073515, (2005).
- 141 Sharma, S. K., Mao, H. K., Bell, P. M. & Xu, J. A. Measurement of stress in diamond anvils with micro-Raman spectroscopy. *Journal of Raman Spectroscopy* **16**, 350-352, (1985).
- 142 Obraztsova, E. D. *et al.* Raman identification of onion-like carbon. *Carbon* **36**, 821-826, (1998).
- 143 Nakagawa, I. Optically Active Crystal Vibrations of the Alkali-Metal Nitrates. *The Journal of Chemical Physics* **51**, 1389, (1969).
- 144 Chang, Y.-R. *et al.* Mass production and dynamic imaging of fluorescent nanodiamonds. *Nature nanotechnology* **3**, 284-288, (2008).
- 145 Yang, L., May, P. W., Yin, L., Smith, J. A. & Rosser, K. N. Growth of diamond nanocrystals by pulsed laser ablation of graphite in liquid. *Diamond and Related Materials* **16**, 725-729, (2007).
- 146 Berthe, L., Fabbro, R., Peyre, P. & Bartnicki, E. Wavelength dependent of laser shock-wave generation in the water-confinement regime. *Journal of Applied Physics* **85**, 7552, (1999).
- 147 Sakka, T., Saito, K. & Ogata, Y. H. Emission spectra of the species ablated from a solid target submerged in liquid: vibrational temperature of C₂ molecules in water-confined geometry. *Applied Surface Science* **197-198**, 246-250, (2002).

-
- 148 Ren, X. D. *et al.* A conversion model of graphite to ultrananocrystalline diamond via laser processing at ambient temperature and normal pressure. *Applied Physics Letters* **105**, 21908, (2014).
- 149 Yang, G. Laser ablation in liquids: Applications in the synthesis of nanocrystals. *Progress in Materials Science* **52**, 648-698, (2007).
- 150 Gogulya, M. F. Shock structure and parameters under dynamic loading of natural graphite in the polymorphic transformation domain. *Combustion, Explosion, and Shock Waves* **25**, 87-95, (1989).
- 151 Venkatesan, T. *et al.* Measurement of Thermodynamic Parameters of Graphite by Pulsed-Laser Melting and Ion Channeling. *Physical Review Letters* **53**, 360-363 (1984).
- 152 Pastras, G., Fysikopoulos, A., Stavropoulos, P. & Chryssolouris, G. An approach to modelling evaporation pulsed laser drilling and its energy efficiency. *The International Journal of Advanced Manufacturing Technology* **72**, 1227-1241, (2014).
- 153 Chung, S.-Y., Kim, Y.-M., Kim, J.-G. & Kim, Y.-J. Multiphase transformation and Ostwald's rule of stages during crystallization of a metal phosphate. *Nat Phys* **5**, 68-73, (2009).
- 154 Ghiringhelli, L., Los, J., Meijer, E., Fasolino, A. & Frenkel, D. Modeling the Phase Diagram of Carbon. *Physical Review Letters* **94**, (2005).
- 155 Wang, C. X., Yang, Y. H., Xu, N. S. & Yang, G. W. Thermodynamics of Diamond Nucleation on the Nanoscale. *Journal of the American Chemical Society* **126**, 11303-11306, (2004).
- 156 Wang, C. X., Yang, Y. H. & Yang, G. W. Thermodynamical predictions of nanodiamonds synthesized by pulsed-laser ablation in liquid. *Journal of Applied Physics* **97**, 66104, (2005).
- 157 Togaya, M. Pressure Dependences of the Melting Temperature of Graphite and the Electrical Resistivity of Liquid Carbon. *Physical Review Letters* **79**, 2474-2477, (1997).
- 158 Fateeva, N. S. & Vereshchagin, L. F. Concerning the melting point of graphite up to 90 kbar. *JETP Lett* **13**, 110-111 (1971).
- 159 Glosli, J. N. & Ree, F. H. Liquid-Liquid Phase Transformation in Carbon. *Physical Review Letters* **82**, 4659-4662 (1999).

-
- 160 Sun, J., Hu, S.-L., Du, X.-W., Lei, Y.-W. & Jiang, L. Ultrafine diamond synthesized by long-pulse-width laser. *Applied Physics Letters* **89**, 183115, (2006).
- 161 Hu, S., Sun, J., Du, X., Tian, F. & Jiang, L. The formation of multiply twinning structure and photoluminescence of well-dispersed nanodiamonds produced by pulsed-laser irradiation. *Diamond and Related Materials* **17**, 142-146, (2008).
- 162 Bai, P., Hu, S., Zhang, T., Sun, J. & Cao, S. Effect of laser pulse parameters on the size and fluorescence of nanodiamonds formed upon pulsed-laser irradiation. *Materials Research Bulletin* **45**, 826-829, (2010).
- 163 Ren, X. D. *et al.* Graphite to ultrafine nanocrystalline diamond phase transition model and growth restriction mechanism induced by nanosecond laser processing. *Applied Physics Letters* **107**, 141907, (2015).
- 164 Wei, Q. & Narayan, J. Superhard diamondlike carbon: preparation, theory, and properties. *International materials reviews* **45**, 133-164 (2000).
- 165 Guo-Wei, Y., Jin-Bin, W. & Qui-Xiang, L. Preparation of nano-crystalline diamonds using pulsed laser induced reactive quenching. *Journal of Physics: Condensed Matter* **10**, 7923 (1998).
- 166 Santori, C., Barclay, P. E., Fu, K.-M. C. & Beausoleil, R. G. Vertical distribution of nitrogen-vacancy centers in diamond formed by ion implantation and annealing. *Physical Review B* **79**, (2009).
- 167 Kaiser, W. & Bond, W. Nitrogen, a major impurity in common type I diamond. *Physical Review* **115**, 857 (1959).
- 168 Tian, Y. *et al.* Dependence of nitrogen concentration in type Ib diamonds on synthesis temperature. *Science Bulletin* **54**, 1459-1462, (2009).
- 169 Pezzagna, S., Rogalla, D., Wildanger, D., Meijer, J. & Zaitsev, A. Creation and nature of optical centres in diamond for single-photon emission—overview and critical remarks. *New Journal of Physics* **13**, 035024 (2011).
- 170 Song, X. *et al.* Generation of nitrogen-vacancy color center in nanodiamonds by high temperature annealing. *Applied Physics Letters* **102**, 133109, (2013).
- 171 Martin, J., Wannemacher, R., Teichert, J., Bischoff, L. & Köhler, B. Generation and detection of fluorescent color centers in diamond with submicron resolution. *Applied physics letters* **75**, 3096-3098 (1999).
- 172 Tinkham, M. *Group Theory and Quantum Mechanics*. (Dover Publications, 2003).

-
- 173 Baldassare Di Bartolo, R. C. P. *Crystal Symmetry, Lattice Vibrations and Optical Spectroscopy of Solids: A Group Theoretical Approach*. (World Scientific Publishing Company, 2014).
- 174 Gali, A., Simon, T. & Lowther, J. E. Anab initiostudy of local vibration modes of the nitrogen-vacancy center in diamond. *New Journal of Physics* **13**, 025016, (2011).
- 175 Zhang, J., Wang, C.-Z., Zhu, Z. Z. & Dobrovitski, V. V. Vibrational modes and lattice distortion of a nitrogen-vacancy center in diamond from first-principles calculations. *Physical Review B* **84**, (2011).
- 176 Kehayias, P. *et al.* The Infrared Absorption Band and Vibronic Structure of the Nitrogen-Vacancy Center in Diamond. *arXiv*, (2013).
- 177 Alkauskas, A., Buckley, B. B., Awschalom, D. D. & Van de Walle, C. G. First-principles theory of the luminescence lineshape for the triplet transition in diamond NV centres. *New Journal of Physics* **16**, 073026 (2014).
- 178 Davies, G. & Hamer, M. F. Optical Studies of the 1.945 eV Vibronic Band in Diamond. *Proceedings of the Royal Society A: Mathematical, Physical and Engineering Sciences* **348**, 285-298, (1976).
- 179 Kilin, S. Y., Nizovtsev, A. P., Maevskaya, T. M., Dräbenstedt, A. & Wrachtrup, J. Spectroscopy on single N–V defect centers in diamond: tunneling of nitrogen atoms into vacancies and fluorescence spectra. *Journal of Luminescence* **86**, 201-206, (2000).
- 180 Tizei, L. H. & Kociak, M. Spectrally and spatially resolved cathodoluminescence of nanodiamonds: local variations of the NV(0) emission properties. *Nanotechnology* **23**, 175702, (2012).
- 181 Fu, K. M. C., Santori, C., Barclay, P. E. & Beausoleil, R. G. Conversion of neutral nitrogen-vacancy centers to negatively charged nitrogen-vacancy centers through selective oxidation. *Applied Physics Letters* **96**, 121907,
- 182 Gatto Monticone, D. *et al.* Systematic study of defect-related quenching of NV luminescence in diamond with time-correlated single-photon counting spectroscopy. *Physical Review B* **88**, (2013).
- 183 Yamano, H. *et al.* Charge state stabilization of shallow nitrogen vacancy centers in diamond by oxygen surface modification. *Japanese Journal of Applied Physics* **56**, 04CK08, (2017).
- 184 Chen, X. D. *et al.* Temperature dependent energy level shifts of nitrogen-vacancy centers in diamond. *Applied Physics Letters* **99**, 161903, (2011).

-
- 185 Lenef, A. & Rand, S. Electronic structure of the N-V center in diamond: Theory. *Physical Review B* **53**, 13441 (1996).
- 186 Felton, S. *et al.* Hyperfine interaction in the ground state of the negatively charged nitrogen vacancy center in diamond. *Physical Review B* **79**, (2009).
- 187 Gali, A., Fyta, M. & Kaxiras, E. Ab initio supercell calculations on nitrogen-vacancy center in diamond: Electronic structure and hyperfine tensors. *Physical Review B* **77**, (2008).
- 188 Loubser, J. & van Wyk, J. Electron spin resonance in the study of diamond. *Reports on Progress in Physics* **41**, 1201 (1978).
- 189 Jensen, K., Acosta, V. M., Jarmola, A. & Budker, D. Light narrowing of magnetic resonances in ensembles of nitrogen-vacancy centers in diamond. *Physical Review B* **87**, 014115 (2013).
- 190 Tetienne, J. P. *et al.* Spin relaxometry of single nitrogen-vacancy defects in diamond nanocrystals for magnetic noise sensing. *Physical Review B* **87**, 235436 (2013).
- 191 Bradac, C. *et al.* Observation and control of blinking nitrogen-vacancy centres in discrete nanodiamonds. *Nature Nanotechnology* **5**, 345-349, (2010).
- 192 Levchenko, A. *et al.* Inhomogeneous broadening of optically detected magnetic resonance of the ensembles of nitrogen-vacancy centers in diamond by interstitial carbon atoms. *Applied Physics Letters* **106**, 102402 (2015).
- 193 Jeong, K. *et al.* Understanding the Magnetic Resonance Spectrum of Nitrogen Vacancy Centers in an Ensemble of Randomly Oriented Nanodiamonds. *The Journal of Physical Chemistry C* **121**, 21057-21061, (2017).
- 194 Tetienne, J. P. *et al.* Magnetic-field-dependent photodynamics of single NV defects in diamond: an application to qualitative all-optical magnetic imaging. *New Journal of Physics* **14**, 103033, (2012).
- 195 Hanson, R., Dobrovitski, V. V., Feiguin, A. E., Gywat, O. & Awschalom, D. D. Coherent Dynamics of a Single Spin Interacting with an Adjustable Spin Bath. *Science* **320**, 352-355, (2008).
- 196 Ishikawa, T. *et al.* Optical and spin coherence properties of nitrogen-vacancy centers placed in a 100 nm thick isotopically purified diamond layer. *Nano letters* **12**, 2083-2087 (2012).

-
- 197 Bar-Gill, N., Pham, L. M., Jarmola, A., Budker, D. & Walsworth, R. L. Solid-state electronic spin coherence time approaching one second. *Nature Communications* **4**, 1743, (2013).
- 198 Bayat, K., Choy, J., Baroughi, M., Meesala, S. & Loncar, M. Efficient, Uniform, and Large Area Microwave Magnetic Coupling to NV Centers in Diamond Using Double Split-Ring Resonators. *Nano Letters* **14**, 1208-1213, (2014).
- 199 Mrózek, M. *et al.* Longitudinal spin relaxation in nitrogen-vacancy ensembles in diamond. *EPJ Quantum Technology* **2**, (2015).
- 200 Jarmola, A. *et al.* Longitudinal spin-relaxation in nitrogen-vacancy centers in electron irradiated diamond. *Applied Physics Letters* **107**, 242403, (2015).
- 201 Jarmola, A., Acosta, V. M., Jensen, K., Chemerisov, S. & Budker, D. Temperature- and magnetic-field-dependent longitudinal spin relaxation in nitrogen-vacancy ensembles in diamond. *Phys Rev Lett* **108**, 197601, (2012).
- 202 Pelliccione, M., Myers, B. A., Pascal, L. M. A., Das, A. & Bleszynski Jayich, A. C. Two-Dimensional Nanoscale Imaging of Gadolinium Spins via Scanning Probe Relaxometry with a Single Spin in Diamond. *Physical Review Applied* **2**, (2014).
- 203 Rendler, T. *et al.* Optical imaging of localized chemical events using programmable diamond quantum nanosensors. *Nat Commun* **8**, 14701, (2017).
- 204 Chen, X.-D. *et al.* Spin depolarization effect induced by charge state conversion of nitrogen vacancy center in diamond. *Physical Review B* **92**, (2015).
- 205 Chen, X.-D., Zou, C.-L., Sun, F.-W. & Guo, G.-C. Optical manipulation of the charge state of nitrogen-vacancy center in diamond. *Applied Physics Letters* **103**, 013112 (2013).
- 206 Loretz, M., Takahashi, H., Segawa, T. F., Boss, J. M. & Degen, C. L. Optical hyperpolarization of nitrogen donor spins in bulk diamond. *Physical Review B* **95**, (2017).
- 207 Jayakumar, H. *et al.* Optical patterning of trapped charge in nitrogen-doped diamond. *Nat Commun* **7**, 12660, (2016).
- 208 Capelli, M. *et al.* Magnetic field-induced enhancement of the nitrogen-vacancy fluorescence quantum yield. *arXiv preprint arXiv:1705.07595* (2017).
- 209 Acosta, V. M., Jarmola, A., Bauch, E. & Budker, D. Optical properties of the nitrogen-vacancy singlet levels in diamond. *Physical Review B* **82**, (2010).

- 210 Collins, A. T., Thomaz, M. F. & Jorge, M. I. B. Luminescence decay time of the 1.945 eV centre in type Ib diamond. *Journal of Physics C: Solid State Physics* **16**, 2177 (1983).
- 211 Storteboom, J., Dolan, P., Castelletto, S., Li, X. & Gu, M. Lifetime investigation of single nitrogen vacancy centres in nanodiamonds. *Opt Express* **23**, 11327-11333, (2015).
- 212 Deák, P., Aradi, B., Kaviani, M., Frauenheim, T. & Gali, A. Formation of NV centers in diamond: A theoretical study based on calculated transitions and migration of nitrogen and vacancy related defects. *Physical Review B* **89**, (2014).

